Link-Adaptive Antenna Systems

Michael Roe

Electrical Engineering and Computer Sciences
University of California at Berkeley

May 1, 2019

Link-Adaptive Antenna Systems

by

Michael Roe

A dissertation submitted in partial satisfaction of the

requirements for the degree of

Doctor of Philosophy

in

Engineering - Electrical Engineering and Computer Sciences

in the

Graduate Division

of the

University of California, Berkeley

Committee in charge:

Professor Eli Yablonovitch, Chair
Professor Kannan Ramchandran
Associate Professor Feng Wang

Spring 2017

Link-Adaptive Antenna Systems

Abstract

Link-Adaptive Antenna Systems

by

Michael Roe

Doctor of Philosophy in Engineering - Electrical Engineering and Computer Sciences

University of California, Berkeley

Professor Eli Yablonovitch, Chair

With the proliferation of rich data and multimedia services in cellular and wireless local area networks (WLANs), mobile operators and service providers are looking for solutions to make more efficient use of their spectrum to keep up with consumer demand. A key challenge in wireless systems research is to identify air interface techniques that increase spectral efficiency and reduce outage probability of a communications network. Currently, cellular operators are deploying small cells to improve the spectral efficiency per unit area, but this approach requires large capital investments for installation and precise network planning to manage inter-cell interference. Wireless standards makers and baseband device vendors have proposed higher order QAM modulation schemes. However, the capacity improvements scale logarithmically with the number of IQ constellation points, and these techniques only work in regions close to the base-station where the quality of the communication channel is already good. Other approaches like transmit beamforming and multiuser-MIMO are power-limited and require a large number of spatially separate antenna array elements.

Fundamentally, in order to improve capacity, a wireless system must maximize the link quality and suppress noise and interference between the transmitters and receivers in the network. This dissertation explores the concept and experimental validation of link-adaptive or modal antenna systems, consisting of a single fed antenna structure, RF switch, and algorithm. The antenna system uses active RF switching to adjust its radiation state to the multipath propagation environment and provide a peak signal at the transceiver. We investigate the impact of modal antennas from a wireless communication systems perspective: RF front end and baseband integration, multipath fading, and network performance. The analysis is extended from SISO to MIMO systems with one or more active elements. We compare active modal antennas with standard passive antennas in the context of mobile cellular handsets and WLAN access points and client devices. Depending on the application, we have tailored algorithms based on the device usage and propagation environment.

This research contributes to the state of the art in wireless communication systems by integrating several cross-disciplinary areas, such as antenna design, signal processing, electromagnetic wave propagation and fading, and software systems. We begin with a theoretical

and practical discussion of novel algorithms designed to integrate modal antennas using real-time channel state information feedback from the device baseband communications processor. We discuss how to optimize these algorithms to achieve good performance in both slow-fading and fast-fading environments. We then present cellular field test results with thousands of hours of data collected using a handset equipped with a modal antenna. To the best of the authors knowledge, this constitutes the first comprehensive measured results of radiation pattern switching antennas in mobile terminals on a live cellular network.

We extend the antenna system architecture and analysis to wireless LAN systems and indoor fading environments. The novel modal antenna algorithms are further generalized to cover MIMO point-to-multipoint systems, such as access points equipped with one or more modal antennas serving multiple users in a network. We believe that the systems described in this dissertation make a strong argument for embedding adaptive modal antennas in mobile devices as a practical and effective method to increase both spectral efficiency and link reliability of a wireless network.

To my mother Merry Roe.

Contents

List of Figures

List of Tables

Acknowledgments

Chapter 1

Background

1.1 The Wireless Communication Channel

Over the past two decades, wireless communication systems have experienced explosive growth driven by universal consumer adoption of smartphones, tablets, access points, Internet of Things (IoT) devices, and the ubiquity of wireless standards, such as Long Term Evolution (LTE), WiFi, and Bluetooth. Widespread usage of mobile wireless broadband internet, consisting of web-browsing, email, and high-definition audio and video streaming, is creating significant challenges for wireless service providers. Existing wireless networks are running out of capacity due to the limited supply of frequency spectrum. Thus, more efficient air-interface techniques are necessary to support the ever-increasing bandwidth requirements mobile devices pose on a wireless network.

The fundamental design goal of a wireless network is to optimize the capacity of the communication nodes by maximizing the desired signal and minimizing unwanted noise and interference. The signal-to-interference-plus-noise ratio (SINR) gives the upper bound of the wireless channel capacity. For example, consider two point sources communicating within a network (Figure 1.1). Noise in the system may be generated by thermal motion of charged particles in the electronics, imperfect RF components in the radio transmit and receive chains, or the statistical nature of the wireless channel itself. Interference may be caused by adjacent transmitters in the wireless network on the same time and frequency channels. Mitigating this type of interference requires careful planning and installation during the network design phase. Even so, some interfering sources, such as microwave ovens interfering with a home WiFi network, may be unpredictable in nature. Noise and interference degrade the overall signal quality of nodes in a wireless network.

Furthermore, wireless communication systems are limited by the environment in which the radio waves propagate. The line of sight between transmitters and the receivers is often obstructed by objects, such as buildings and walls. The signal may undergo small-scale fading due to local objects in the vicinity of the transmitter and receiver. The multiple paths taken by the signal before reaching the receiver can create time delays, phase shifts,
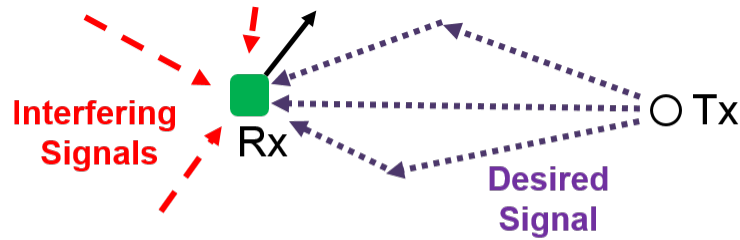
$$SINR = \frac{P_{RX}}{P_{Noise} + \sum_{i=1}^{N_{inter}} P_{RX_i}}$$

Figure 1.1: Model for signal-to-interference-plus-noise ratio (SINR) of two nodes in a communication network.

and attenuations that may combine destructively at the receiving antenna and degrade the link quality. To further complicate matters, these effects are often time-varying due to user motion.

Multiple-Input and Multiple-Output (MIMO) and antenna diversity schemes are known to mitigate the adverse effects of multipath propagation. Examples of antenna diversity are spatial diversity, pattern diversity, and polarization diversity. Antenna diversity may involve switching between antennas or combining the signal from multiple antennas. These techniques reduce the outage probability of a network. Alternatively, spatial multiplexing is a MIMO technique in which multiple data streams are transmitted independently using different spatial paths taken between multiple receive and transmit antennas. In other words, the spatial dimension is used to increase the capacity of the wireless channel. Other techniques, such as beamforming, increase the directionality of a multi-antenna array in order to overcome path loss and multipath fading. The beamformer adjusts the amplitude and phase of the signals at each antenna to achieve constructive or destructive interference of the propagating wave.

In this thesis, we will analyze another kind of antenna diversity - diversity from a single fed antenna element. The antenna (hereby referred to as a modal antenna) is able to generate multiple radiating states from a single antenna feed through active RF switching. The antenna system is also practical to fit into the form factor of an embedded device. The antenna system switches between the different radiating states to adapt to the varied propagation paths of the wireless channel to provide a peak signal at the transceiver. We will describe how this antenna technique can be used to address multipath fading and interference in the subsequent chapters. Moreover, we will describe how modal antennas can be used to further enhance existing spatial multiplexing and beamforming systems.
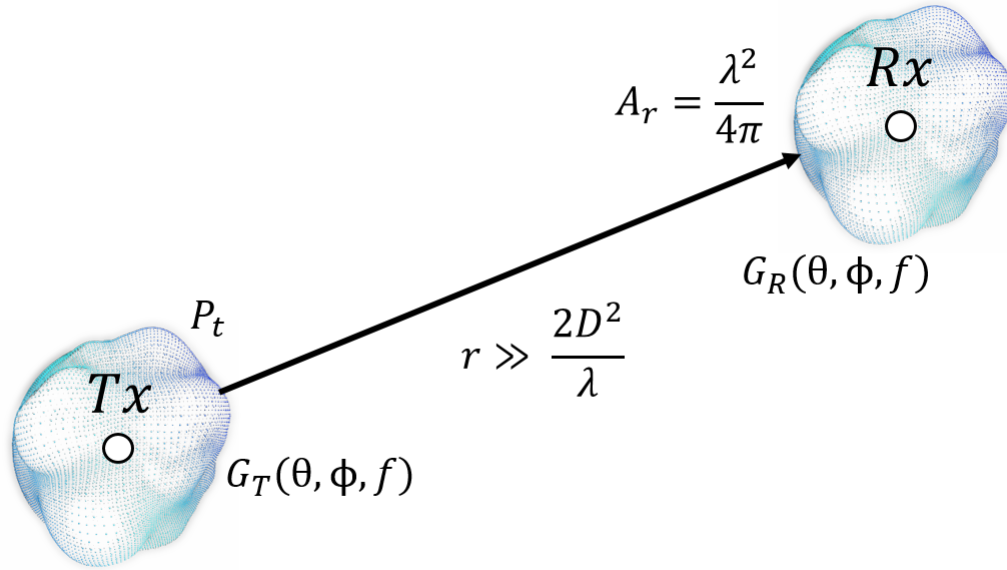
Figure 1.2: Free space path loss model for transmit and receive antennas.

1.2 Path Loss

The propagation of electromagnetic waves has significant influence on the design of communication systems. The signal between two nodes in a network is susceptible to noise, interference, scattering, reflections, diffractions, and attenuations from the wireless channel. The exact solution to the propagation of radio waves can be solved using Maxwell's equations with the proper boundary conditions. However, most propagation problems are intractable to solve this way, and statistical models are used instead. In this section, we introduce the theory for path loss and multipath fading, along with commonly used empirical models for indoor and outdoor propagation. These models are valuable to inform the design of the communication network. However, for actual network deployments, there is no substitute for actual field measurements of the wireless channel.

We start by first considering the case of a transmitter and receiver separated in free space by a distance r (Figure 1.2). For our analysis, we consider the far-field region of the antenna, in which the angular field distribution is independent of distance [7]. The far-field is the region of the antenna in which the transmitter and receiver are at a distance greater than $2D^2/\lambda$, where D is the length of the antenna and λ is the wavelength.

Because the field strengths in this region are independent of distance, we can compute the power of an ideal source that radiates equally in all directions using the time-averaged Poynting vector $\vec{W}$ [59]:

$$\vec{W_{avg}} = \frac{1}{2}Re[\vec{E} \times \vec{H^*}], \tag{1.1}$$

$$P_{rad} = \oint_S \vec{W} \cdot d\vec{s} = 4\pi r^2 W_{avg}. \tag{1.2}$$

The transmitting antenna produces a power density per unit area of $\vec{W}(\theta, \phi, f)$. We can account for the anisotropic radiation pattern of the transmit antenna by including the factor $G_t(\theta, \phi, f)$. Hence, the power density depends on the gain of the transmit antenna $G_t(\theta, \phi, f)$ in the given direction, the power of the transmitter P_t, and the distance r from the transmitter to the receiver:

$$W_{avg} = \frac{P_t}{4\pi r^2} G_t(\theta, \phi, f). \tag{1.3}$$

An antenna operating at a wavelength λ has a receiving aperture of A_r [57]:

$$A_r = \frac{G_r(\theta, \phi, f)\lambda^2}{4\pi}. \tag{1.4}$$

The power at the terminals of the receiving antenna are expressed in terms of the receive antenna effective area A_r, the transmit and receive antenna gains, $G_t(\theta, \phi, f)$ and $G_r(\theta, \phi, f)$, and the power from the transmitter:

$$P_r = A_r W_t = \left(\frac{\lambda}{4\pi r}\right)^2 G_t G_r P_t. \tag{1.5}$$

Equation (1.5) is referred to as the Friis transmission equation, and it is applicable for free-space link budget calculations. It is sometimes more convenient to express this equation in logarithmic form [18]:

$$P_{r,dBm} = P_{t,dBm} + G_{t,dB} + G_{r,dB} - 20\log_{10} r_{km} - 20\log_{10} f_{MHz} - 32.44. \tag{1.6}$$

where r is in units of kilometers and f is in units of MHz. $P_{r,dBm}$ and $P_{t,dBm}$ are the receive and transmit powers in units of decibels relative to one milliwatt.

The free space path loss term is:

$$L_{fs,dB} = -20\log_{10} r_{km} - 20\log_{10} f_{MHz} - 32.44. \tag{1.7}$$

For non-free space environments, the Friis transmission equation can be further extended to account for losses in the transmission medium and from polarization mismatch between the transmitting and receiving antennas:

$$P_{r,dBm} = P_{t,dBm} + G_{t,dB} + G_{r,dB} + L_{fs,dB} + L_{med,dB} + L_{pol,dB}. \tag{1.8}$$

We will explore the role of the radiation patterns $G_t(\theta, \phi, f)$ and $G_r(\theta, \phi, f)$ in section 1.5. However, in reality, the antenna patterns alone are not sufficient to describe the power at the receiver. The patterns must be combined with the scattering from the complex multipath propagation channel.

The Friis transmission equation can be extended for different radio wave environments using empirical models that account for macroscale propagation effects. These empirical models provide a theoretical treatment for how the electromagnetic waves will propagate for a given environment. The models provide the communication system designer with a way to estimate the coverage area for a wireless network. Because empirical models do not account for the exact geometrical description of objects (e.g. trees, buildings, walls) in the environment, they should not be used to calculate field strength at precise locations.

The Okumura model is an empirical model used to describe fading in large urban macro-cells [38]. Okumura developed the model from measurements of base station to mobile terminals in Tokyo. The model fits empirical curves to calculate path loss based on mobile terminal and base station heights for different outdoor fading environments: metropolitan, suburban, and rural areas. The model is applicable over distances of 1-100 km and frequencies of 150-1920 MHz. The path loss formula for the Okumura model is:

$$L_{Okumura,dB} = L_{fs,dB} + A_{mu,dB}(f,r) - G_{dB}(h_{Tx,m}) - G_{dB}(h_{Rx,m}) - G_{Area,dB}(f,r) \quad (1.9)$$

where r is the distance between the transmitter and receiver, $A_{mu,dB}$ is the median attenuation across all environments, $G_{dB}(h_{Tx})$ is the base station antenna height gain factor, $G_{dB}(h_{Rx})$ is the mobile terminal height gain factor, and $G_{Area,dB}(f,r)$ is the gain factor derived from the empirical plots recorded by Okumura:

$$G(h_{Tx,m}) = 20\log_{10} h_{Tx,m}/200, \quad 30m < h_{Tx} < 1000m, \quad (1.10)$$

$$G(h_{Rx}) = \begin{cases} 10\log_{10}(h_{Rx}/3) & h_{Rx} \leq 3m \\ 20\log_{10}(h_{Rx}/3) & 3m \leq h_{Rx} \leq 10m. \end{cases} \quad (1.11)$$

Curves for $G_{Area,dB}(f,r)$ and $A_{mu,dB}(f,r)$ as a function of frequency and distance can be obtained from reference [38].

The Hata model is a empirical formulation of the Okumura model that also accounts for diffraction, reflection, and scattering from buildings and includes loss factors for suburban and rural macrocells [20]. The Hata model greatly simplifies the empirical path loss computation by fitting Okumura's measured curves for $G_{Area,dB}(f,r)$ and $A_{mu,dB}(f,r)$ with an analytical expression [34]:

$$L_{Hata,dB} = A + B\log_{10}(r_{km}) + C. \quad (1.12)$$

The parameters A and B depend on the frequency, and antenna height:

$$A = 69.55 + 26.16\log(f_{MHz}) - 13.82\log(h_{Tx,m}) - \alpha(h_{Rx,m}), \quad (1.13)$$

$$B = 44.9 - 6.55\log(h_{Tx}). \quad (1.14)$$

The parameters C and $\alpha(h_{Rx})$ depend on the fading environment. For small and medium-sized cities,

$$\alpha(h_{Rx}) = (1.1\log_{10}(f_{MHz}) - 0.7)h_{Rx} - (1.56\log_{10}(f_{MHz}) - 0.8), \tag{1.15}$$

$$C = 0. \tag{1.16}$$

For metropolitan areas:

$$\alpha(h_{Rx}) = \begin{cases} 8.29(\log_{10}(1.54h_{Rx,m}))^2 - 1.1 & f \le 200MHz \\ 3.2(\log_{10}(11.75h_{Rx}))^2 - 4.97 & f \ge 400MHz, \end{cases} \tag{1.17}$$

$$C = 0. \tag{1.18}$$

For suburban areas:

$$C = -2(\log_{10}(f_{MHz}/28))^2 - 5.4. \tag{1.19}$$

For rural areas:

$$C = -4.78(\log_{10}(f_{MHz}/28))^2 + 18.33\log_{10}(f_{MHz}) - 40.98. \tag{1.20}$$

The Okumura-Hata model describes the path loss for several terrains. However, the model assumes that the terrain profile varies slowly, which may not be accurate for most urban environments. Other models [6], [29], [50] have attempted to correct for sharp variations in terrain. The most popular of these correction models is COST 231, which also extends the model to frequencies above 2 GHz [17]. The Walfisch/Bertroni model factors in diffraction from rooftops and buildings [65].

The generalized path loss simplifies the number of parameters in the path loss calculation to a fixed fading factor and the rate of change of the propagating waves across distance [51]. The generalized model is often good enough for quick calculations and tradeoff analysis for common fading environments. The simplified path loss model can be expressed as:

$$P_r = P_t K \left(\frac{r_0}{r}\right)^n, \tag{1.21}$$

or in logarithmic form

$$P_{r,dBm} = P_{t,dBm} + K_{dB} - 10n\log_{10}\left(\frac{r}{r_0}\right). \tag{1.22}$$

where K is a constant that depends on the average channel attenuation, n is the path loss exponent, and r_0 is the distance to the antenna far field. The path loss exponent is a function of frequency, environment, and obstacles. Table 1.2 shows typical values for the path loss and attenuation factors.

Table 1.1: Generalized path loss model parameters for common environments [52], [13], [43], [14], [47].

Environment	n	K (dB)
Store	1.8 - 2.2	5.2 - 8.7
Office	2.4 - 3.0	7.0 - 14.1
Factory	1.6 - 2.0	3.0 - 7.0
Home	2.8 - 3.5	5.0 - 10.2
Urban	2.7 - 3.5	7.1 - 13.1
Suburban	3.8	13.25
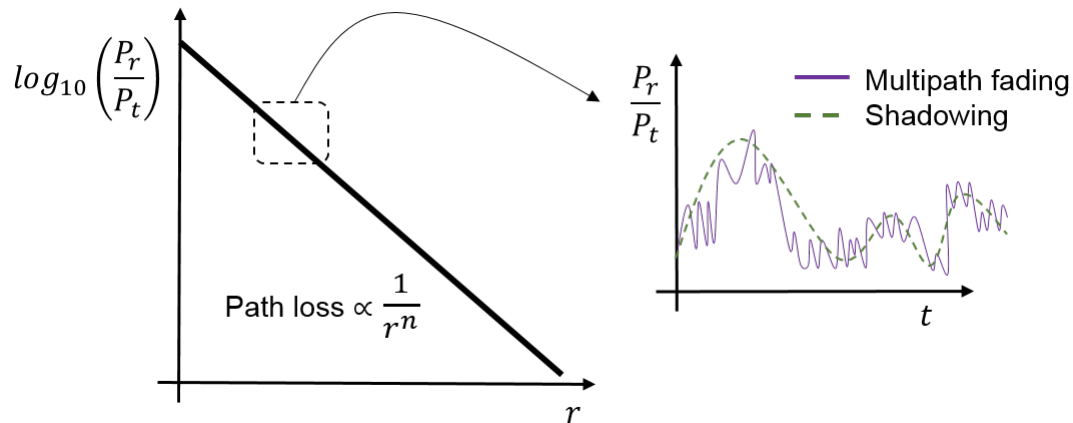
Figure 1.3: Free space path loss falls off with the square of the distance between the transmitter and receiver. When the receiver and transmitter are separated by some distance r, shadowing and multipath fading may introduce slow and fast fluctuations in the received power.

1.3 Multipath Fading

In addition to pathloss, electromagnetic waves propagate in multiple directions from the transmitter to the receiver. The waves may bounce off of walls and buildings creating delays, attenuations, and phase shifts. Objects that are large relative to the wavelength of the communication system introduce shadowing or slow fading. Local scatters or physical movement of the communication devices will create faster multipath fading. The fast and slow time scales are measured relative to the coherence bandwidth or the multipath time delay spread of the channel. Figure 1.3 shows how the combination of path loss, shadowing, and fast multipath fading affect the power at the receiver as a function of distance and time.

Ray tracing provides a simple way to model the multipath of electromagnetic waves by propagating narrow beams and analyzing the interaction with local objects in the environment. Figure 1.4 shows a scenario in which the path between transmit and receive antennas
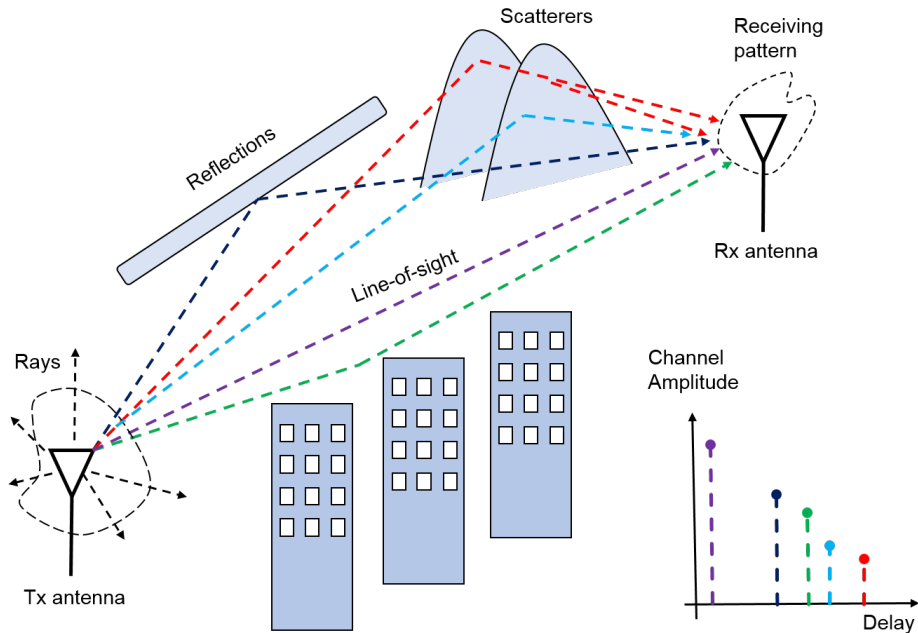
Figure 1.4: Ray tracing model of multipath propagation.

is blocked by reflectors and scatterers. The rays propagating out of the transmitter can be modeled as having an amplitude that is derived from the radiation pattern gain at a particular angle of the transmit antenna. Furthermore, the rays are attenuated and delayed due to the channel by the time they reach the receiver. Rays that are reflected and scattered reach the receiver at later times and are more attenuated than the line of sight path.

By itself, ray tracing does not account for wave characteristics like diffraction and interference. However, ray tracing models may be supplemented with the Geometric/Uniform Theory of Diffraction (GTD/UTD). GTD is used to describe the interaction of rays diffracting near or around local surfaces or edges [25]. UTD extends GTD to account for wave diffraction in the presence of shadow and reflection boundaries [27]. Given a precise description of the electromagnetic properties, size, and position of scatters in a communication system, one can use ray theory and UTD to predict radio wave propagation and delay spread to inform network design and planning. However, this information is specific to a particular transmitter and receiver configuration and does not apply to all propagation environments.

It is often convenient for system designers to describe the wireless channel as a linear time-invariant system. In this model, each path i of the wireless channel introduces a unique delay τ_i and attenuation a_i by the time it reaches the receiver. The time-varying channel h can be written using a tapped-delay line model:

$$h(\tau, t) = \sum_i a_i \delta(\tau - \tau_i(t)) \tag{1.23}$$

where each resolvable channel path is represented by a delta function. Modeling each tap as a discrete delta function is a good approximation when there are a small number of reflectors that contribute to the channel fading. Two paths may be resolvable from each other if their delay difference is greater than the inverse of the signal bandwidth W:

$$\tau_1 - \tau_2 >> \frac{1}{W}. \tag{1.24}$$

Using this channel model, the received signal $y(t)$ from an input $x(t)$ can be written as:

$$y(t) = \sum_i a_i x(t - \tau_i(t)) + w(t). \tag{1.25}$$

Equation (1.25) also includes a time-varying factor $w(t)$ to account for random noise introduced by the statistical nature of the wireless channel. The channel impulse response can also be converted to the frequency domain using the Fourier transform:

$$H(f,t) = \int_{-\infty}^{\infty} h(\tau,t)e^{-2j\pi f\tau}d\tau = \sum_i a_i(t)e^{-2j\pi f\tau_i(t)}. \tag{1.26}$$

We can express the channel capacity of the system in units of bits per second per hertz [62]:

$$C = \log_2\left(1 + |h|^2 SNR\right) \quad bps/Hz. \tag{1.27}$$

In the time-domain, multipath reflections may interfere constructively or destructively causing the signal to fluctuate between peaks and nulls at the receiver. A similar interpretation exists in the frequency domain. Frequency-selective fading occurs when two or more paths partially cancel one another at the receiver. This result in nulls in the frequency response of the received signal. That is, each of the frequency components of the signal may undergo different amounts of fading as they pass through the wireless channel. Alternatively, flat fading occurs when all frequencies within the bandwidth of the signal undergo the same attenuation at the receiver. Flat fading is caused by shadowing or other slow-fading characteristics of the channel.

The multipath channel may also be characterized in the angular domain. In this interpretation, the radio waves exit the transmitter at multiple angles of departure, and reach the receiver at multiple angles of arrival. Consider a three-dimensional propagation channel with azimuthal angle $\phi \in [0, 2\pi]$ and polar angle $\theta \in [0, \pi]$. To simplify the notation, we group the azimuthal and polar angles into a single parameter Φ. The path i is represented by the following parameters $a_i, \Phi_{Tx}, \Phi_{Rx}$ in the angular domain, where Φ_{Tx} and Φ_{Rx} constitute the azimuth and elevation angles for the transmitter and receiver, respectively. We can write the channel response in the angular domain for path i as [48]:

$$h(\Phi_{Tx}, \Phi_{Rx}) = \sum_i a_i \delta(\Phi_{Rx} - \Phi_{i,Rx})\delta(\Phi_{Tx} - \Phi_{i,Tx}) \tag{1.28}$$
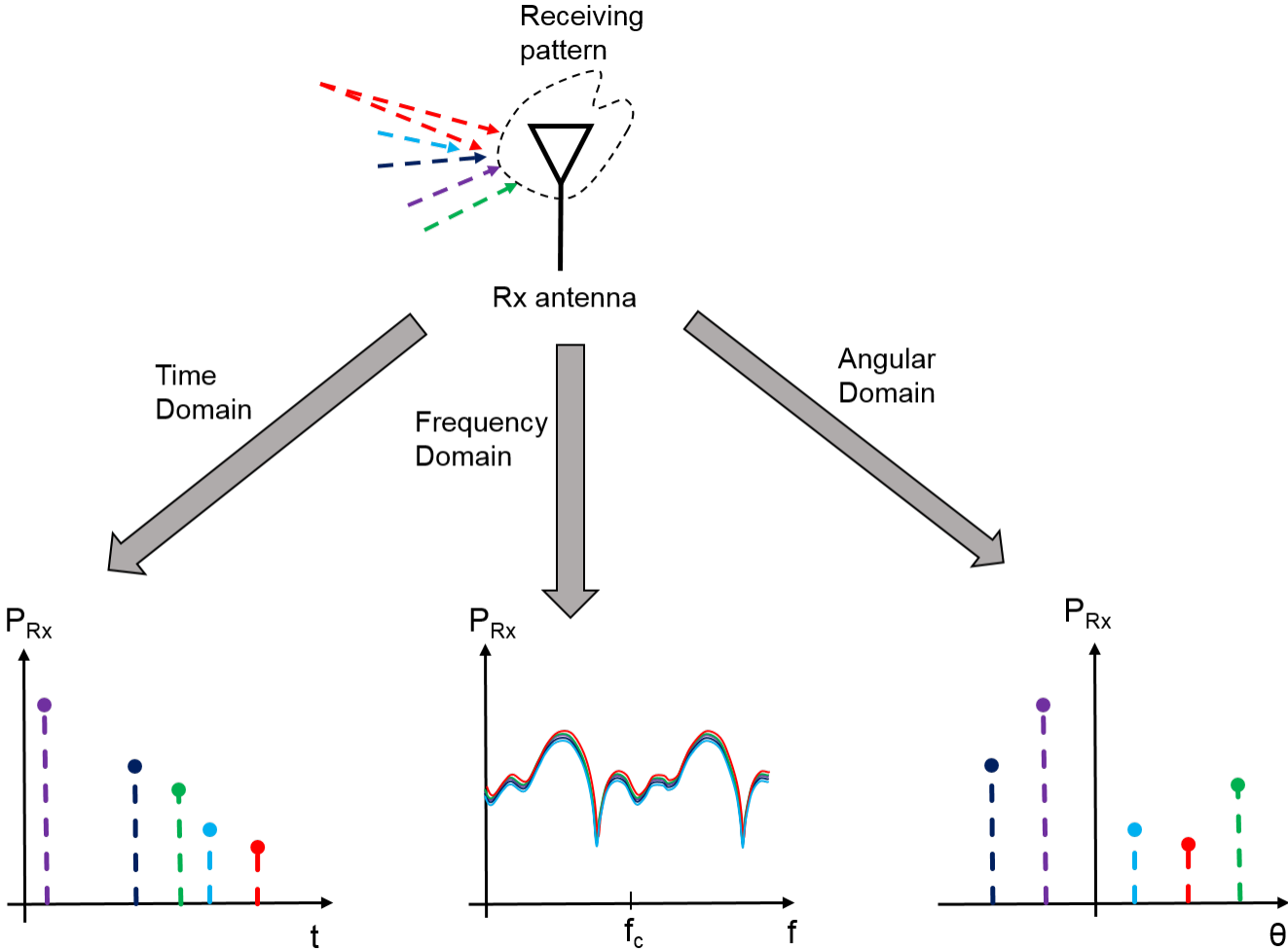
Figure 1.5: Physical domains for modeling multipath. Time domain (left), frequency domain (center), and angular domain (right). Paths may arrive at the receiver at different angles and time delays. These paths may also combine constructively or destructively at different frequencies, creating a frequency-selective fading response.

where $\delta(\Phi_{Rx} - \Phi_{i,Rx})$ and $\delta(\Phi_{Tx} - \Phi_{i,Tx})$ represent the angular taps at the transmitter and receiver, respectively.

Common cellular and indoor channel models may use statistical distributions to describe the transmitter and receiver angular spreads. For more details on angular channel distributions, we refer the reader to [8], [32], [56], [15]. How the channel interacts with the transmitter and receiver radiation patterns $G_{Tx}(\theta, \phi)$, $G_{Rx}(\theta, \phi)$ in the angular domain is of utmost importance for the design of link-adaptive antennas. We will explore this topic further in subsequent sections.

1.4   MIMO Antenna Techniques

A key feature of any wireless system is to adapt to the channel to maintain reliable communication. Multiple-input-multiple-output (MIMO) is one such channel adaptation method, in which one or more antennas is used at the transmitter or receiver. MIMO can be subdivided into three categories: diversity, precoding or beamforming, and spatial multiplexing. Spatial antenna diversity consists of placing multiple antennas at the transmitter or receiver separated by some distance such that each antenna is less likely to experience a weak signal due to fading. Precoding or beamforming involves sending the same signal from multiple transmit antennas and combining their gain and phase to maximize the signal at the receiver. Spatial multiplexing exploits the spatial dimensions or multipaths of the channel to send independent data streams. Diversity and precoding may be used to reduce outage probability of the communication channel, whereas spatial multiplexing increases the overall capacity.

Diversity

Spatial antenna diversity may be implemented at the receiver and/or transmitter. Both methods require some way to combine the multiple signals to minimize the outage probability. The effectiveness of a diversity system can be measured by its diversity gain. Diversity gain is defined as the power gain for a diversity system to achieve a given system outage probability compared to a non-diversity system (Figure 1.6).

Space time block coding (STBC) and cyclic delay diversity (CDD) are the most common forms of transmit diversity. STBC applies a complex precode at different times to the copies of the signal sent by each antenna, such that the receiver may decode each stream independently. Space-time codes are designed to maximize diversity gain without sacrificing data rate. The most popular STBC was designed by Alamouti for two-antenna diversity systems [2]. Alamouti's code acheives a diversity gain of 3 dB without sacrificing data rate. Tarokh et. al. extended the space of STBCs to support more than two antennas and showed that all higher order STBCs must sacrifice data rate in order to acheive orthogonality between signals from different antennas [60].
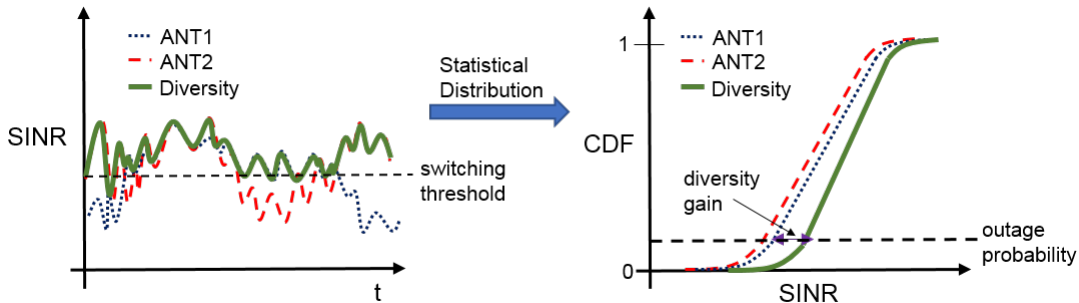
Figure 1.6: Example of receive antenna switching diversity. Plot of SINR vs. time for two antennas (left). When the signal quality of antenna 1 falls below a threshold, the receiver switches to antenna 2 to maintain the link quality. The diversity gain of the system can be read off of the cumulative distribution function (right) of the SINR at the outage probability.

CDD is a frequency diversity technique in which signals from each transmit antenna are delayed in time to reduce correlation between multiple antennas. Each antenna sends phase-shifted copies of the same signal such that the copies combine non-coherently at the receiver. The time domain phase shifts reduce the likelihood of frequency selective fading in which signals may combine destructively at the receiver. The receiver requires no additional complexity to decode the CDD signal from the transmitter.

Receiver diversity schemes use multiple antennas at the receiver. The antennas are spaced apart such that the transmitted signal takes different paths to each antenna, thereby reducing the outage probability. Receive diversity requires a processing technique, such as switching, selecting, or combining, to recover the signal.

Switching is the simplest form of receive diversity in which one antenna is used until the signal level falls below a threshold, at which point the system switches to another receive antenna. Selecting is the process by which the diversity system makes pre-measurements on all antennas to determine the antenna with maximum signal quality to present to the receiver. The primary drawback of selecting is that it require a training process in order to determine which antenna to select. It is critical to keep this training period short to minimize signal disruption at the receiver. Alternatively switching and selecting may use a dedicated receiver at each antenna so as to make a measurement of signal quality without interrupting the path to the primary receiver. However, this approach comes with higher cost, complexity, and power consumption.

Consider the selection diversity scheme with M receive antennas, which requires an SINR of γ_t to maintain a target outage probability of ρ. The cumulative distribution function of the outage probability of the diversity system is:

$$P_{out} = P(p_{out} > \rho) = P(\gamma_{selection} < \gamma_t) = P(\max(\gamma_1, \gamma_2, ..., \gamma_M) < \gamma_t). \qquad (1.29)$$

If the antennas are spaced far apart relative to the wavelength of the signal, it can be

assumed that each antenna fades independently. Hence, the cumulative distribution function (CDF) of the diversity system simplifies to the product of all outage probabilities:

$$P(p_{out} > \rho) = \prod_{i=1}^{M} P(\gamma_i < \gamma_t). \tag{1.30}$$

In order to analyze the impact on outage probability, we need a model for the wireless channel. The Rayleigh distribution is a reasonable model if there are a large number of scatterers in the environment and no one scatterer dominates. In this case, the channel impulse response can be modeled as a Gaussian process. It is well known that such a distribution has outage probability [42]:

$$P_{out}(\gamma_i) = 1 - e^{-\gamma_i / \mathrm{E}\langle \gamma_i \rangle} \tag{1.31}$$

where $\mathrm{E}\langle \gamma_i \rangle = \Gamma$ is the average SINR for the ith antenna, Γ_0 is the average SINR for a single antenna, and $\Gamma_{selection}$ is the average SINR for selection diversity:

$$\Gamma_{selection} = \Gamma_0 \sum_{i=1}^{M} \frac{1}{i}. \tag{1.32}$$

Hence, for M-antenna selection diversity we obtain the outage probability:

$$P_{out}(\gamma_i) = (1 - e^{-\gamma_i/\Gamma})^M. \tag{1.33}$$

In addition to switching and selecting, combining is a diversity technique that presents all antenna chains to the receiver at once and adjusts the contribution of each antenna to maximize SINR. Examples of combining are equal gain combing (EGC) and maximum ratio combining (MRC). Figure 1.8 shows the system block diagrams for these diversity techniques.

EGC coherently combines the signal from each antenna with an equal weighting $w_i = e^{-j\phi_i}$ and assumes an equal interference and noise for the channel of each antenna. MRC also accounts for interference and noise on each antenna path. Antennas which degrade the overall SINR are given smaller weights. Therefore, MRC optimally combines each of the channels. Because the SINR is maximized when the weight of each antenna is proportional to its channel ($w = h$), the receive SINR for MRC becomes the sum of SINRs for each antenna:

$$\gamma_{MRC} = \gamma_0 \sum_{i=1}^{M} \gamma_i. \tag{1.34}$$

Similarly, it can be shown that the SINR gain for EGC is lower because the signal from each antenna is weighted equally [43].

$$\gamma_{EGC} = \gamma_0 \left[1 + (M-1)\frac{\pi}{4}\right]. \tag{1.35}$$
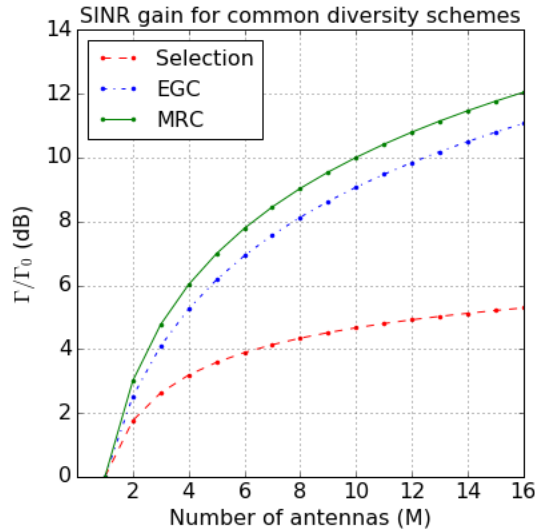
Figure 1.7: SINR increase for common diversity schemes. Adding more antennas provides a diminishing return on SINR gain. MRC achieves optimal diversity combining. EGC comes close to MRC without accounting for noise on each chain. If the received signals do not contain much noise, selection diversity does not perform as well because only one antenna chain at a time may contribute to the overall signal. However, EGC may perform worse than selection diversity if one of the received signals contributes more noise to the total system SINR [39].

Note that the SINRs for MRC and EGC both increase linearly with M. In terms of complexity, switching and selection diversity are the simplest. MRC and EGC both require estimation of the channel response in order to compute the antenna weights. Furthermore, in order to combine the antenna signals, MRC and EGC require multiple receiver front ends (e.g. amplifiers, filters, etc.) for each antenna in the system, resulting in higher power consumption, higher cost, and more volume required for the electronics. In practice, the size constraints of embedded devices, such as mobile handsets, make antenna diversity techniques with more than two or four antennas unmanageable.

Beamforming

Beamforming is an antenna array technique in which the same signal is combined in-phase at multiple antennas to achieve a power gain. The phase adjustment may occur in the RF domain, or in the digital domain, after downconversion to baseband. Beamforming can be implemented at the transmitter or the reciever. Receive beamforming is similar to EGC and MRC in that the same receive signal is combined constructively at multiple receive antennas. Receive beamforming is applicable for single-input-multiple-output (SIMO) channels.
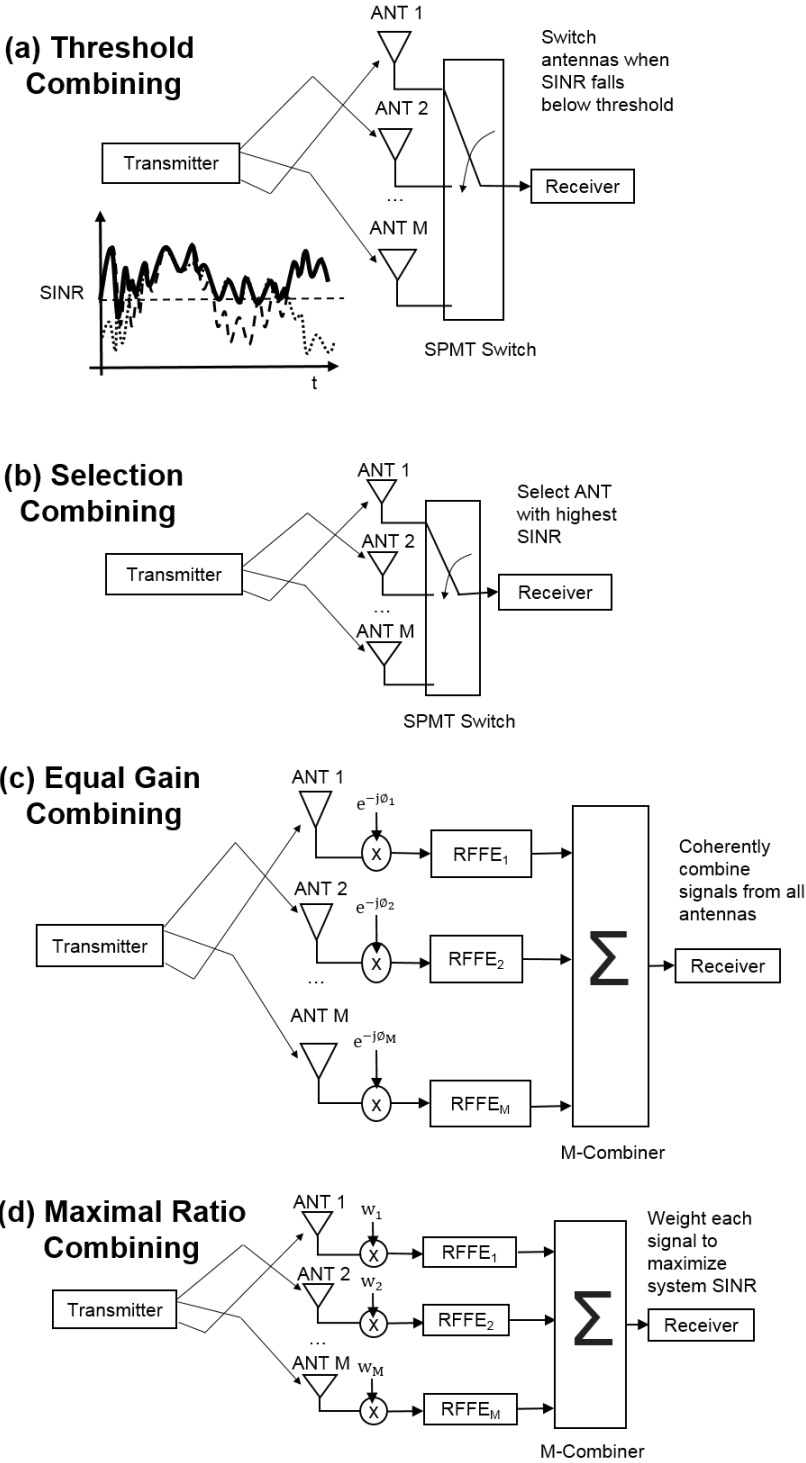
Figure 1.8: System block diagrams for (a) threshold diversity, (b) selection diversity, (c) EGC, and (d) MRC.

Transmit beamforming, sometimes called pre-coding, involves adjusting the amplitude and phase of the transmit signals based on channel state feedback from the receiver. Transmit beamforming applies to multiple-input-single-output (MISO) channels. Figure 1.9 illustrates these beamforming architectures.

Beamforming not only provides a power gain for the desired signal, but may also be used to adapt the nulls of the channel for interfering signals. Adpative beamforming arrays use a signal processing technique, such as MUSIC [71] or ESPIRIT [46], to determine the angle of arrival of signals of interest (SOIs) and signals not of interest (SNOIs) or interferers.

While beamforming does provide a power gain, there are some drawbacks. Beamforming systems require multiple RF circuits and multiple antennas spaced at least a half wavelength apart. Hence, size is a key limitation for the effectiveness of multi-antenna arrays, especially in mobile systems. Just as with antenna diversity, the power gain from beamforming scales as the logarithm of the number of antennas. Furthermore, beamforming requires one RF front end per antenna array element, and this comes with increased size and power consumption. As an example, for WLAN transmit beamforming, each power amplifier consumes hundreds of milliamperes. In other words, four or eight antenna beamforming requires a power supply that can source one to two amps just for the RF front end.

Furthermore, because beamforming increases the peak antenna array gain, system designers must take care not to violate radiated power, specific absorption rate (SAR), and spurious emissions requirements. For example, in the U.S. and Europe, the Federal Communications Commission (FCC) and the European Telecommunications Standards Institute (ETSI), regulate the maximum equivalent isotropic radiated power (EIRP) for outdoor and indoor communications. EIRP is defined as:

$$EIRP_{dBm} = P_{Tx,dBm} + G_{peak,dB}. \tag{1.36}$$

The FCC and ETSI assume a worst case maximum radiated power when regulating wireless transmitters. Actual antennas may only have a peak gain over a narrow angular region. This means that transmit beamforming systems must back off their transmit power even when the antenna system is in a fade. This back-off limits the overall power gain provided by beamforming.

Beamforming systems are only as effective as the antenna elements in the array. To simplify the analysis, it is often assumed that each array element is omni-directional, but this is not the case for real systems. Consider a two-antenna receive beamforming system, in which the dominant angle of arrival of the signal is in the direction (θ_0, ϕ_0). The maximum beamforming gain G_{bf} with perfect channel knowledge is:

$$G_{bf} = G_{Rx,1}(\theta_0, \phi_0) \times G_{Rx,2}(\theta_0, \phi_0) \tag{1.37}$$

where $G_{Rx,1}$ and $G_{Rx,2}$ are the antenna gains at the angle (θ_0, ϕ_0).

Equation (1.37) indicates that in order to maximize beamforming gain, each individual antenna element must each be providing a peak signal at the receiver and be adaptive to
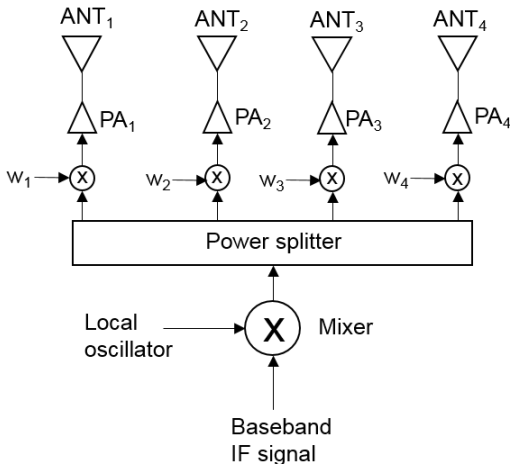
Transmit Beamforming (Analog)
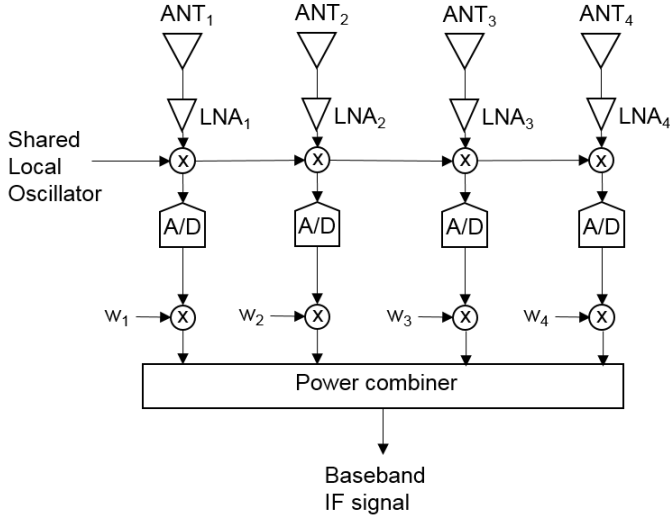
Receive Beamforming (Digital)

Figure 1.9: Beamforming architectures: transmit beamforming in the analog domain (top) and receive beamforming in the digital domain (bottom), for example. Both transmit and receive beamforming may occur in either the digital or analog domain.
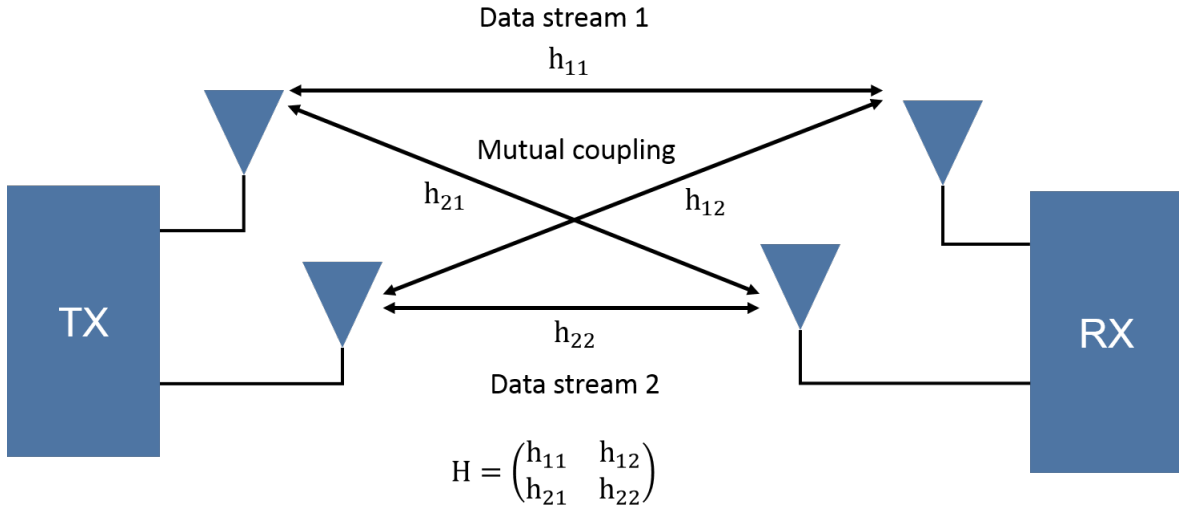
Figure 1.10: MIMO system with 2 transmit and 2 receive antennas and channel matrix H. The diagonal elements represent the channels for the separate spatial data streams. The off-diagonal elements represent the unwanted coupling between antennas or spatial data streams. An ideal MIMO channel would have zero-valued off-diagonal elements.

the varied polarization of the propagating waves. If one or more of the antennas is in a fade, beamforming will not provide much power gain compared to a single antenna system.

Spatial Multiplexing

We have seen that diversity and beamforming provide a power gain to improve SINR and reduce outage probability. In this section, we describe a technique called spatial multiplexing that uses the spatial dimension of the wireless channel to increase the system capacity. Spatial multiplexing exploits the MIMO channel to send different data streams between multiple transmit and receive antennas. We consider the MIMO channel with M_{Rx} receive antennas and M_{Tx} transmit antennas (Figure 1.10). The channel path between each of the transmit and receive antennas can be described by an $M_{Tx} \times M_{Rx}$ channel matrix $\mathbf{H}$:

$$\mathbf{y} = \mathbf{Hx} + \mathbf{w} \tag{1.38}$$

where $\mathbf{x}$ and $\mathbf{y}$ denote the transmitted and received signal vectors, respectively. The channel gain from transmit antenna j to receive antenna i is denoted by h_{ij}. The channel matrix can be decomposed into orthogonal eigenvectors using singular value decomposition:

$$\mathbf{H} = \mathbf{U\Lambda V}^*. \tag{1.39}$$

The diagonal elements λ_i represent the channel eigenvalues. We can re-write $\mathbf{H}$ by projecting onto the channel eigenvectors with $M_{min} = \min(M_{Rx}, M_{Tx})$:

$$\mathbf{H} = \sum_{i=1}^{M_{min}} \lambda_i \mathbf{u_i v_i^*}. \tag{1.40}$$

Projecting the transmit and receive signal along the same basis:

$$\widetilde{y}_i = \lambda_i \widetilde{x}_i + \widetilde{w}_i. \tag{1.41}$$

We can generalize the single-input-single-output (SISO) channel capacity from equation (1.27) for MIMO channels:

$$C = \mathrm{E}\langle \log_2 \left[det \left(\mathbf{I_{M_{Rx}}} + \frac{\mathbf{SNR}}{M_{Tx}} \mathbf{HH^*} \right) \right] \rangle. \tag{1.42}$$

Combining equations (1.42) and (1.40), we obtain:

$$C = \sum_{i=1}^{M_{min}} \log_2 \left(1 + \frac{P_i \lambda_i^2}{N_0} \right) \quad bps/Hz \tag{1.43}$$

where N_0 is the average channel noise and P_i is the transmit power allocated to the ith eigenchannel. Hence, spatial multiplexing provides a capacity increase proportional to M_{min}, the minimum number of antennas at the transmitter or receiver.

We can also interpret equation (1.43) by analyzing the rank and condition number of the channel matrix $\mathbf{H}$. The rank, k, of the matrix is the number of non-zero eigenvalues. Physically, this means that the number of spatial paths or scatters in the channel must be greater than or equal to M_{min}. If the receiver is not able to sufficiently de-correlate the signals from each transmit antenna, the channel cannot be exploited for a capacity enhancement. The rank of the channel matrix depends on the wavelength and the number of scatters in the environment. The channel matrix is said to be full rank if $k = M_{min}$. The condition number n of the channel matrix is the ratio of the maximum eigenvalue to the minimum eigenvalue:

$$n = \frac{\max_i \lambda_i}{\min_i \lambda_i}. \tag{1.44}$$

Based on equation (1.43), in the high SINR regime, the capacity is maximized when all channel eigenvalues are equivalent. In other words, spatial multiplexing is not effective if the channel qualities are imbalanced between spatial streams. In section 1.5, we will explore what this means in terms of antenna design for MIMO systems.

One drawback for spatial multiplexing systems is that an individual RF transceiver is required for each data stream, leading to an increase in design size, cost, and power consumption. As with antenna diversity, the antennas must be well-isolated with low correlation between patterns. Implementing higher order MIMO systems may not be feasible for embedded devices without enough volume for the required antenna separation. Furthermore, a high SINR is required for the receiver to estimate the channel and decorrelate the signal from

each spatial stream. As path loss and fading increase for larger distances between the transmitter and the receiver, the communication system is better off reducing the number of data streams. For low SINR, the power gain from diversity and beamforming methods is a more optimal use of the MIMO channel to guarantee a target SINR for reliable communication.

1.5   Antenna Parameters

The antenna radiation pattern defines the variation of radiation intensity or gain as a function of spherical angle. In the far-field region of the antenna, the radiation pattern can be visualized as a three-dimensional surface where the radiation intensity varies over angle. An isotropic radiation pattern has the same gain over all spherical angles. Isotropic antennas do not exist in practice, but they are used for comparison purposes. The radiation pattern gain is typically measured on a logarithmic scale in decibels (dBi) relative to an isotropic antenna. In this thesis, when we refer to antenna gain in dB, it is implied that we are expressing the gain relative to an isotropic antenna. Radiation patterns vary across frequency and aspect angle. High gain regions of the radiation pattern may have positive gain (higher than 0 dBi) and low gain regions may have negative gain (less than an 0 dBi). It is important to note that the antenna does not create additional power or gain relative to its input. The radiation pattern just defines how the antenna directs its energy in 3-D space.

Dipoles are the most commonly used type of antenna. In its simplest form, a dipole consists of two conducting arms that are each a quarter wavelength long with an oscillating RF current applied at the center between the two arms. The oscillating charge produces an ideal radiation pattern that is the shape of a donut with peak gain of 2 dBi along the azimuth plane. The two poles of the dipole contain nulls where the dipole current distribution goes to zero. A monopole antenna may be formed from a conductive wire sitting on top of a ground plane. The ground plane acts as a reflector taking the energy that was radiated underneath the antenna and re-directing that energy around the azimuthal plane. Hence a monopole has twice the peak gain (5 dBi) of the dipole. Figure 1.11 shows the peak gain and radiation patterns for dipole and monopole antennas.

It is important to consider that the ideal antenna radiation pattern is measured in an anechoic or non-reflecting environment. The shape of the ideal radiation pattern does not exclusively determine how the waves will propagate in a reflective or cluttered multipath environment. In reality, the actual antenna radiation pattern is determined by the convolution of the ideal radiation pattern, as measured in an anechoic chamber, with the angular power distribution $A(\Phi)$ of the cluttered multipath channel [72]:

$$G_{actual}(\Phi) = \int_\Phi G_{ideal}(\Phi)A(\Phi - \Phi_0)d\Phi. \tag{1.45}$$

We will further analyze the concept of the antenna pattern in a cluttered environment in Chapter 2.
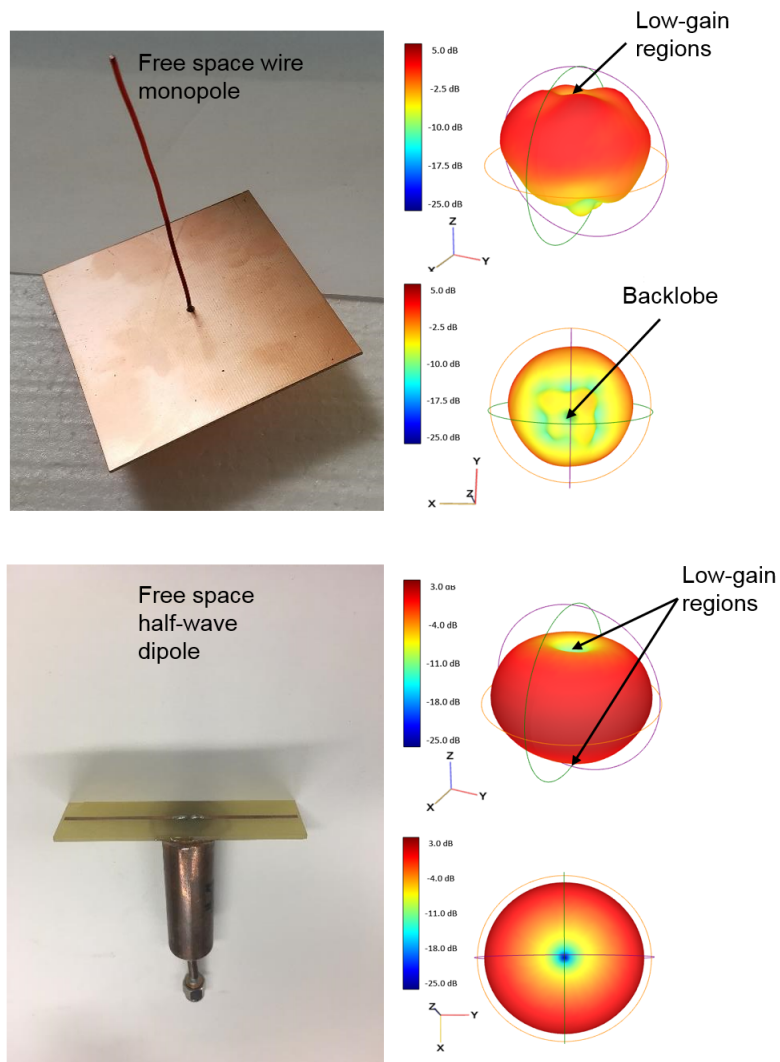
Figure 1.11: (a) Image of free space monopole and 3D radiation pattern at 2.4 GHz (top). The monopole antenna has 5 dBi peak gain around the azimuthal plane. The backlobe of the pattern comes from the reflected energy off of the ground plane. (b) Free space half-wavelength dipole and 3D radiation pattern at 2.6 GHz (bottom). The dipole antenna has peak gain of 2 dBi and is omnidirectional along the azimuth plane. The dipole has two deep nulls at the poles of the radiation pattern.

The polarization of an antenna is defined as the orientation of the electric field of the radiation pattern. As an electromagnetic wave propagates, the electric field may move linearly, circularly, or elliptically in space. If a receiving antenna has a polarization that is not matched to the electromagnetic wave it is receiving, there will be a polarization or power loss. Most mobile antennas are linearly polarized. The dominant portion of the polarization is the co-polarization term and the orthogonal component is the cross-polarization term. For line of sight radio links, it is advantageous to exactly match the polarization of the transmit and receive antennas to maximize power transfer. However, in environments with high levels of multipath, a better approach is to use an antenna with multiple polarizations. In this case, after leaving the transmit antenna, the wave may lose its pure sense of polarization as it bounces off of walls or buildings. By the time the wave reaches the receiver, the wave may look more elliptically polarized with power in both co- and cross-polarization components.

Antenna efficiency is defined as the ratio of radiated power to the power delivered at the antenna input. Efficiency is normalized to an isotropic antenna. An antenna with 100% or 0 dBi efficiency radiates all of the power at its input. An antenna with radiation intensity $F(\theta, \phi, f)$ has efficiency η:

$$\eta(f) = \frac{P_{rad}}{P_{in}} = \frac{\int\limits_{0}^{2\pi} \int\limits_{0}^{\pi} F(\theta, \phi, f) \sin\theta \, d\theta \, d\phi}{P_{in}}. \tag{1.46}$$

In reality, antenna efficiencies are degraded due to mismatch losses and conductive and dielectric losses in the antenna structure. This is especially true for embedded antennas, which may have reduced efficiency due to volume constraints [67], finite ground plane size, and metallic components such as shield cans and integrated circuits that reduce the total power radiated from the antenna structure [37]. It is well known from electrostatics that the dipole moment of the charge distribution of an antenna is the dominant portion of the far field radiation pattern. However, for size-constrained antennas, as in mobile handsets, the antenna may be smaller than the wavelength of operation and components on the ground plane of the antenna may distort the charge distribution, thereby canceling the dipole moment in particular directions. This creates low gain regions in the far field of the antenna, such that the radiation pattern may no longer appear as an ideal dipole pattern (Figure 1.12).

Antenna isolation and radiation pattern correlation are key metrics to characterize a multi-antenna system. Antenna isolation is defined as the amount of power transferred from one antenna that can be seen at the input of another antenna. For MIMO systems, it is advantageous to maintain high antenna isolation typically better than -20 dB (or 1%). Isolation is typically achieved by physically separating antennas in the same system. However, it may be difficult to achieve high isolation for embedded antennas that share the same ground plane in a limited volume, such as a cellular phone.

Antenna pattern diversity is classified into three categories: spatial diversity, pattern diversity, and polarization diversity (Figure 1.13). Spatial diversity represents the diversity of antenna patterns that are placed some distance apart. In these systems, antennas placed
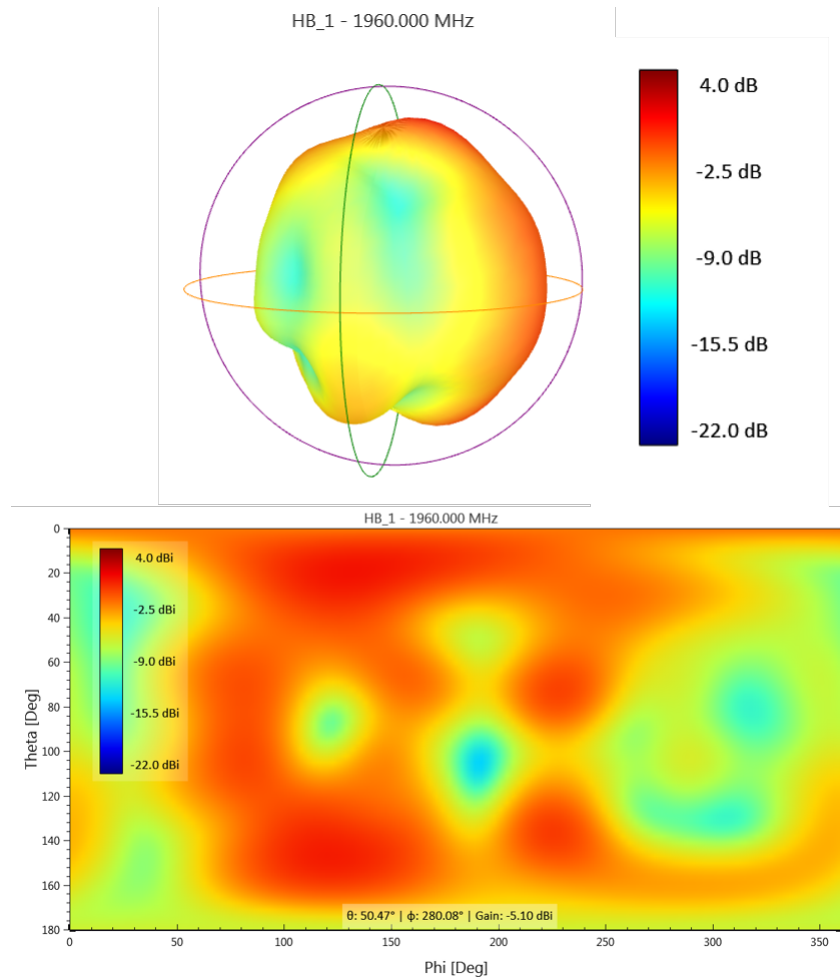
Figure 1.12: 3D plot of the radiation pattern of an embedded antenna (top). Bottom plot shows the surface plot of the radiation pattern with azimuth angle on the x-axis and elevation angle on the y-axis.

in separate positions will experience different peaks and nulls of the electromagnetic wave. Pattern diversity corresponds to antennas with distinct radiation pattern gain distribution across all aspect angles. A high degree of pattern diversity is desirable for MIMO systems. Polarization diversity is a kind of diversity that uses antennas with different electric field orientations. Polarization diversity may be achieved by placing antennas orthogonal to each other in a design. Because the electric field distribution is proportional to the radiation pattern gain, polarization diversity is a subset of pattern diversity.

Antenna envelope correlation coefficient (ECC) gives a measure of the similarity of radiation patterns of two antennas. ECC has a range of 0 to 1. Antennas with an ECC of 0 have radiation patterns that are perfectly de-correlated from one another, and antennas with an ECC of 1 have identical radiation patterns. For a MIMO antenna system, an ECC less than 0.5 is usually desired. For a linearly polarized antenna, we decompose the radiation intensity vector in terms of its vertical and horizontal components:

$$\vec{\boldsymbol{F}}(\theta, \phi, f) = \vec{\boldsymbol{F_\theta}} \cdot \hat{\mathbf{u}}_\theta + \vec{\boldsymbol{F_\phi}} \cdot \hat{\mathbf{u}}_\phi \tag{1.47}$$

where $\hat{\mathbf{u}}_\theta$ and $\hat{\mathbf{u}}_\phi$ are unit vectors in the θ and ϕ directions, respectively.

From this, we can express the ECC ρ_{12} between antennas 1 and 2 in terms of their radiation intensities:

$$\rho_{12}(f) = \frac{|\int \int \vec{\boldsymbol{F_1}} \cdot \vec{\boldsymbol{F_2^*}} \, d\theta \, d\phi|^2}{|\int \int \vec{\boldsymbol{F_1}} \, d\theta \, d\phi|^2 \cdot |\int \int \vec{\boldsymbol{F_2}} \, d\theta \, d\phi|^2}. \tag{1.48}$$

For systems with N antennas, we may express the ECC as a matrix $\boldsymbol{P}$ where the ECC between antennas i and j is ρ_{ij}:

$$\boldsymbol{P} = \begin{bmatrix} \rho_{11} & \rho_{12} & \cdots & \rho_{1N} \\ \rho_{21} & \rho_{22} & \cdots & \rho_{2N} \\ \vdots & \vdots & \ddots & \vdots \\ \rho_{N1} & \rho_{N2} & \cdots & \rho_{NN} \end{bmatrix} \tag{1.49}$$

When $i = j$, the diagonal components of $\boldsymbol{P}$ have an ECC of 1. $\boldsymbol{P}$ is also symmetric such that $\rho ij = \rho ji$.

From a physical perspective, reducing the ECC between antenna patterns reduces the probability that a diversity receiver may enter a deep fade. Reducing the ECC between antennas also increases the number of distinct multipaths between transmitter and receiver. This translates into a higher potential for capacity enhancements for a spatial multiplexing system.

In section 1.4, we assumed the only cause for correlation between signals was due to limited multipath reflections between spatial channels in the environment. For embedded MIMO systems, antenna isolation and correlation also impact the capacity and outage probability of the MIMO channel. Consider a two antenna MRC diversity system with correlation ρ

Pattern Diversity

Antenna 1

Antenna 2

Polarization Diversity

Dipole elevation cut pattern

Antenna 1

Dipole elevation cut pattern

Antenna 2

Multipath
reflections

Multipath
reflections

Spatial Diversity
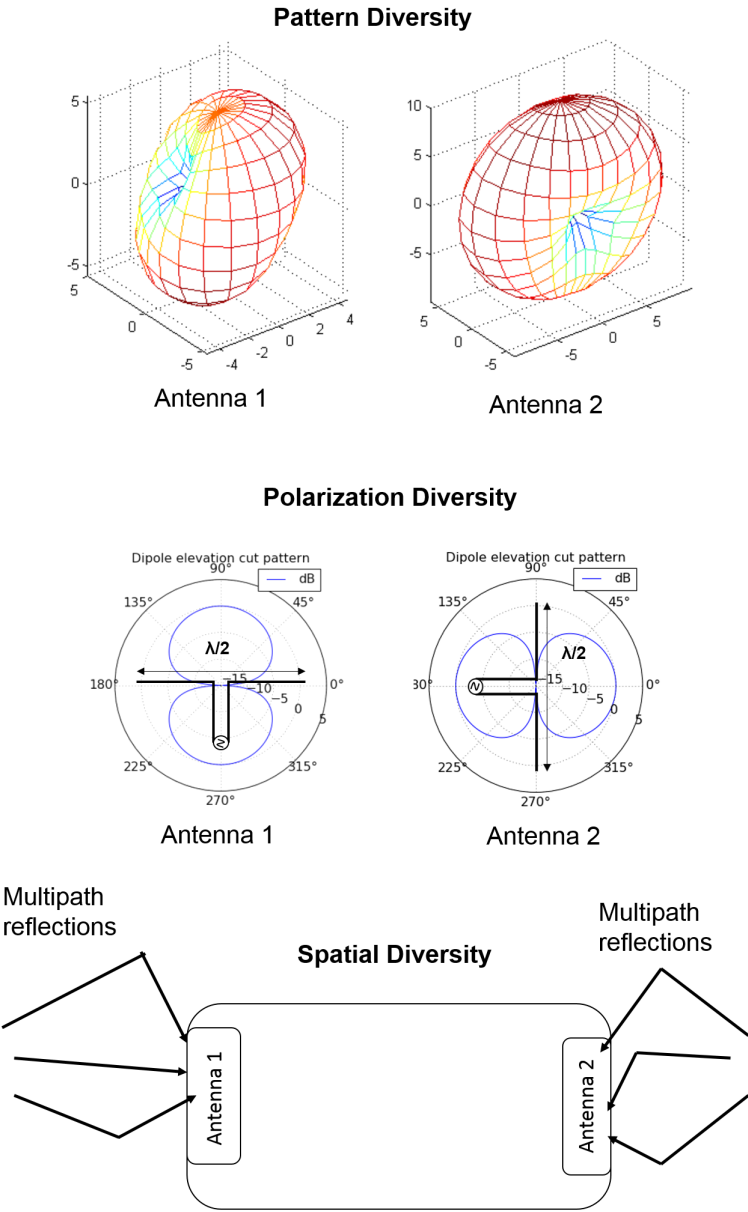
Antenna 1

Antenna 2

Figure 1.13: Types of antenna radiation pattern diversity: pattern diversity showing the rotation of two antenna patterns (top), polarization diversity showing two cross-dipoles for example (middle), spatial diversity showing two offset antenna placements (bottom).
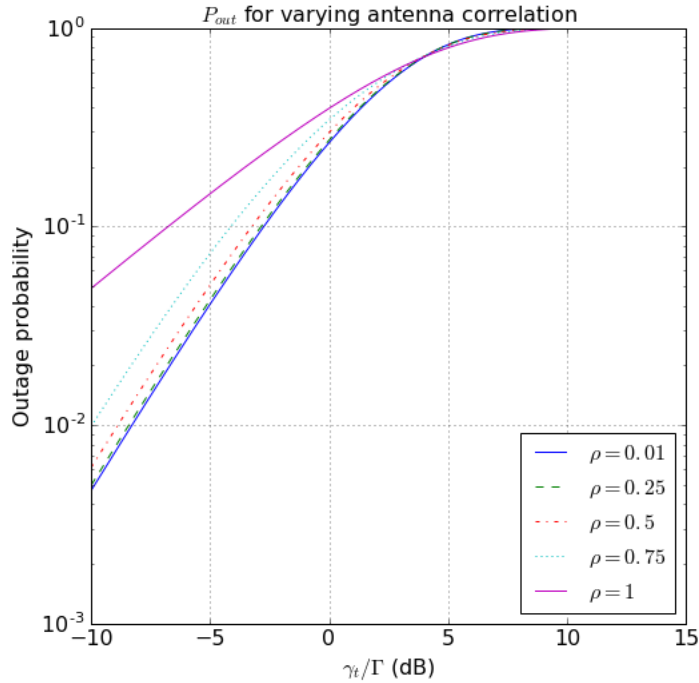
Figure 1.14: Outage probability for a two antenna MRC receive diversity system as a function of ECC between the antennas. The outage probability does not change significantly for ECC below 0.5.

where each element receives a signal that is individually Rayleigh distributed. We can write the probability density function (pdf) of the SNR as [22]:

$$f(\gamma) = \frac{1}{2\rho\Gamma} \left[e^{-\gamma/(1+\rho\Gamma)} - e^{-\gamma/(1-\rho\Gamma)} \right].$$ (1.50)

The outage probability occurs when the SNR falls below γ_t:

$$P_{out} = P(\gamma < \gamma_t) = \int_0^{\gamma_t} f(\gamma) d\gamma$$ (1.51)

which for the Rayleigh faded case reduces to:

$$P_{out} = 1 - \frac{1}{2\rho} \left[(1+\rho)e^{-\gamma/(1+\rho\Gamma)} - (1-\rho)e^{-\gamma/(1-\rho\Gamma)} \right].$$ (1.52)

Figure 1.14 shows the outage probability across correlation coefficient. At a 1% outage probability, there is a significant loss in diversity gain going from perfect correlation to perfect de-correlation. The outage probability does not change significantly for ECC below 0.5.

This analysis suggests that effective MIMO system designers must not only take into account the channel characteristics from the environment, but also the correlation and mutual-coupling between antenna elements. This is especially true for embedded multi-antenna designs, such as mobile handsets. For poorly isolated antenna systems, radiated power may be lost between elements in both transmit and receive. Furthermore, it is desirable to design the antennas in the system to have an ECC less than 0.5 to achieve diversity or spatial multiplexing gains. Such a low correlation may be realized by separating the antennas relative to the wavelength of the communication system. For mobile terminals operating at longer wavelengths, it may not be possible to separate antennas to achieve high isolation and low ECC in a constrained volume.

Chapter 2

Link-Adaptive Antenna Systems

In the previous chapter, we outlined a few well-known methods to enhance the SINR of a communication system in order to improve capacity and reduce outage probability. Antenna diversity and spatial multiplexing exploit the spatial degree of freedom of the wireless channel. However, these multi-antenna techniques do not scale well for practical systems and limited form factors. Multi-antenna systems are only as good as the correlation and isolation between antenna elements. In addition, the radiation patterns of the individual antenna elements themselves may exhibit low-gain regions due to a limited volume and also placement of the antennas near other circuitry within the system. Furthermore, increasing the number of antennas in a MIMO system requires additional complex circuitry, which may be expensive, take up more volume, and consume more power.

In this section, we discuss another method to achieve antenna diversity from a single antenna structure. We present the system architecture for modal adaptive antennas, capable of generating multiple radiating states from a single fed antenna element. In effect, this means that one antenna can act as many antennas, and we can switch between the states of that antenna in time to adapt to the complex propagation channel and provide a peak at the transceivers in the communication system. We begin by discussing modal antenna design techniques and common structures. We then explore the integration of modal antennas with active RF circuitry, such as switches and tunable matching components. We conclude by discussing the system architecture for modal link-adaptive antennas.

2.1   Modal Antenna Structures

Existing implementations of modal antennas primarily consist of a driven or fed antenna element and a switched parasitic array on the ground plane around the driven element. These types of antennas are known as electronically steerable parasitic array radiator (ESPAR) antennas. The radiation states are generated by adjusting the coupling between driven element and parasitic reflector elements, which alter the RF current distribution on the antenna ground plane. As such, the size and distance between the fed and parasitic elements

are the key design parameters. The parasitic elements may be connected to a variable LC circuit to adjust the impedance between the parasitic element and ground. The fed and driven elements may come in different forms: monopoles [49], cross-polarized dipoles [21], or microstrip patches [3] [41], [54].

A variable reactance may be placed between the parasitic elements and the ground plane to change the resonant frequency of the parasitic. Some implementations may use PIN diodes [23] as a low cost means to switch between the parasitics. Other examples use tunable capacitor networks or varactors to control the reactance of the parasitic structures [31]. MEMs switches have also been used for their low RF insertion loss and high isolation between switch ports [40].

Switched parasitic arrays can achieve a low correlation and high degree of antenna diversity from a single driven element. However, the problem with these types of ESPAR antennas is that they require an array of parasitic elements and a large volume, making them unsuitable for embedded mobile applications. Furthermore, ESPAR antennas are often highly directive, and depending on the application, may exceed radiated emissions limits. States of the ESPAR antennas may have high peak gains and correspondingly deep null regions. The low-gain regions of the antenna pose challenges for high reliability systems that must always maintain a communication link. This is a problem because the switched parasitic systems must change between radiation states in time. For example, selection of non-optimal radiating states in a highly dynamic channel could cause a cellular phone to disconnect from a cell tower if the signal experiences a deep null of the channel.

As discussed in the previous chapter, the primary challenges for designing embedded MIMO antenna systems is to realize high efficiency structures with high isolation and low correlation in constrained form factors. In this thesis, we explore the use of isolated loop antenna structures and a single parasitic element to ensure the active antenna volume is practical to fit in an embedded form factor. The antenna structure uses a capacitively loaded inductive loop sitting above the ground plane to tightly confine the current distributions on and around the radiating element (Figure 2.1). This is different from a planar inverted F antenna (PIFA), which primarily uses the capacitive coupling between the ground plane to radiate. Alternatively, the isolated loop structure uses the slot above the ground plane as the primary radiation mechanism, thereby reducing the RF energy transferred to other nearby components, such as shield cans or integrated circuits on the printed circuit board (PCB) [45].

We consider a modal antenna structure that consists of a fed isolated loop antenna element and another parasitic or reflector element placed on the ground plane at some offset (Figure 2.2). In its most basic form, two radiating states of the antenna may be generated by open-circuiting and short-circuiting the parasitic to the antenna ground plane. When the parasitic is open-circuited, the antenna's return loss exhibits a resonant frequency (f_0) due to the main fed element. In the open-circuit case, there is only a small amount of RF current that is induced on the parasitic element from the main element. This induced current flows from the parasitic element back to the ground plane of the antenna. When the parasitic element is short-circuited to the ground plane, the return loss includes a dual resonance
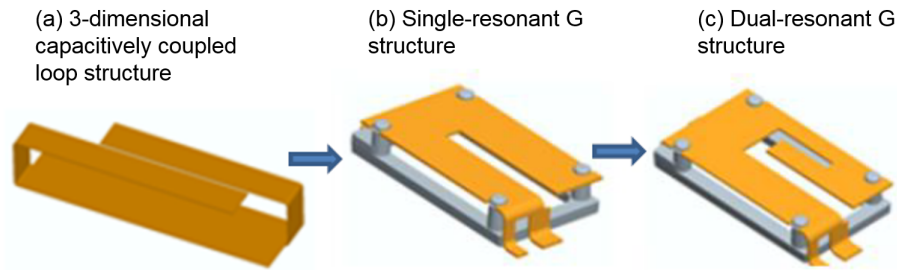
Figure 2.1: (a) 3-dimensional isolated loop antenna structure in which the primary radiation mechanism is between the the two arms sitting above the ground plane. (b) Isolated loop antenna structure with single resonant frequency in the horizontal plane. (c) Isolated loop antenna structure with two resonant frequencies. The lower-frequency resonance is produced from the outer, larger loop and the higher-frequency resonance is produced from the inner, smaller loop.

(f_1 and f_2): one resonance from the main fed element and the other from the parasitic element. Hence, the conductive portion of the RF current flows from the ground plane onto the parasitic reflector. Changing between open and short circuit alters the direction of the RF current distribution on the antenna elements and ground plane, thereby changing the direction of the electromagnetic radiation from the structure. Figure 2.3 illustrates this effect. A variable LC circuit may also be placed between the parasitic and the ground plane to generate more than two radiating states. In this case, a variable reactance may be used to alter the coupling between the main and parasitic elements changing the RF current density vector and resonant frequency of the antenna structure.

We refer to the radiating states of the antenna as modes (not to be confused with transverse electric (TE) or transverse magnetic (TM) modes of a waveguide). We design the modes of the antenna system to have an ECC less than 0.5. We define the correlation bandwidth as the separation between f_0 and f_2. We can tune the correlation bandwidth for different frequency applications by adjusting the parasitic load reactance and by changing the size and separation of the antenna and parasitic elements.

At the same time, each individual mode has a peak directivity that is similar to a passive antenna. Furthermore, the modes exhibit nearly matched total efficiencies. One can visualize the system as adapting how the antenna radiates to match the propagating waves in a cluttered multipath environment, without adding or subtracting from the peak directivity of the antenna. The advantage of this approach is that switching to non-optimal states does not catastrophically impact the communication link, as it may with highly directive antenna systems.
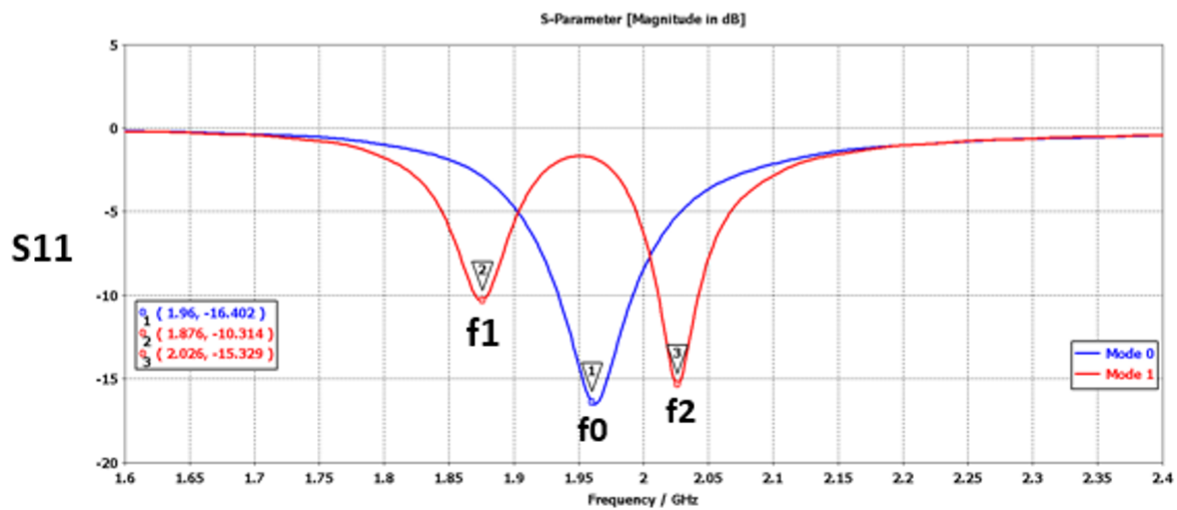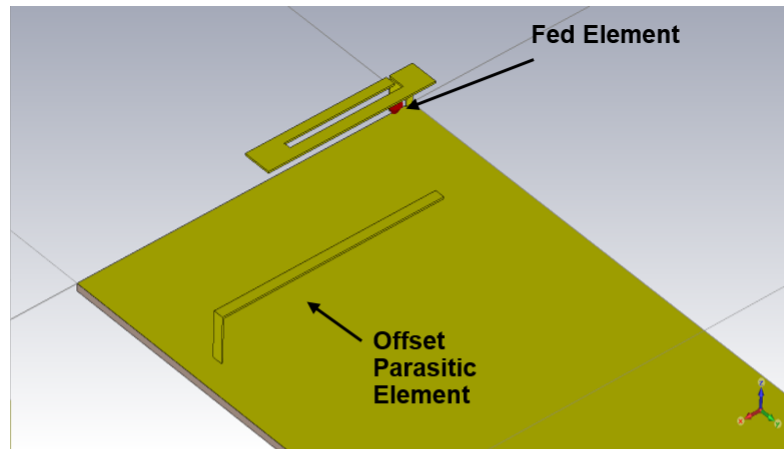
Figure 2.2: Illustration of an isolated loop modal antenna structure. A single resonant frequency f_0 is generated from the driven element when the offset parasitic is open-circuited on the ground plane. Two resonant frequencies f_1 and f_2 are generated when the parasitic element is shorted to the ground plane, thereby becoming part of the overall antenna structure.
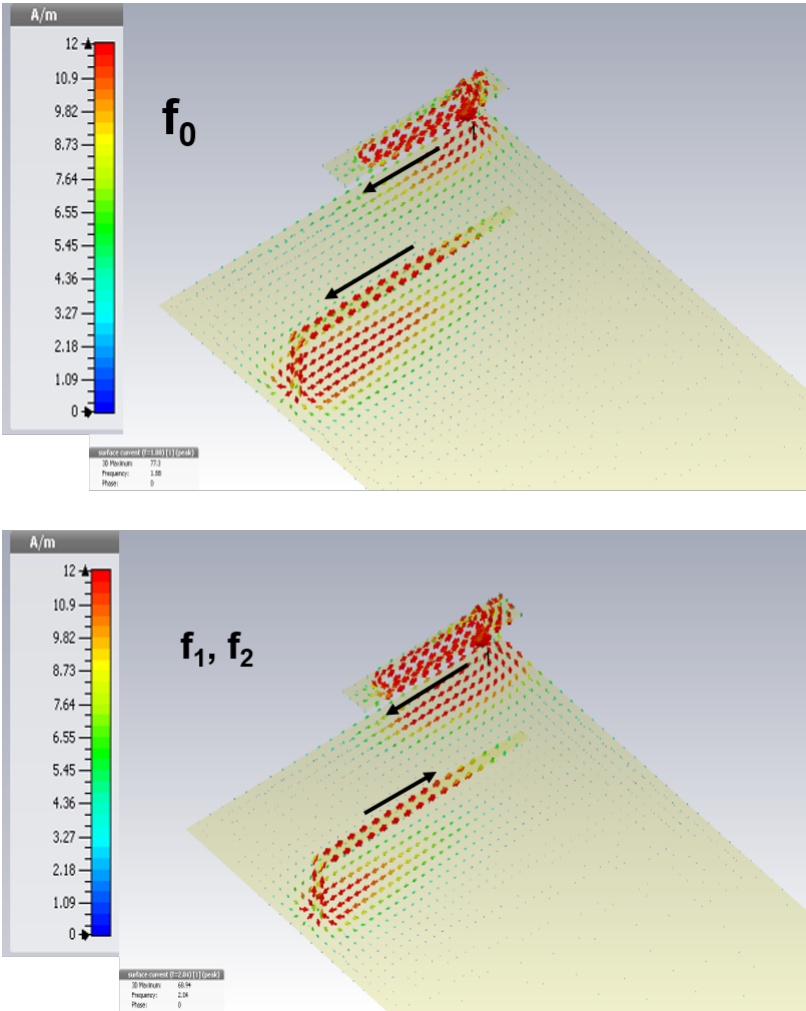
Figure 2.3: Plot of vector surface current density for the modal antenna structure. In the top plot, the parasitic element is open circuit on the ground plane and only an induced current is generated on the parasitic element. In the bottom plot, the parasitic element is shorted to the ground plane. Thus, current flows from the ground plane onto the parasitic, which now acts as a part of the radiating structure.
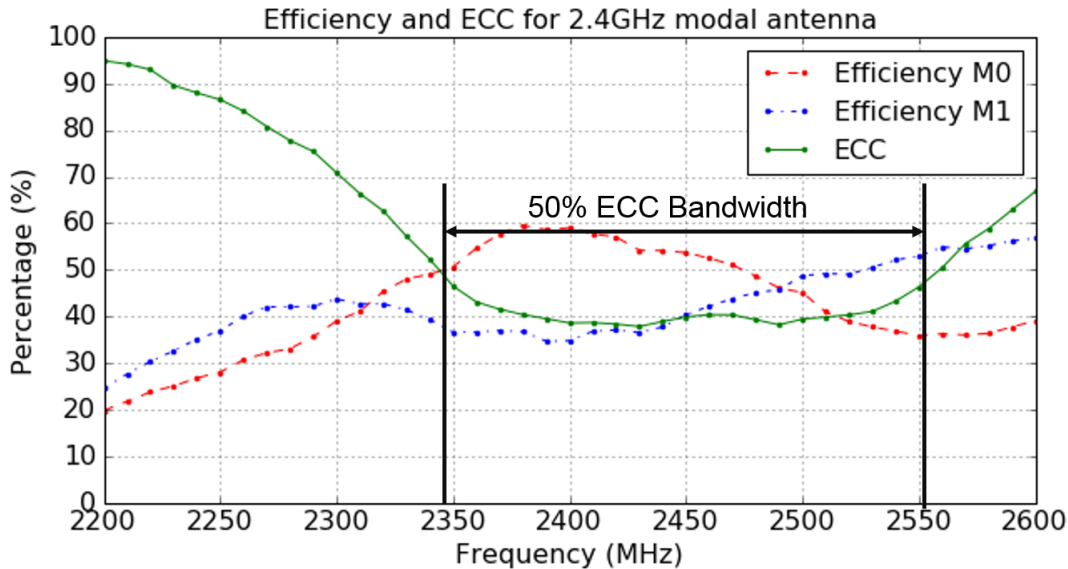
Figure 2.4: Measured efficiency and ECC of two-mode reconfigurable 2.4 GHz antenna with 200 MHz 50% ECC bandwidth. Modes maintain nearly matched efficiency averages across the bandwidth.

2.2   Single Antenna Diversity Gain

Efficiency, ECC, and diversity gain are key metrics to characterize the effectiveness of a modal antenna system. In a MIMO system, maintaining matched efficiencies between antennas in the system means that each antenna contributes equally when averaged over all possible signal directions. For an environment with rich scattering, this increases the likelihood that the channel matrix condition number will be close to 1, and it will be possible to exploit the capacity gains of the channel. Just as with systems with multiple antennas, modal antenna systems must exhibit radiation states with near-matched total efficiency, so that one mode of the system does not severely degrade the communication channel quality when it is selected.

Furthermore, just as with MIMO systems, we can define ECC as a design metric for link-adaptive antennas. For modal antennas, the ECC matrix now represents the correlation between individual radiation states of the same antenna structure. It is not enough to design matched efficiency antennas, the antennas must also be sufficiently de-correlated to achieve diversity gain from a single antenna. MIMO antenna systems rely heavily on spatial diversity to exploit capacity gains. For these kinds of multi-antenna systems, it is advantageous to position the antennas far apart relative to the wavelength and place the antennas orthogonal to each other, so it is less likely that one or more of the antennas experiences the same null of the propagation channel. The challenge for modal antenna systems is that the multiple radiating states are now generated from a single antenna structure so that spatial diversity

cannot be relied upon to lower the ECC. Thus, modal antenna system designers must carefully plan the spacing between the driven and parasitic elements and carefully select the parasitic reactance values to realize an ECC matrix with low correlation.

In addition, we can also define a modal antenna diversity gain factor d from a single antenna structure. Consider a modal antenna system with M radiation modes. We define the maximum gain composite antenna state $G_{max}(\theta, \phi, f)$ by selecting the max gain from all modes over all spherical angles:

$$G_{max}(\theta, \phi, f) = \max_G [G_1(\theta, \phi, f), G_2(\theta, \phi, f), ..., G_M(\theta, \phi, f)] \quad \forall \phi \in [0, 2\pi], \forall \theta \in [0, \pi].$$

$$(2.1)$$

The maximum gain composite state cannot be realized in actual systems, since modal antennas must switch between the individual states in time. However, the maximum gain composite state can be thought of as the effective antenna state of a system that selects the optimal radiation state to always maximize the signal of interest.

Similarly, the minimum gain composite state is defined as an idealized radiation state in which the antenna always selects the mode with the minimum gain across all spherical angles:

$$G_{min}(\theta, \phi, f) = \min_G [G_1(\theta, \phi, f), G_2(\theta, \phi, f), ..., G_M(\theta, \phi, f)] \quad \forall \phi \in [0, 2\pi], \forall \theta \in [0, \pi]. \quad (2.2)$$

The minimum gain composite state may be used to quantify how effective a modal antenna system is at minimizing interference or signals not of interest.

The diversity gain of a modal antenna system is defined as the power gain from using multiple radiation states to achieve a given system outage probability compared to an antenna with a single radiation state. To simplify notation, we express the azimuth angle (ϕ) and elevation angle (θ) in terms of a single variable representing the angle of departure/arrival (Φ) of the signal. If we assume that Φ is a uniformly distributed random variable over all possible antenna orientations and channel conditions, we can express the diversity gain strictly in terms of the radiation states themselves. In other words, we treat the radiation state as the probability density function of the incoming/outgoing signal. Hence, radiation state i has a corresponding cumulative distribution of:

$$F_{\Phi,i} = \int_0^{2\pi} \int_0^{\pi} G_{\Phi,i} \sin \theta \, d\theta \, d\phi. \tag{2.3}$$

If the incoming signal requires an antenna gain of G_0 for error-free detection, we can express the outage probability as:

$$P_{out} = F_{\Phi}(g) = P(g \leq G_0). \tag{2.4}$$

We can use the quantile function, or inverse cdf, to read off the gain at the outage probability P_{out} of interest:
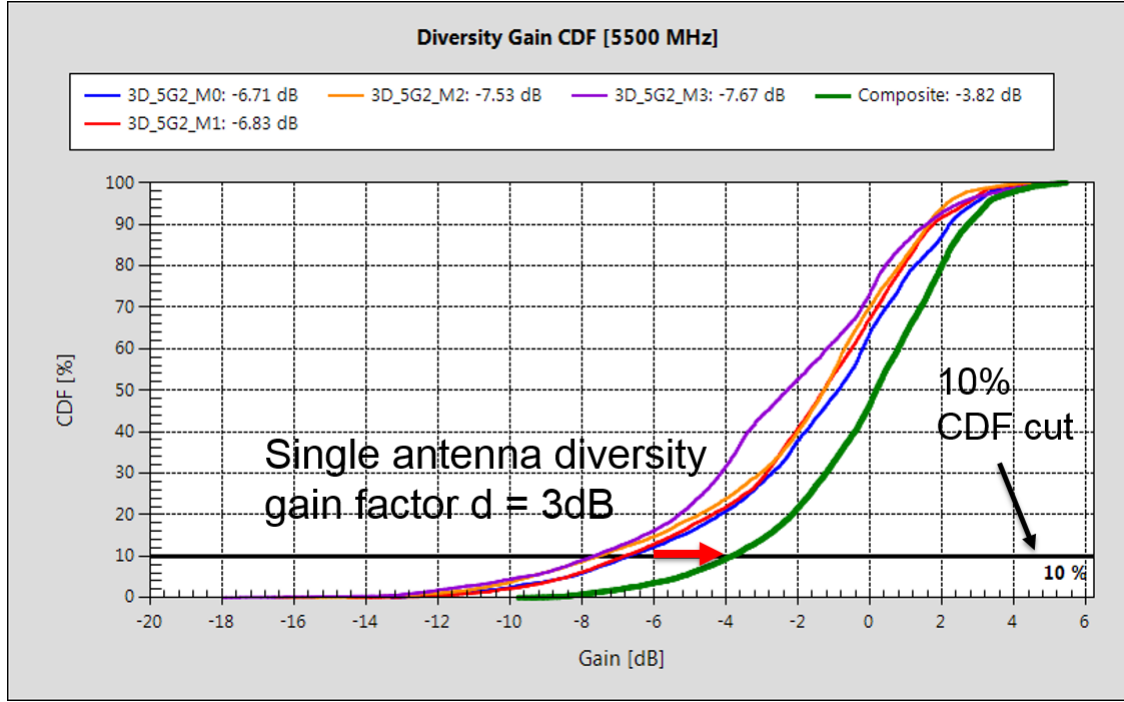
Figure 2.5: CDF of the modal antenna with diversity gain factor d. This plot shows the CDF of the measured radiation patterns of a modal antenna with 4 modes operating at 5500 MHz. The legend shows the gain at the 10% CDF cut for each of the antenna modes. At the 10% CDF cut, the max gain composite state (green curve) has 3 dB higher gain than the highest gain mode (blue curve) of the same antenna.

$$Q_\Phi(P_{out}) = F_\Phi^{-1}(g). \tag{2.5}$$

Thus, the single antenna diversity gain is the power gain difference between the composite state of the modal antenna compared and the ith radiation state at the outage probability. The single antenna diversity maximum gain is:

$$d_{max,i} = Q_{\Phi,max}(P_{out}) - Q_{\Phi,i}(P_{out}). \tag{2.6}$$

Similarly, the minimum gain composite antenna state becomes:

$$d_{min,i} = Q_{\Phi,min}(P_{out}) - Q_{\Phi,i}(P_{out}). \tag{2.7}$$

Figure 2.5 shows an example of a single antenna diversity gain calculation using four radiation states and a 10% CDF cut.

Along with efficiency and the ECC matrix, the diversity gain is a key design parameter for modal antenna systems. Both the radiation patterns and the diversity gain factors are also a function of the frequency of the communication system. Hence, during the antenna

design phase, the single antenna diversity gain factor allows us to quantify how effective the modal antenna system will be based on the application.

We can also use the diversity gain factor to express the capacity improvements expected for SISO and MIMO modal antenna systems (Figure 2.6). We can express the capacity of the SISO channel h is:

$$C = \log_2 \left(1 + |h|^2 SNR\right) \quad bps/Hz. \tag{2.8}$$

If the transmitter sends a fixed rate R bits/s/Hz for a target error probability of P_{out}:

$$P_{out} = P\left[\log_2\left(1 + |h|^2 SNR\right) < R\right]. \tag{2.9}$$

In the usual channel capacity formulation, the transmitter and receiver antenna gains are implicitly included in the channel h. Hence, for a SISO modal antenna system the antenna gain boosts the channel amplitude by a diversity gain power factor d taken at the CDF cut given by the outage probability P_{out}:

$$P_{out} = P\left[\log_2\left(1 + d|h|^2 SNR\right) < R\right]. \tag{2.10}$$

This analysis extends to a MIMO modal antenna system in which one or more of the transmit or receive antennas in the system are modal antennas. We consider the case of a MIMO antenna system with N_{Tx} transmit antennas, N_{Rx} receive antennas, and N_{min} modal antennas on one side of the link. The capacity for the MIMO channel matrix (H) is given by equation (1.43). The outage probability is given in terms of the channel matrix eigenvalues (λ_k), the SNR at antenna k, and the number of antennas. If we assume independent fading between the multipaths, the outage probability is the probability that the channel capacity is less than the sum of the rates of the individual MIMO sub-channels:

$$P_{out} = P\left[\sum_{k=1}^{N_{min}} \log_2\left(1 + \frac{SNR_k}{N_{Tx}}\lambda_k^2\right) < \sum_{k=1}^{N_{min}} R_k\right]. \tag{2.11}$$

The individual eigenvectors of the channel matrix (λ_k) also include the amplitude from the antenna pattern. If antenna k has a modal diversity gain factor of d_k, the outage probability becomes:

$$P_{out} = P\left[\sum_{k=1}^{N_{min}} \log_2\left(1 + d_k\frac{SNR_k}{N_{Tx}}\lambda_k^2\right) < \sum_{k=1}^{N_{min}} R_k\right]. \tag{2.12}$$

Thus, link-adaptive antennas reduce the outage probability of SISO systems by providing diversity from a single antenna structure. For spatial multiplexing systems, adding modal antenna elements improves the link quality and boosts the capacity of the individual MIMO sub-channels. In other words, modal antennas may be used to increase the condition number and rank of the MIMO channel by adapting to SNR mismatches between antennas in the system.
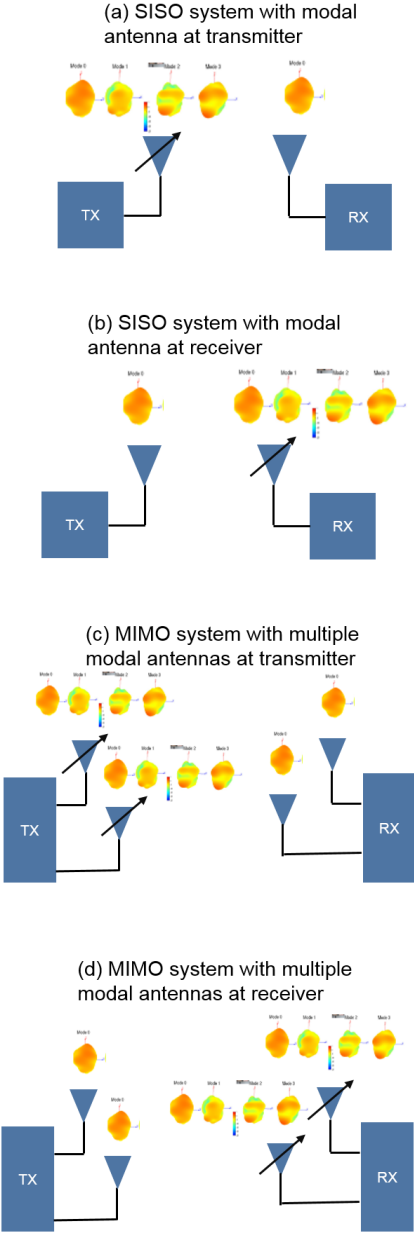
Figure 2.6: (a) Diagram of a SISO system with a modal antenna at the transmitter and passive antenna at the receiver. (b) SISO system with modal antenna at the receiver. (c) MIMO system with multiple modal antennas at the transmitter. (d) MIMO system with multiple modal antennas at the receiver.

2.3 System Architecture

One of the primary goals of this thesis is to bridge experiment and theory and to be able to present measured results of a modal antenna system implemented in a wireless device. Link-adaptive antenna systems consist of three primary components:

1. An antenna structure with a fed element and one or more parasitic elements coupled to the ground plane of the device.

2. A switch or varactor to change between the states of the antenna or to adjust the reactance between the parasitic element and the ground plane.

3. An algorithm to dynamically switch between the states to select the optimal state based on the multipath or interference environment. The algorithm may receive real-time feedback from the transceiver or baseband to make the decision on the best antenna mode.

Figure 2.7 illustrates this system architecture for a SISO system. This core architecture may be extended to MIMO systems as well (Figure 2.8). In this case, one or more of the antennas in the system may be made active. Depending if the MIMO system uses diversity, beamforming, or spatial multiplexing, the algorithm may optimize other metrics than it would with a SISO system. For example, the algorithm may switch between the different states of the antenna to reduce the correlation or increase the isolation between different antennas. This may be especially valuable for size constrained form-factors in which the system wavelength is long relative to the separation between antennas. It is clear that if the system consists of N antennas with M radiation modes per antenna, the number of state combinations is M^N. In subsequent sections, we will explore the effectiveness of this system architecture in terms of actual cellular and indoor wireless field measurements.

2.4 Contributions of This Research

This dissertation explores the concept and experimental validation of modal or link-adaptive antenna systems. We analyze modal antennas in the context of embedded systems, such as cellular phones and WLAN access points, where the antenna volume may be constrained. The goal of this thesis is to present the practical benefits and limitations of modal antenna systems from a communication systems perspective. This research contributes to the state-of-the-art in the following ways:

- Presentation of modal antenna system architecture from antenna design to integration with RF circuitry and algorithms for real-time selection of the radiation states.

- Comprehensive field measurements of link-adaptive antenna systems on live cellular and WLAN networks. Analysis of field data in terms of mobile terminal statistics and the wireless network as a whole.
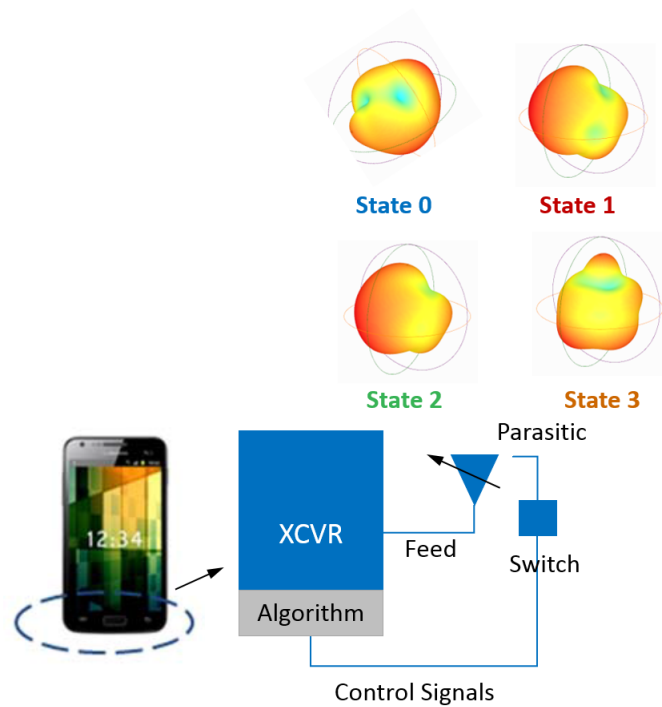
Figure 2.7: System architecture of a modal adaptive antenna system. The system contains a modal antenna structure, a switch, and an algorithm that changes the state of the switch and antenna based on real-time channel state feedback from the transceiver.

- Presentation of the modal antenna state prediction process in terms of measured channel fading and coherence time.

- Application of modal antennas with form factors small enough to fit in the size of a cellular phone.

- Extension of modal antenna architectures to include MIMO systems: spatial multiplexing and beamforming.

- Treatment of link-adaptive antennas as a full system in terms of typically disparate research areas, such as antenna design, signal processing, radio wave propagation, and software design.
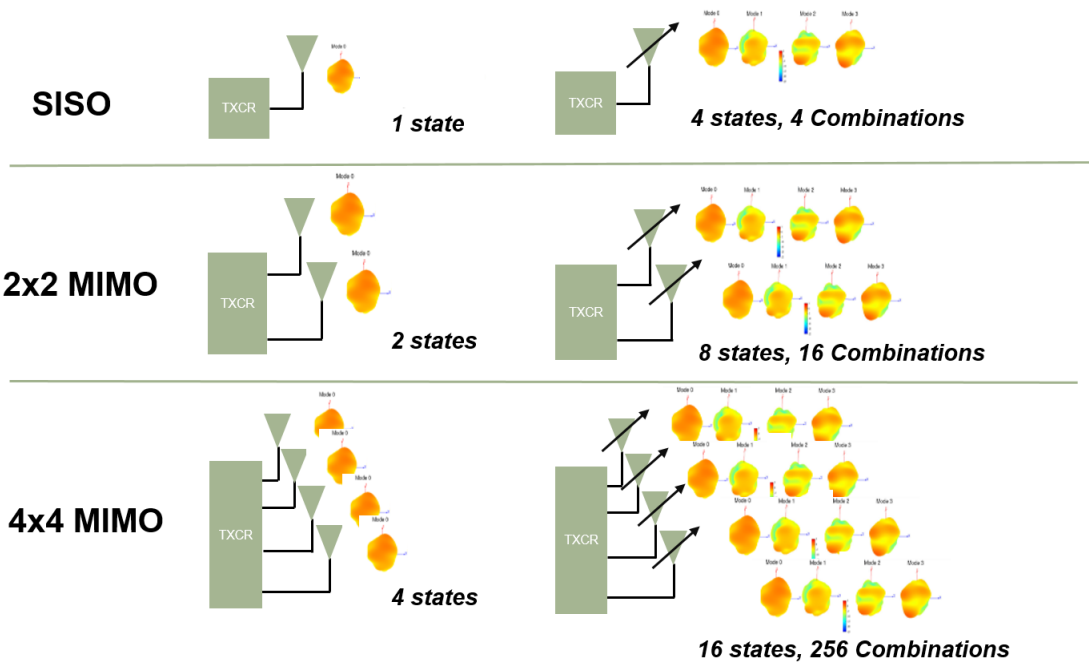
Figure 2.8: SISO and MIMO systems with passive antennas (left). SISO and MIMO systems with link-adaptive antennas (right). The example shows how the number of radiating states and state combinations scale for a system with four radiating modes at each antenna.

Chapter 3

The State Prediction Process

Next we discuss the state prediction process of the modal antenna system. Because multiple radiation states are generated from the same antenna structure, a process is required to switch between the individual states in order to choose the best mode based on the RF environment. The prediction process uses one or more channel quality indicators (CQIs), such as SINR or block-error-rate (BLER), from the radio or baseband to inform how well the current antenna state is performing. The goal of the process is to pick the state of the antenna that maximizes the CQI.

The two primary challenges for the modal antenna state prediction process are:

1. How to select the best antenna state to adapt to the fading environment, when only one state may be selected at a time?

2. How frequently to sample the channel to select the best radiation state for slow- and fast-fading channels?

We will explore the tradeoffs for the first item in sections 3.1 and 3.2, and we will present empirical results for the second question in section 3.3.

3.1   The Applied Multi-Armed Bandit Problem

We frame the state prediction process in terms of the familiar reinforcement learning multi-armed bandit problem [44]. In its simplest form, the multi-armed bandit problem consists of a gambler who pulls the arms of a slot machine to receive an award. The reward on each arm has an associated statistical distribution, and the gamblers goal is to maximize the expected value of the reward. At first the gambler has no knowledge of the rewards for each arm, and he must gather information on the distributions by testing the different arms. After testing each arm, the gambler can then focus on the most rewarding levers. We refer to the training process to acquire knowledge about the distributions as the exploration

phase. Once the gambler has explored the arms, he may exploit the game by selecting the arms that provide the highest reward.

Clearly there is a tradeoff between exploration and exploitation. It is well known that the solution to the multi-armed bandit problem depends on the number of arms, the number of turns, and the reward variance of each of the arms [28]. Several solutions to the problem have been proposed, and it has been found that simpler, approximate solutions may outperform more complex solutions in practice [63]. One such approximate solution is the ϵ-greedy strategy [66]. In this approach, the gambler selects the best lever with proportion $1 - \epsilon$, except when training. During exploration, the gambler uniformly selects one of the other slot machines with a proportion ϵ. For example, the proportion ϵ may be chosen to train the other slot machine arms 10% of the time and to select the best arm 90% of the time.

More exploration is required to track slot machine reward distributions with higher variance. Given this heuristic, another strategy is to adapt the resampling rate ϵ to track the probability distributions of the slot machines. The probability matching Bayesian bandit is an example of an ϵ-greedy strategy in which the number of pulls of a lever matches its probability distribution. In other words, levers that are more likely to be optimal are pulled more often.

The process of selecting the best state of the antenna is an example of a multi-armed bandit problem. In this chapter, we will present an applied version of the multi-armed bandit problem. Our purpose is not necessarily to find an optimal solution to the general problem, but rather to present an algorithm that works well in practice for link-adaptive modal antenna systems. For this application, the prediction process must train the different states with some proportion to determine which state will provide the highest CQI. The distribution of the wireless fading channel and angle of arrival of signals describes the probability that a given state will be optimal. These distributions may vary with time, in which case the proportion of training may be chosen to match the coherence time of the channel. Fast fading channels require re-training more often. That is, a key parameter to the state prediction process is how quickly the baseband processor can acquire a CQI value and present it to the algorithm. We explore this limitation in subsequent sections.

3.2   The NLMS Filter

The state prediction process must be able to dynamically adapt to channel variations for each of the modes of the antenna system. That is, the rate of change of the signal quality may be just as important as the instantaneous value of the signal quality. One such example, may be a cellular phone where the user is moving at a fast speed and the channel is changing rapidly relative to the channel measurement sample time. Stochastic gradient descent filters, such as normalized least means square (NLMS) filters, perform well for such problems [68].

The NLMS algorithm is not overly computationally intensive to implement in hardware or software. As such, NLMS filters have found numerous applications in smart antenna systems [69] [33], such as beamforming arrays [19], [58], radar [9], and for noise and interference
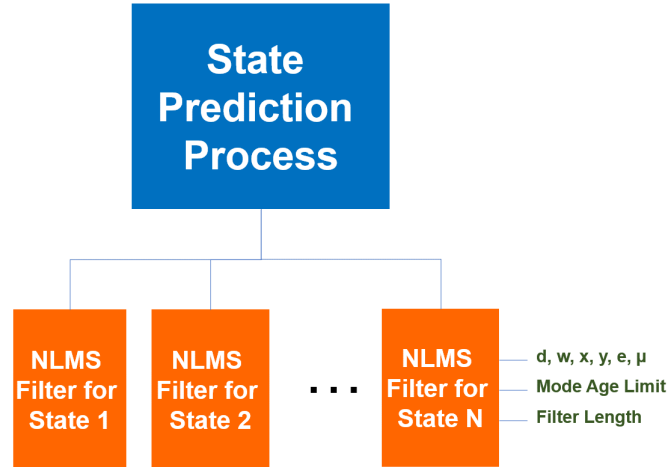
Figure 3.1: Modal antenna state prediction process in which the CQI of each mode of the modal antenna system is predicted using an NLMS filter.

cancellation [70] [26]. NLMS filters may also be applied to modal antennas; however, it should be noted that the NLMS algorithm may not be optimal for a modal antenna system across all fading channels. The development of other modal antenna prediction algorithms and proof of optimality is an interesting area for further exploration that is beyond the scope of this work. Instead, our intent is to provide the reader with an algorithm that works well for antennas with multiple radiation states and across practical wireless fading channels.

In the context of modal antenna systems, the NLMS algorithm uses a linear CQI predictor to estimate what the CQI of a mode will be based on past signal quality information for that mode. The algorithm must switch between the antenna states at different time intervals. It is important to note that the algorithm does not know the signal quality for a given mode until it selects that mode.

Consider a modal antenna with M states. We assign an LMS filter to each mode m to track its distribution of signal quality at each time interval (Figure 3.1).

Filter weights are applied to the previous CQI sample inputs such that the mean squared error (MSE) of the output is minimized. The vector weights $\mathbf{w}_m(n)$ are given by:

$$\mathbf{w}_m(n) = [w_1(n), w_2(n), ..., w_L(n)]^T \tag{3.1}$$

where $(.)^T$ represents the transpose operator and L is the filter length. The CQI input values $(\mathbf{x}(n))$ are:

$$\mathbf{x}_m(n) = [CQI(n-1), CQI(n-2), ..., CQI(n-L)]^T \tag{3.2}$$

The NLMS weight calculation that minimizes the MSE at time $n+1$ in the future is:

$$\mathbf{w}_m(n+1) = \mathbf{w}_m(n) + \mu \frac{\mathbf{x}_m(n)e_m(n)}{\mathbf{x}_m(n)\mathbf{x}_m^H(n)} \tag{3.3}$$

in which μ is the step size, $e_m(n)$ is the filter prediction error and $(.)^H$ is the Hermitian transpose. The estimation error is given in terms of the current input $d_m(n)$:

$$e_m(n) = d_m(n) - \mathbf{x}_m(n)\mathbf{w}_m^H(n). \tag{3.4}$$

In other words, the errors are used as feedback to adjust the tap weights. The predicted future value $\widetilde{CQI}_m(n+1)$ for mode m is:

$$\widetilde{CQI}_m(n+1) = \mathbf{x}_m(n+1)\mathbf{w}_m^H(n+1). \tag{3.5}$$

Since we will be using the gradient of the CQI signal to select the optimal radiation mode, we can remove the DC portion from the input:

$$\overline{d}_m(n) = \frac{1}{L} \sum_{n=1}^{L} \widetilde{d}_m(n). \tag{3.6}$$

Figure 3.2 outlines the steps of the NLMS state prediction process.

The state prediction algorithm may only select one filter output or mode at any given time, and thus, the algorithm must handle two different phases of operation.

- Learning phase: at time index n, the desired output $\mathbf{d}_m(n)$ is known, and the algorithm must predict the output $\mathbf{y}_m(n+1)$ at the next time step.

- Blind phase: at time index n, the desired output $\mathbf{d}_m(n)$ is not known and we need to predict the output $\mathbf{y}_m(n+1)$ at the next time step. This phase occurs for filters whose mode was not selected by the algorithm.

Below is a summary for computing the NLMS filter output.

1. Determine which sample input $\widetilde{d}_m(n)$ to use:

   a) Learning phase: $\widetilde{d}_m(n) = d_m(n)$
   b) Blind phase: $\widetilde{d}_m(n) = y_m(n)$

2. Calculate the CQI input by removing the DC offset from the input:

   a) $\overline{d}_m(n) = \frac{1}{L} \sum_{n=1}^{L} \widetilde{d}_m(n)$

Error Estimation:

$e(n) = d(n) - y(n)$

Filtering:

$\widetilde{CQI}(n + 1) = w^T(n + 1)x(n)$
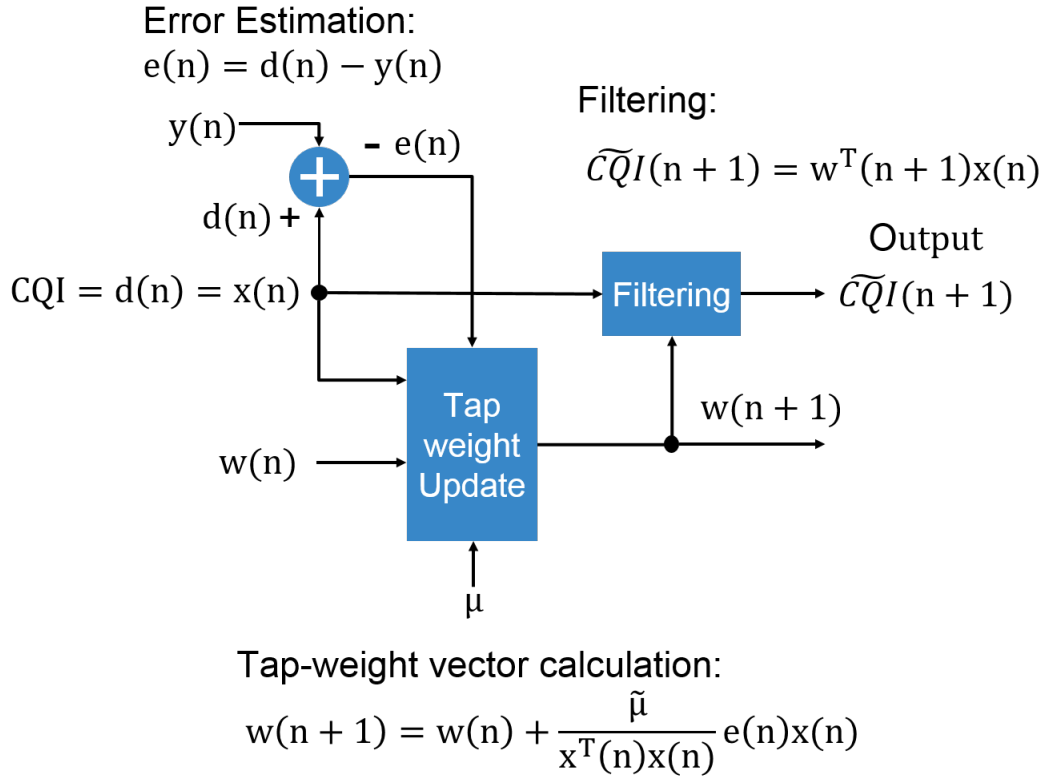
Figure 3.2: NLMS algorithm block diagram, illustrating error estimation, normalized tap-weight vector calculation, and filtering to generate the predicted CQI.

b) $x_m(n) = \widetilde{d}_m(n) - \bar{d}_m(n)$

3. Error estimation: $e_m(n) = x_m(n) - y_m(n)$

4. Tap-weight vector adaptation: $\mathbf{w}_m(n + 1) = \mathbf{w}_m(n) + \mu \frac{\mathbf{x}_m(n)\mathbf{e}_m(n)}{\mathbf{x}_m(n)\mathbf{x}_m^H(n)}$

5. Filtering: $\widetilde{y}_m(n + 1) = \mathbf{x}_m(n + 1)\mathbf{w}_m^H(n + 1)$

6. Calculate predicted output at time $(n + 1)$: $\widetilde{CQI}_m(n + 1) = \mathbf{y}_m(n + 1) + \bar{d}_m(n)$.

7. Repeat for all antenna modes m and select the mode at time step n based on some ϵ-greedy strategy.

3.3 State Prediction Parameters

Next, we consider the problem of how to select from the possible modes using an ϵ-greedy strategy. Given the NLMS formulation, we empirically determine values for the step size μ,

Table 3.1: Percentage of time spent learning relative to the age limit for a system with four NLMS filters.

Age Limit	% of Time Spent Learning
4	75%
8	37.5%
12	25%
16	18.8%
32	9.4%
64	4.7%
128	2.3%
256	1.2%
512	0.6%

re-train limits, and filter lengths L_m based on knowledge about the variance of the fading channels for each mode.

In order to account for the re-training intervals, we introduce an age limit variable, A_m, for each of the filters. At each time step n, if the mode of the associated filter was not selected, we increment its age. If the filter was selected, we set its age to zero. Once the age of a filter reaches the age limit, the algorithm must select that mode, even if it is not optimal at the time. The age limit for each of the filters may be fixed, based on some ϵ-greedy strategy and knowledge of the dynamics of the fading channel. For instance, in order to achieve a exploration rate of e for an antenna with M antenna states, we would select the fixed age limit A for each mode such that:

$$A = \frac{M - 1}{e}. \tag{3.7}$$

Table 3.3 shows the percentage of time spent learning as a function of the age limit for a system with four NLMS filters.

The step size μ determines how heavily the weights change based on the gradient estimate. It is critical to select μ such that the NLMS filter is stable. The step size stability condition at time n is [55]:

$$0 < E\left[\mu(n)\right] < \frac{2}{\lambda_{max}} \tag{3.8}$$

where λ_{max} is the greatest eigenvalue of the input signal autocorrelation matrix $\mathbf{R_x}$:

$$\mathbf{R_x} = E\left[\mathbf{x}(n)\mathbf{x}^H(n)\right]. \tag{3.9}$$

On the other hand, if μ is chosen to be too small, the NLMS filter will minimally account for the gradient of the signal. This may be acceptable for signals that vary slowly relative to the filter length, but will decrease the prediction accuracy in fast fading scenarios. The optimal convergence speed is given by [1]:

$$\mu_{opt} = \frac{2}{\lambda_{min} + \lambda_{max}}. \tag{3.10}$$

The filter length determines the number of samples that the NLMS filter uses to make the weight calculation. A longer filter length uses more of the previous samples to calculate the CQI output. If the samples from the fading channel are changing rapidly, the filter length should be made short. If the samples from the channel are changing slowly, the gradient of the signal will be small, and making the filter length short has minimal effect on the prediction error.

We consider the filter error parameters suitable for a modal antenna algorithm based on empirical channel measurements. The channel measurements were taken on an LTE cellular network using a handset moving at three different speeds: 0 km/h, 6 km/h, and 40 km/h. We recorded 5000 channel SINR samples every 10 ms for the study. The experimental setup is described in Chapter 4. Figure 3.3 shows a snapshot of the SINR measurements for 1000 samples.

We evaluate the prediction performance in terms of the root-mean-squared-error (RMSE) of the NLMS filter:

$$RMSE = \sqrt{\frac{1}{N} \sum_{n=1}^{N} (y(n) - d(n))^2}. \tag{3.11}$$

In the study, we use an NLMS filter with a filter length of 8. We find that this provides a good compromise between computing the gradient given the past inputs without considering too many of the older samples for faster varying channels. Figure 3.4 shows the results of the study as a function of user speed.

The LMS filter becomes unstable for step sizes that overfit the channel. Smaller age limits indicate more learning phases. If the measured channel samples have a large variance, the LMS filter weights become unstable, leading to large increases in the RMSE. Larger age limits indicate more blind phases, in which the filter must estimate the channel without receiving a measured sample. Hence, larger age limits can tolerate larger mu values before becoming unstable. As expected, for walking and driving channels, in which the gradient of the signal varies significantly, the LMS algorithm reduces the RMSE of the predicted signal compared to a simple moving average. On the other hand, when μ equals zero, the gradient of the signal is not included in the NLMS predicted output, and this provides the best performance for larger age limits and static channels.

Clearly the prediction performance decreases for higher speeds and this is a limitation of the sample update rate. As the user moves through the environment, the incoming wave may pass through different peaks and nulls of the channel. To first order, the number of samples to accurately model the channel depends on the number of quarter-wavelengths the user is moving at any given time. We can specify a nominal time for a selection algorithm to sample the channel accurately as a function of the user speed v_{UE} and wavelength λ:
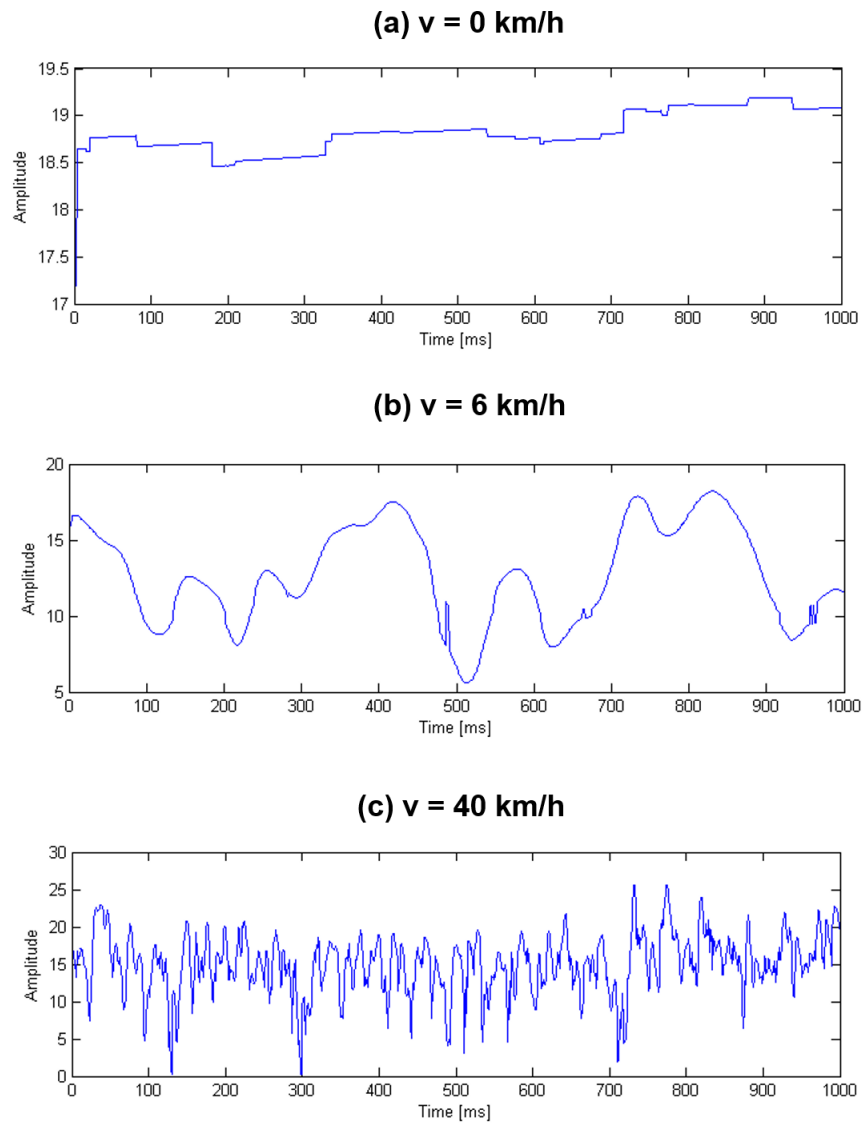
Figure 3.3: Snapshot of 1000 samples of SINR as measured using a cellular phone on a live LTE network. Three channels were used for empirical evaluation of the NLMS filter age limit and step size parameters. Channel measurement cases: (a) stationary v = 0 km/h, (b) walking channel v = 6 km/h, (c) driving channel v = 40 km/h.
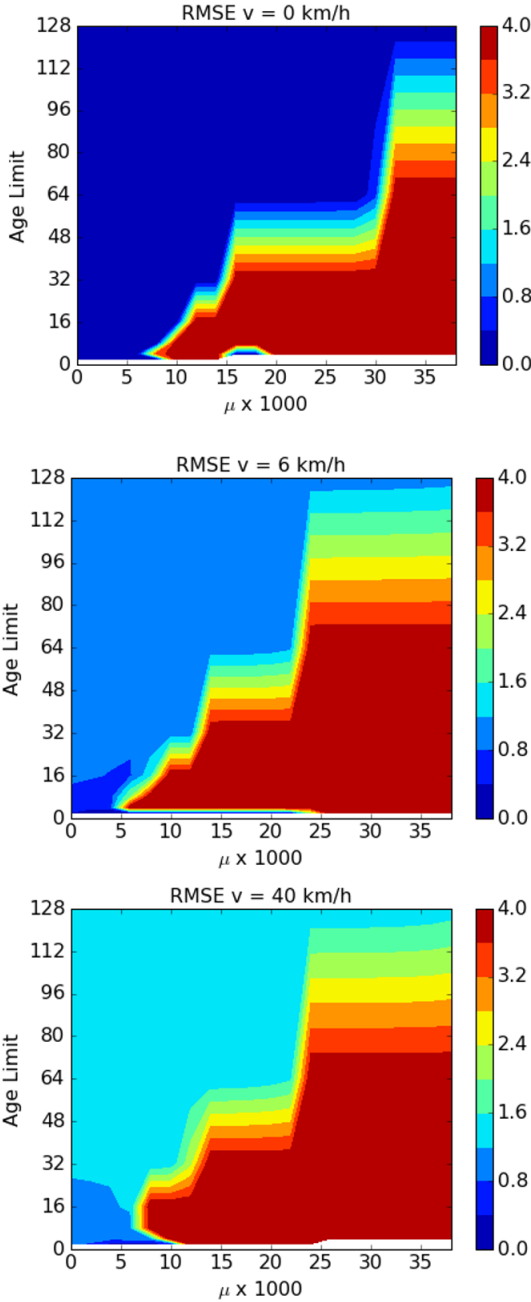
Figure 3.4: Plot of LMS filter RMS error as a function of step size, μ, and filter age limit for static (top), walking (middle), and driving (bottom) fading channels sampled at 10 ms intervals.
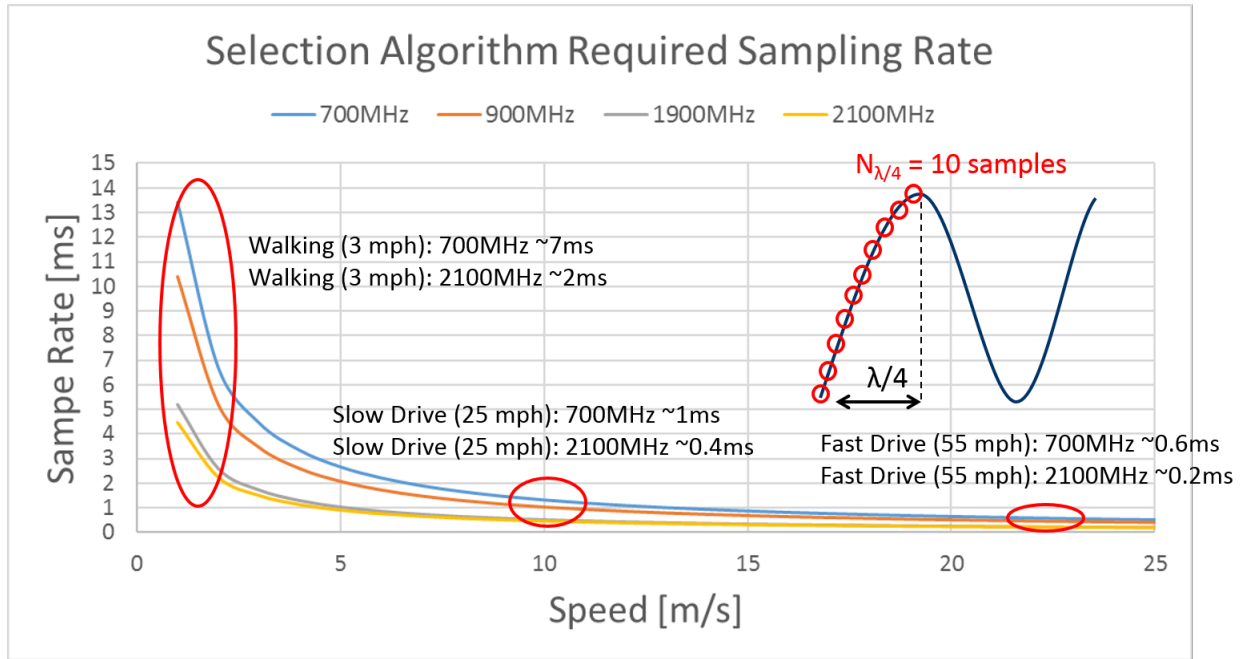
Figure 3.5: Sampling time for common cellular frequencies based on equation (3.12) for N = 10 samples per quarter wavelength.

$$T = \frac{\lambda/4}{v_{UE} N_{\lambda/4}} \tag{3.12}$$

Figure 3.5 plots the required sample time to achieve ten samples per quarter wavelength as a function of user speed for common cellular frequencies. Modern LTE baseband processors compute the cellular tower pilot signal at subframe intervals of 1 ms [5], so it is reasonable to expect that we can sample the channel accurately for walking and slow driving speeds. However, to accurately sample at highway driving speeds, requires sub-millisecond update intervals, which may not be feasible for some communication systems.

Chapter 4

Applications for Cellular Networks

One of the primary goals of this thesis is to explore the practical effects of modal adaptive antennas in an actual wireless communication system. In order to evaluate this, we design a cellular field trial on a live 4G LTE network. The experimental design and measured capacity results are the topic of this chapter. We retrofit a cellular handset with a modal adaptive antenna system from the ground up, including the antenna design, the state prediction algorithm, and the associated software to log key performance indicators (KPIs) across time and location for both the handset and the network.

Field measurements are typically avoided in communication systems research due to the sheer time required to collect the data and ensure repeatability. In this chapter, we not only discuss the field performance of modal antennas, but we also focus on the design of the field measurement itself. As with any statistical trial, the key is to collect data in several different propagation environments over many different times of day. Moreover, the measured channel models from this research may be used to better inform the statistical models used by communication theorists.

4.1 LTE Physical Layer Parameters

The 3rd Generation Partnership Project (3GPP) LTE standard has enjoyed a significant amount of success since its deployment in 2010 thanks to its rapid market adoption, efficient use of spectrum in multi-user sites, and robustness to multipath fading [53] [11]. To account for spectrum fragmentation among network operators, LTE allows for scalable bandwidth deployments of 1.25, 2.5, 5.0, 10.0, and 20.0 MHz. LTE uses OFDMA as the primary air interface mechanism to allow data to be scheduled to multiple users in frequency intervals as small as 180 kHz and time slots of 0.5 ms. This minimum scheduling datum is known as a resource block.

LTE also allows for adaptive modulation and coding (AMC) as users in different regions of the cell will experience different channel conditions. AMC is implemented as a feedback mechanism whereby the user equipment (UE) sends a requested modulation and coding

Table 4.1: MCS and spectral efficiency mapping used in LTE AMC.

CQI	SINR (dB)	Modulation	Code Rate	Spectral Efficiency (bps/Hz)
1	-3.1	QPSK	0.08	0.15
2	-1.2	QPSK	0.12	0.23
3	1.5	QPSK	0.19	0.38
4	4.0	QPSK	0.30	0.60
5	6.0	QPSK	0.44	0.88
6	8.9	QPSK	0.59	1.18
7	12.7	16QAM	0.37	1.48
8	14.9	16QAM	0.48	1.91
9	17.5	16QAM	0.60	2.40
10	20.5	64QAM	0.46	2.73
11	22.5	64QAM	0.55	3.32
12	23.2	64QAM	0.65	3.90
13	24.9	64QAM	0.75	4.52
14	27.0	64QAM	0.85	5.12
15	29.1	64QAM	0.93	5.55

scheme (MCS) to the basestation or eNodeB (eNB) to send on the next transmission. The LTE standard maps the MCS indices as a 4-bit CQI value. This CQI is not to be confused with the modal antenna CQI, which we refer to as a generic channel quality parameter for a state prediction process. Table 4.1 shows these CQI values and their associated spectral efficiencies [24].

The SINR values in this table are based on simulations for a flat Rayleigh faded channel. Each CQI step corresponds to an SINR increase of 1.5-3 dB. That is, if we can improve the signal quality by adapting the antenna to the propagating wave, the associated diversity gain can allow the modem to operate at a more spectrally efficiency modulation and coding scheme. This translates into improved reliability and fewer network resources consumed by the cellular handset.

Figure 4.1 plots the SINR and spectral efficiency for one CQI increase. We observe a larger percentage increase in spectral efficiency for lower CQI values. In other words, improving the link margin has a more significant effect for lower signal qualities, which occur for cases when the UE is closer to the cell edge. This is because for QAM modulation techniques the spectral efficiency scales as the logarithm of the number of constellation points. Higher order QAM modulation schemes increase the absolute value of the spectral efficiency, but only in high SINR regions near the cell tower where the link margin is already good.

At the physical layer, we will use the following KPIs for evaluation of the modal antenna system: RSSI, RSRP, RSRQ, and SINR.

- RSRP: reference signal received power is defined as the average of the resource elements that carry cell-specific pilot signals [16]. RSRP measures the signal power from a
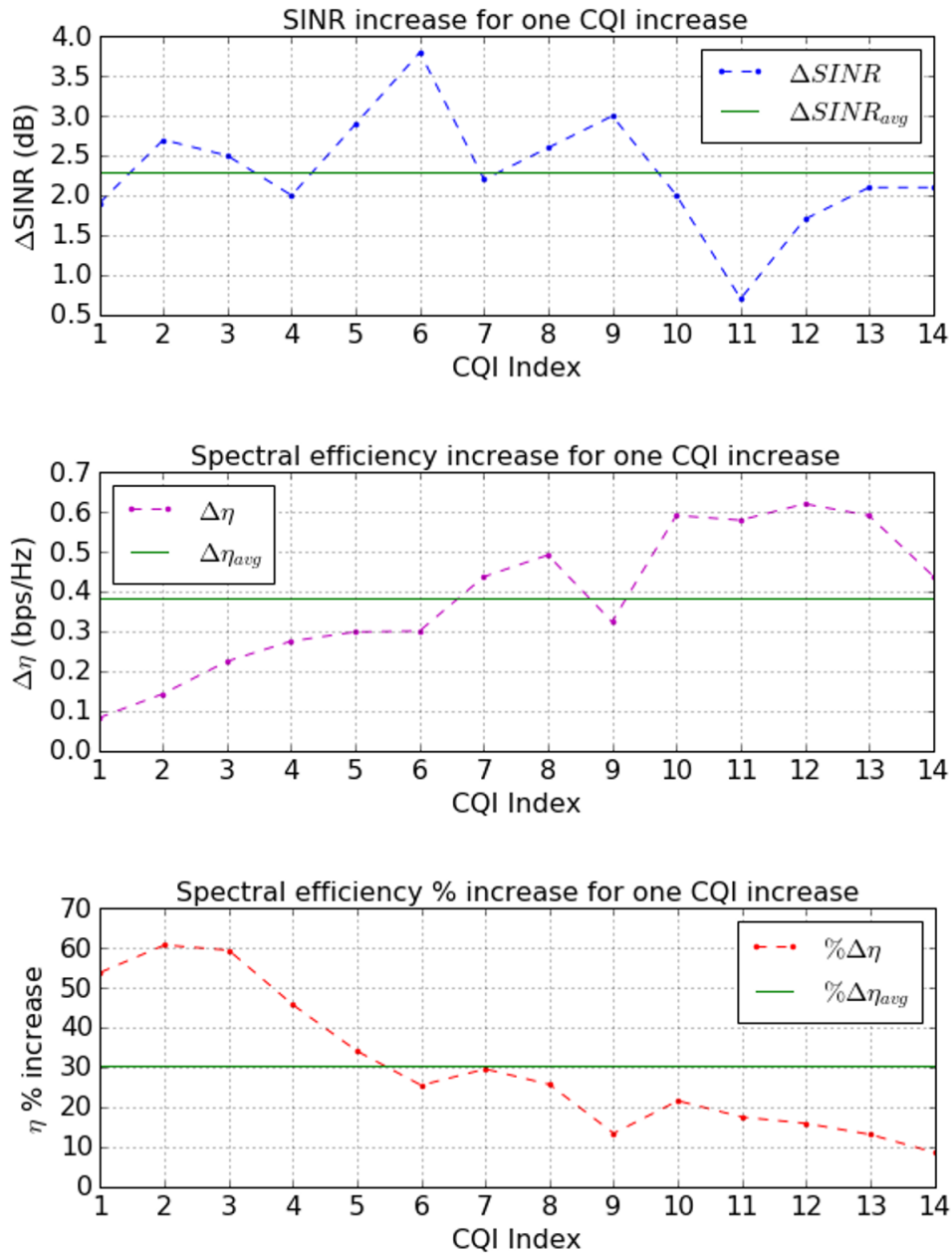
Figure 4.1: Plots of SINR (top), spectral efficiency (middle), and percentage increase in spectral efficiency (bottom) for one step increase in CQI index. For all possible LTE channel conditions, we would expect that a 2.3 dB increase in SINR would translate into a 30% increase in spectral efficiency on average.

specific cell sector.

- RSSI: receive signal strength indicator is the wideband power across all reference signal symbols [16]. RSSI includes noise power, serving cell power, and interference power.

- RSRQ: reference signal received quality is the ratio of RSRP to RSSI over the number of resource blocks for which RSSI is measured [16]. $RSRQ = N_{RB} \times \frac{RSRP}{RSSI}$.

- SINR: signal to interference plus noise is defined as the ratio of the average received signal carrier power to the sum of the noise power and interference power from other sources or neighboring cells. SINR is measured by the baseband receiver after down-conversion from RF. While SINR is not standardized by the 3GPP, our measurements indicate that it provides the best correlation with CQI and spectral efficiency on the measured handset.

Furthermore, we evaluate throughput and spectral efficiency as key indicators of network performance. We compute the spectral efficiency using the measured throughput, error rate ϵ, and number of resource blocks consumed by the handset over a time interval:

$$\eta_{UE} = \frac{\text{Throughput} \times (1 - \epsilon)}{N_{RB} \times 180\text{kHz}}. \tag{4.1}$$

In this thesis, when we use the term throughput, it is implied to mean goodput: the throughput after block errors have been discarded.

4.2   Implementation of a Modal Antenna System in a Handset

We select a 4G LTE handset in mass production to retrofit with a modal antenna system for our experiments. The device has two cellular antennas with an LTE category 4 modem. For feasibility of the retrofit, we only modify the main cellular antenna at the bottom of the phone, and the diversity antenna is left unmodified (Figure 4.2). The main fed element of the antenna and offset parasitic element sit on a plastic carrier above the main logic board. We retrofit a single-pole four throw (SP4T) RF switch on the main logic board and connect the common port to the parasitic element of the antenna. The control lines of the RF switch are routed to the status LED of the phone so that they can be controlled by the applications processor.

The antenna is designed to operate on LTE AWS band 4 (downlink 2110-2155 MHz and uplink 1710-1755 MHz) and LTE band 7 (downlink 2620-2690 MHz and uplink 2500-2570 MHz) with three radiation modes. We limit the multiple radiation modes to the downlink band only because the chosen LTE networks for the field trials are frequency division duplexed (FDD). The state prediction process uses channel state information receive (CSIR) from the baseband of the phone, and the channel state information transmit (CSIT)
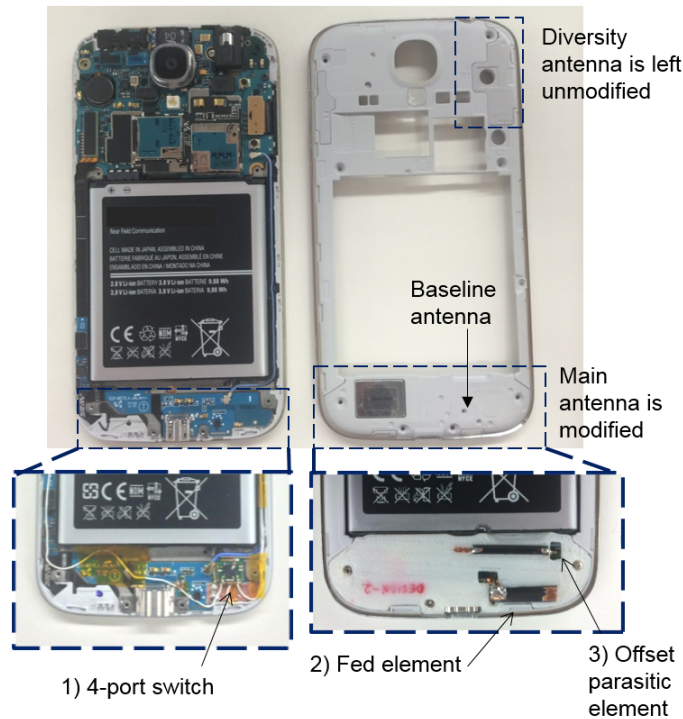
Figure 4.2: Cellular phone retrofit with active reconfigurable antenna system with SP4T, driven antenna element, and offset parasitic element. The main antenna is modified and the diversity antenna is left passive. We wire the GPIOs from the activity LED in order to control the four-port switch from the applications processor.

is not computed by the baseband for the FD-LTE uplink. Because the uplink and downlink frequencies are separate, their wireless channels will fade differently. It is worth noting that for time division duplex (TDD) LTE systems, the wireless uplink and downlink channels will be reciprocal. Hence, the CSIR may be used for the state prediction process to adapt the antenna to the uplink propagation channel as well. The effect of channel reciprocity on transmit and receive is explored in the next chapter for indoor wireless LAN systems, and it is left as an area for further study for cellular active antenna systems.

The single antenna diversity gain and ECC in the two test bands are shown in Figure 4.3 below. We are able to achieve a single antenna diversity gain between 1.5-2.5 dB with ECC between 35-70% across both bands using this three mode retrofit antenna system. Optimizing the volume for this antenna structure from the start of the design may have improved the diversity gain over the retrofitted antenna. Nonetheless, we use these diversity gains to evaluate the modal antenna in an actual cellular system.

The total efficiency of the retrofit antenna mode 0 and the baseline, unmodified main
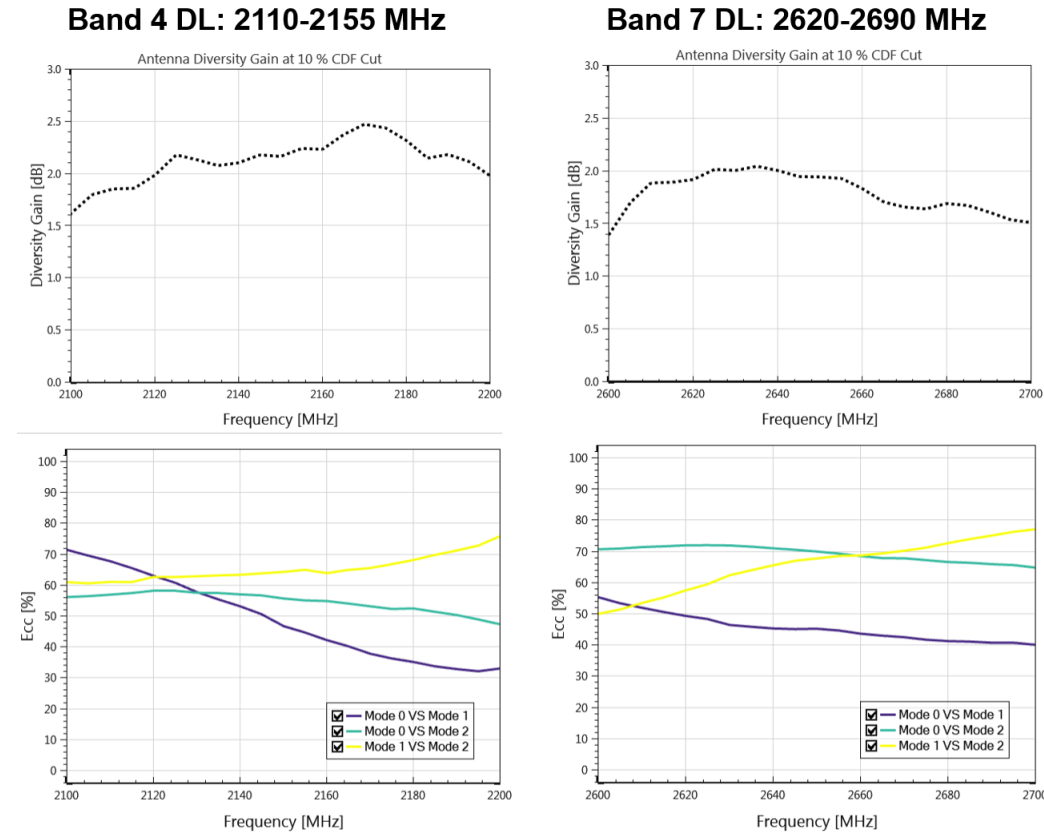
Figure 4.3: Plots on the left show the diversity gain at the 10% CDF cut and ECC for three mode antenna system for downlink LTE Band 4. Plots on the right show the diversity gain and ECC for the antenna system for downlink LTE Band 7.

antenna are between 30-35% across both bands. Throughout the field trial we compare the three mode antenna system to the fundamental mode 0 of the antenna. Mode 0 refers to the state of the antenna structure in which the parasitic element is open to the ground plane and only the main fed element is driven. This provides an accurate baseline for A to B (active versus passive) comparisons as we are comparing antenna systems that utilize the same volume and placement within the phone.

In addition to the antenna system, we also implement the state prediction process in software on the phone. We develop an Android kernel driver to query baseband diagnostic information, such as SINR, BLER, throughput, and LTE resource blocks, to be used as CQI inputs to our state prediction algorithm. We use an algorithm in which each mode of the antenna is assigned an NLMS filter to track its CQI updates. The algorithm is written as a user space application that gathers CQI via ioctl calls into the baseband diagnostic kernel

driver.

Furthermore, we log the key performance indicators directly to the SD card on the phone. This implementation is limited to 25 ms between baseband queries due to latency of the baseband interface and process context switching overhead. The effect of the baseband CQI latency is explored for the fast fading walking and driving test cases in section 4.4. We generate cellular traffic on the network by initiating a large file transfer protocol (FTP) download, while at the same time logging the KPIs locally on the phone. Figures 4.4 and 4.5 show the setup.

4.3   Field Test Scenarios

We repeat the modal antenna retrofit on twenty identical units of the handset. The following field test scenarios are considered. To the best of the author's knowledge, this represents the first comprehensive field test of a modal link-adaptive antenna in a handset.

1. LTE Bands: Band 4, Band 7

2. Channel Conditions:

   a) Near-cell: SINR $>$ 20 dB

   b) Mid-cell: 5 dB $<$ SINR $<$ 20 dB

   c) Cell edge: SINR $<$ 5 dB

3. Number of identical handset retrofitted with modal antenna: 20

4. Field Test Hours: 2000+ hours logged

5. Data Collection Period: 3 months

6. Test Conditions: Stationary, Slow rotation (10 deg/s), Walking (5 km/h), Driving (30-70 km/h)

7. Test Locations: Suburban, Rural, Urban

The design of the field test covers the most common cellular use cases and channel conditions. The goal is to collect enough data to be able to determine the impact of a single antenna diversity gain of 2-3 dB on the capacity and reliability of an LTE network. We also evaluate the effectiveness of the state prediction process across slow and fast fading channels.

The test cases are illustrated in Figure 4.6. We evaluate the performance of modal antenna systems as a function of different channel speeds from static to medium speed driving. Figure 4.7 shows the cell tower layout for the LTE Band 7 stationary and semi-stationary test cases. Figure 4.8 shows an example route for the LTE Band 4 driving test cases.
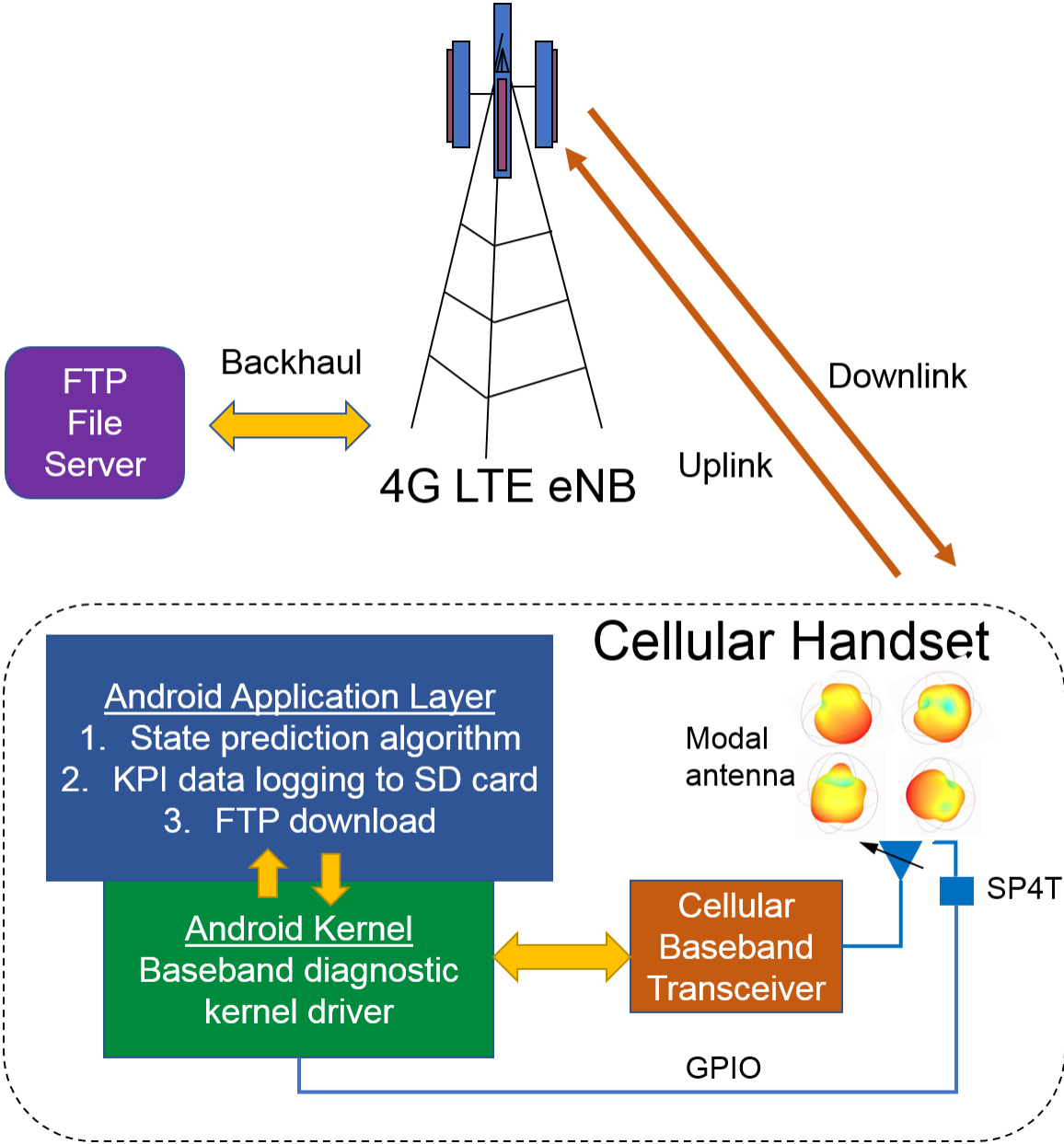
Figure 4.4: Modal antenna field test implementation. The state prediction algorithm, logging, and baseband diagnostic drivers are written for the Android operating system and run locally on the phone. Large FTP file transfers are used to pass data traffic between the 4G LTE eNodeB (eNB) and the cellular handset equipped with a modal antenna.
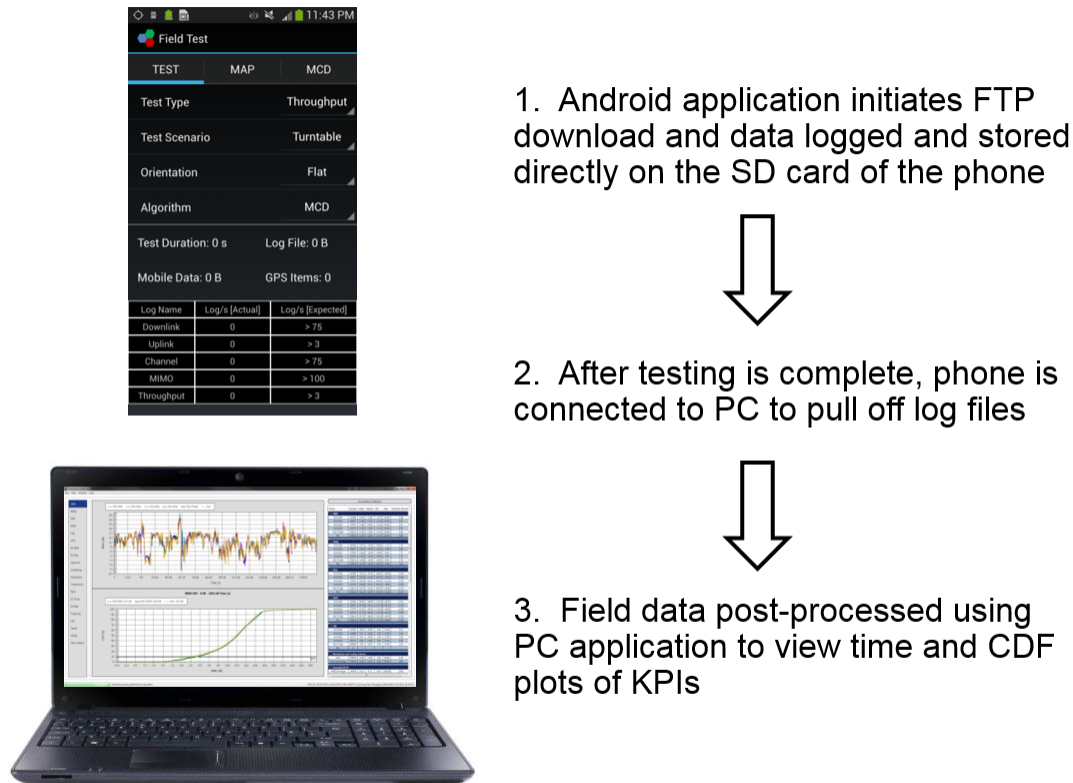
Figure 4.5: Process to log LTE Physical Layer KPIs locally to the SD card of the phone. After the test is complete, the log files are pulled off of the phone and post-processed using a PC application. KPIs are analyzed across time, statistical CDF, and latitude/longitude of the phone.

4.4 Measured Field Results

In this section, we summarize the key findings from the modal link-adaptive antenna cellular field trials. We divide the results section into four areas: impact of UE speed on the state prediction algorithm, the effect of single antenna diversity on spatial multiplexing, adaptation to inter-cell interference, and aggregate network capacity results.

State Prediction Speed Limitations

We begin by discussing the measured limitations of the state prediction process for walking and driving channel conditions. The state prediction process switches between the radiation modes in time. Therefore, the CQI inputs to the process must be sampled fast enough

Figure 4.6: Cellular field test use cases (1) stationary, (2) walking, (3) slow rotating turntable (4) driving. In all cases, multiple units are measured simultaneously to increase the sample size of the test and to capture multiple fading channel conditions at the same time.
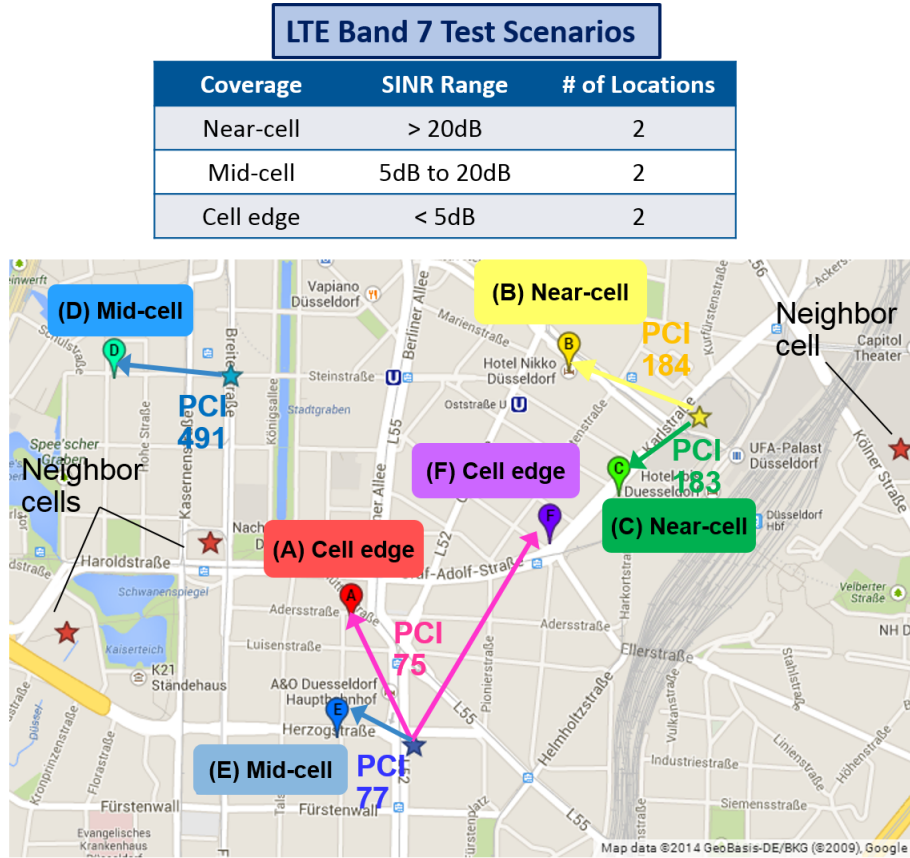
Figure 4.7: Layout of different channel conditions on LTE Band 7 network for stationary and turntable tests. We use 2 locations for each of the coverage cases: near-cell, mid-cell, and cell edge. Note that one cell tower may broadcast multiple physical cell identities (PCIs) across different antenna array sectors.

to track the channel state for each mode.

Figure 4.9 shows the measured SINR for walking (6 km/h) and driving speeds (40 km/h). As can be seen from the zoomed in plots, the SINR may change as much as 2-4 dB between individual SINR samples for both walking and driving use cases. The channel variance is too large for the NLMS filter to accurately track with a sample time of 25 ms. To make matters worse, if one of the radiation modes is not trained for a long time, its CQI estimate will become outdated, resulting in a large filter error when the mode is eventually selected.

Recall that our implementation of the state prediction process in this particular handset is limited by the data transfer rate from the baseband interface to the applications processor. The SINR is sampled at a nominal rate of 25 ms. Performance of the state prediction process at higher user speeds may be improved by implementing the algorithm directly at the baseband physical layer in order to sample the channel at a faster rate (e.g. 1 ms, or
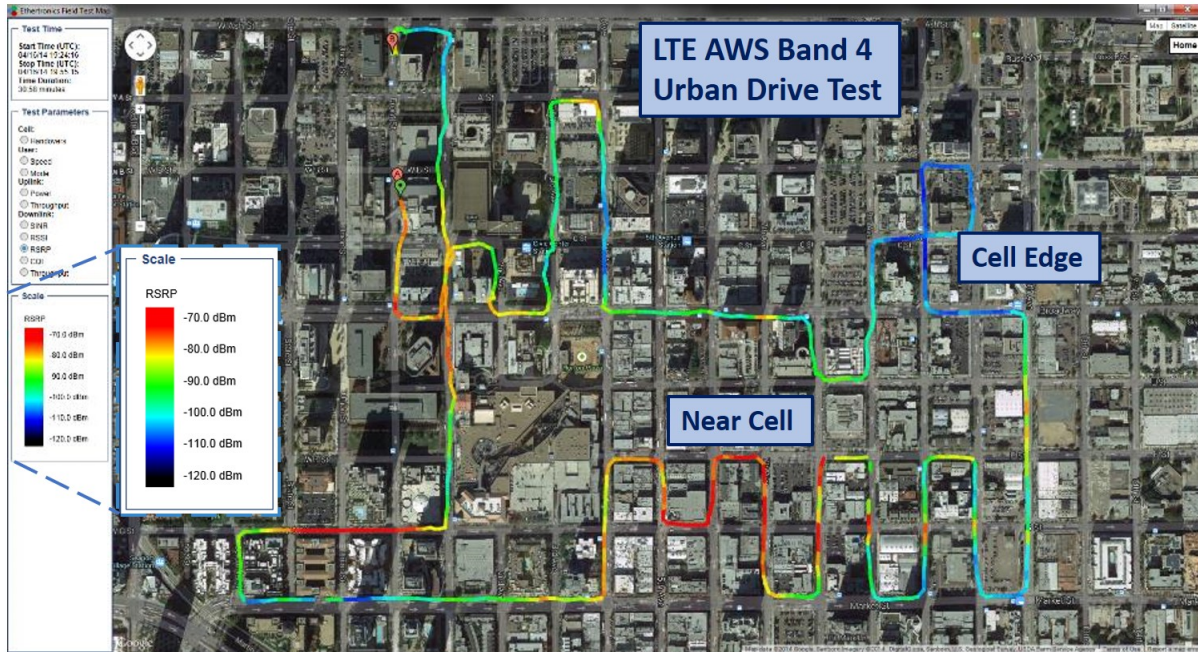
Figure 4.8: Sample urban drive route for network using LTE AWS Band 4. The RSRP (LTE cell pilot channel power) and SINR are logged across latitude and longitude to classify the different channel conditions from near-cell to cell edge.

once per LTE subframe).

Despite these limitations, we report a median 0.4 dB increase in SINR and 6% increase in spectral efficiency when switching between the three modes (hereby referred to as active) as compared to mode 0 of the antenna across more than 400 hours of walking and driving field tests. Even though the algorithm may not always select the optimal antenna mode in these cases, we believe that positive antenna diversity is introduced by changing between the modes, which reduces the likelihood that one of the antennas will be stuck in a null of the multipath channel for a long time.

Improved Spatial Multiplexing Performance

Although we have only retrofitted the primary cellular antenna with a modal antenna system, there is still an improvement in MIMO performance for certain channel conditions. When the SINR is not matched between MIMO antennas, the baseband may revert to a diversity scheme so as to favor improved reliability over improved data rate. Per equations (1.43) and (1.44), spatial multiplexing is most useful when the eigenvalues of the channel matrix are comparable (condition number close to 1).
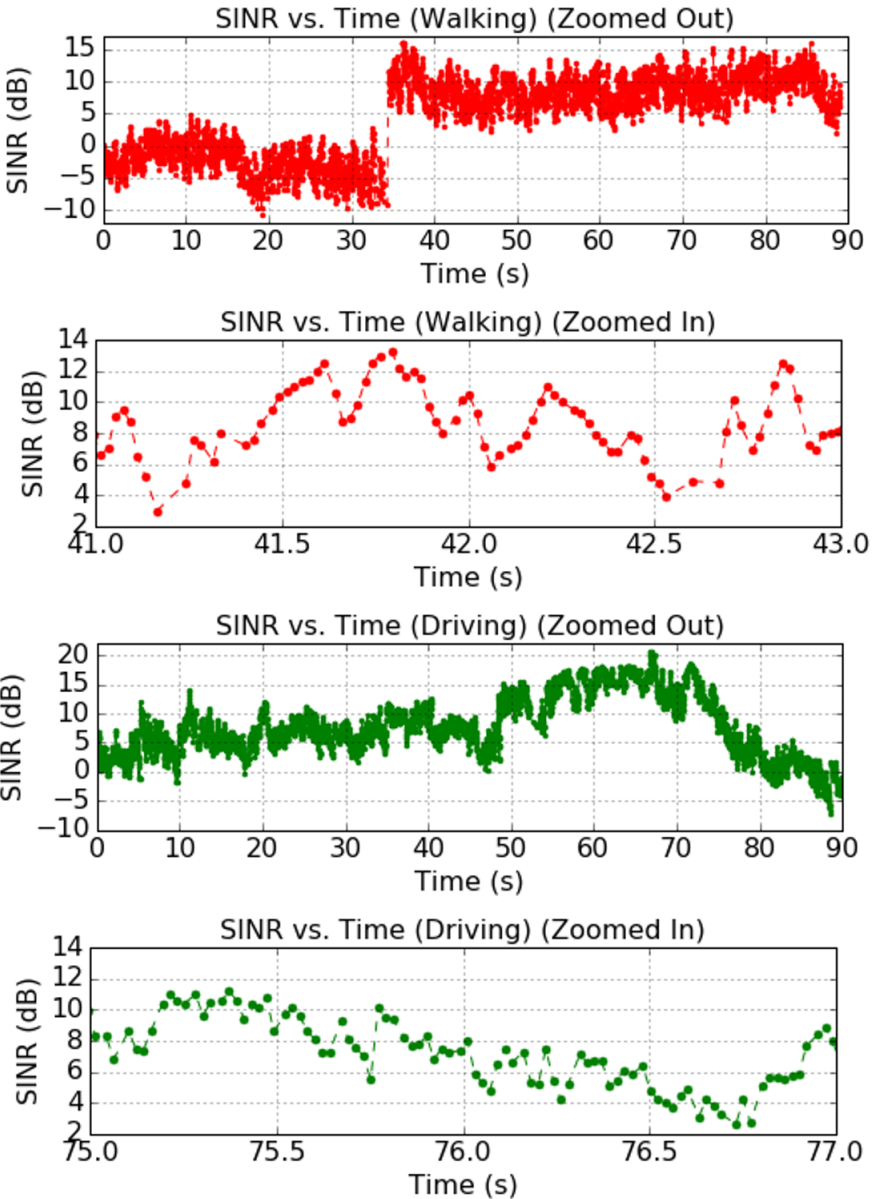
Figure 4.9: SINR samples for walking (6 km/h) and driving (40 km/h) use cases at sample rate of 25 ms. A cell handover occurs at time = 34 s for the walking case.
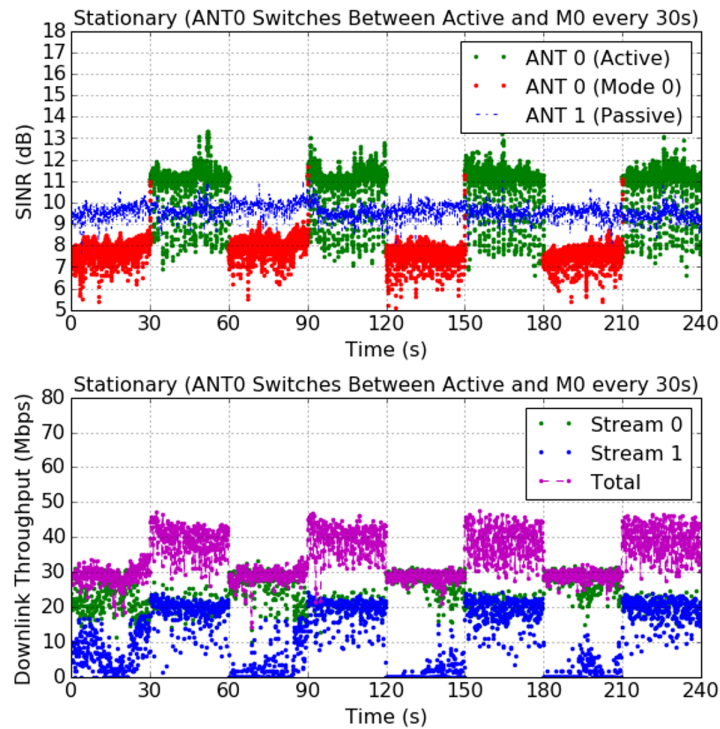
Figure 4.10: Top plot: SINR vs. time for the diversity antenna (ANT 1) and primary antenna (ANT 0). For the primary antenna, we alternate between mode 0 and turning on the state prediction process to select the best of the three possible antenna modes (active). Bottom plot: Corresponding throughput per MIMO antenna stream.

Figure 4.10 shows one such example of this case. We alternate between mode 0 of the primary antenna and active (or the three modes of the link-adaptive antenna system). In the case that the fixed mode of the antenna experiences a fade, an SINR mismatch of 2-3 dB can be observed between MIMO paths. We can improve the SINR on the primary antenna by switching to another one of the antenna modes. The result is a comparable SINR on both paths, which triggers the baseband to start using spatial multiplexing more often. Thus, the downlink throughput is increased from 30 to 45 Mbps when the SINR between the two receive paths is better matched.

Inter-Cell Interference Mitigation

One benefit of a modal antenna system is the ability to adapt the antenna to the propagation channel between the handset and the serving cell tower. In addition, modal antenna systems may also be used to adapt the antenna to minimize the power coming from interfering signals. For actual cellular deployments, users at the cell edge may receive signals from

Table 4.2: Median SINR, RSRQ, RSRP, RSSI for the inter-cell interference mitigation experiment.

Median	Mode 0	Active
SINR	-1.2 dB	+1.2 dB
RSRQ	-14.3 dB	-13.2 dB
RSRP	-101.5 dBm	-101.2 dBm
RSSI	-69.7 dBm	-70.8 dBm

multiple towers, not just their serving cell. One of the neighboring cells may be serving users in its network on the same time and frequency slots as an adjacent cell. This effect is known as inter-cell interference (ICI). ICI reduces the SINR of users at the edge of adjacent cells.

LTE has introduced methods known as enhanced ICI coordination to reduce the impact of inter-cell interference [12]. However, these algorithms typically sacrifice bandwidth or power in cases that the neighboring eNBs use lower transmit powers on time and frequency resources shared between cell edge users [36]. Interference coordination techniques trade off between resource fairness and quality of service (QoS). More complex heterogeneous networks and small-cell technologies further complicate ICI as low-power femtocells and picocells are introduced in the same coverage areas as high-power macrocells [30].

We explore the effect of using a modal antenna to reduce ICI inherent to LTE network deployments. In our modal handset implementation, we use SINR as the CQI input to the state prediction process. Reducing the interference term in the denominator of SINR may actually be more important than maximizing the serving cell signal for improving the data rate in cell edge conditions. We design an experiment to measure the link margin for our modal antenna handset, which receives power from two interfering cells (PCI 110 and PCI 209) and one serving cell (PCI 380) (Figure 4.11).

We log the SINR, RSRP, RSSI, RSRQ samples for 3 separate one hour download sessions. Every 60 seconds of the session, we alternate between mode 0 of the modal adaptive antenna and enabling the state prediction process (using all three radiating states of the antenna). Table 4.4 shows the median results and Figure 4.12 plots the corresponding statistical distributions.

The results show that the state prediction algorithm increases the SINR and RSRQ by 2.4 dB and 1.1 dB, respectively. However, the serving cell pilot signal (RSRP) is only increased by 0.3 dB and the median RSSI, or total power at the receiver, is actually reduced by 1.1 dB in the active case. Thus, the improvement in SINR primarily comes from switching to an antenna mode that reduces the power from neighboring cells, as opposed to just maximizing the power from the serving cell.

Given this insight, we analyze the relationship between RSSI and SINR for all field test conditions for stationary and semi-stationary test cases, which constitutes more than 1000 hours of field test data. Figure 4.13 plots the histograms for near-cell and mid-cell as compared to cell edge cases. Near, mid, and cell edge cases are defined in section 4.3. We
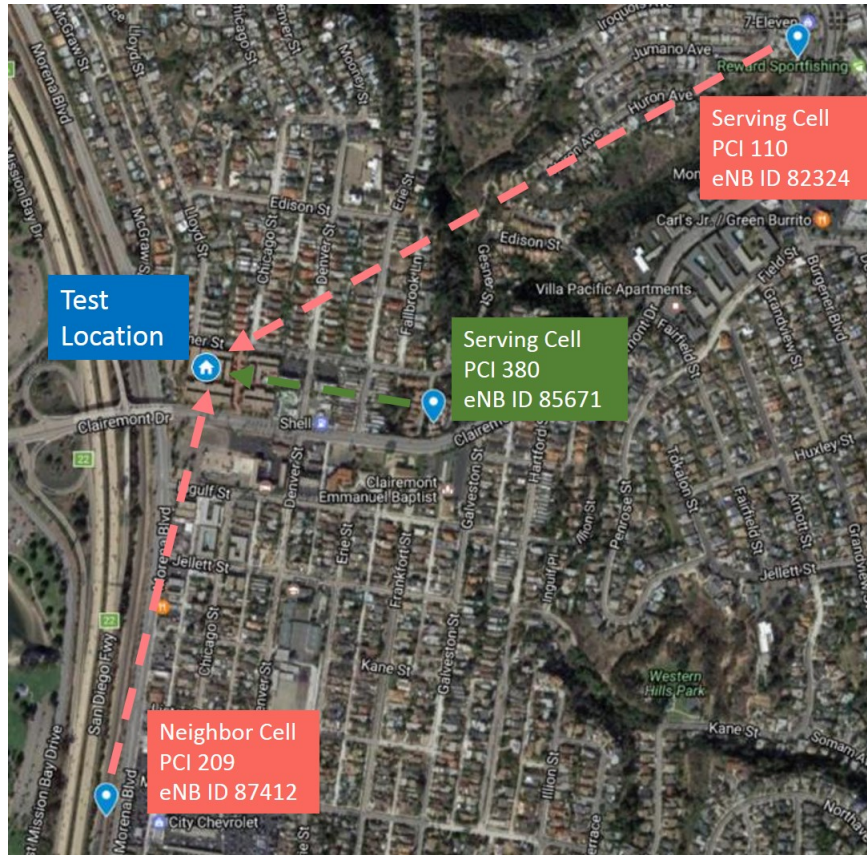
Figure 4.11: ICI test map. PCI 380 is the serving cell and PCI 110 and PCI 209 are neighboring, interfering cells.

define the difference in SINR between the active state of the three mode antenna and mode 0 of the same structure:

$$\Delta SINR = SINR_A - SINR_{M0} \tag{4.2}$$

and the same for RSSI:

$$\Delta RSSI = RSSI_A - RSSI_{M0}. \tag{4.3}$$

We observe an average ΔSINR of 1.5 dB for all cell locations. The ΔRSSI distribution for near-cell and mid-cell is skewed to the right with a average of 0.51 dB. Close to the eNB, the handset selects the modes of the antenna to maximize the power, which is primarily coming from the serving cell. However, the RSSI distribution at the cell-edge is skewed to the left with an average of -0.67 dB. At the cell edge, the modal antenna system actually reduces the total power compared to a passive antenna with a single radiation state. This is because at the cell edge the receiver also receives power from the interfering cells.
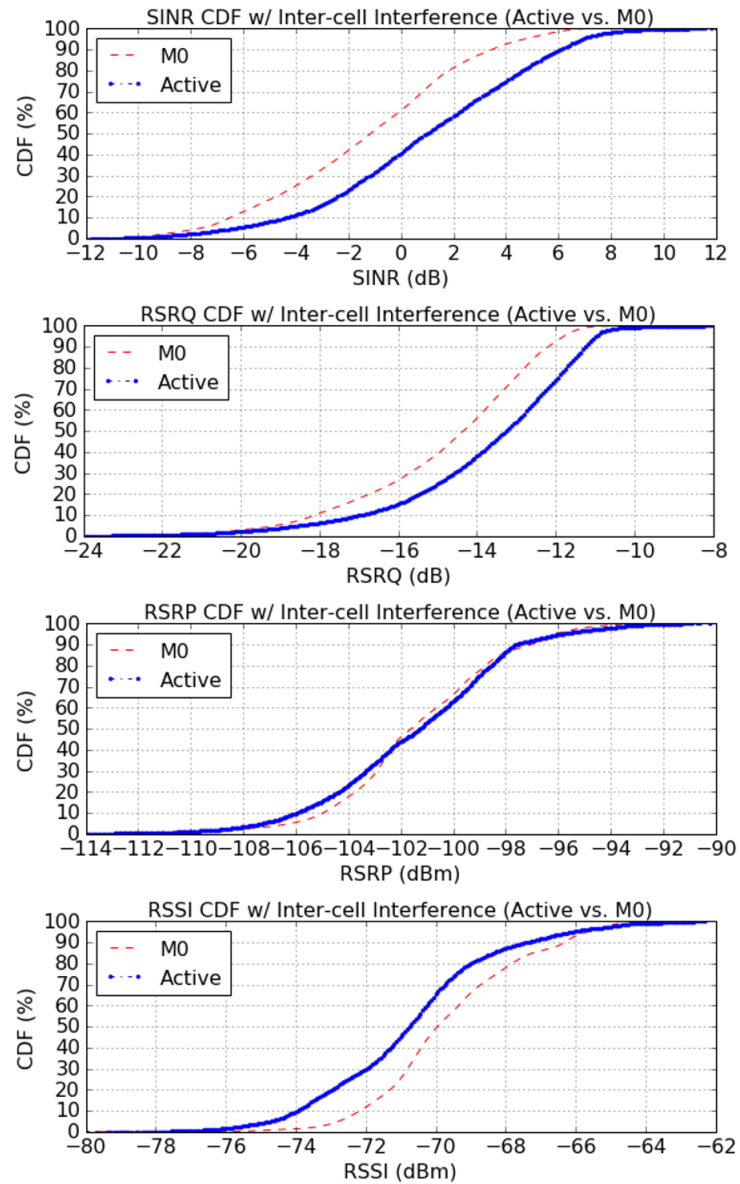
Figure 4.12: SINR, RSRQ, RSRP, RSSI cumulative distribution functions for the inter-cell interference test experiment. The SINR is higher and the RSSI is lower for the active antenna compared to the antenna with the fixed radiation pattern because the active antenna reduces the power coming from the interfering cells.
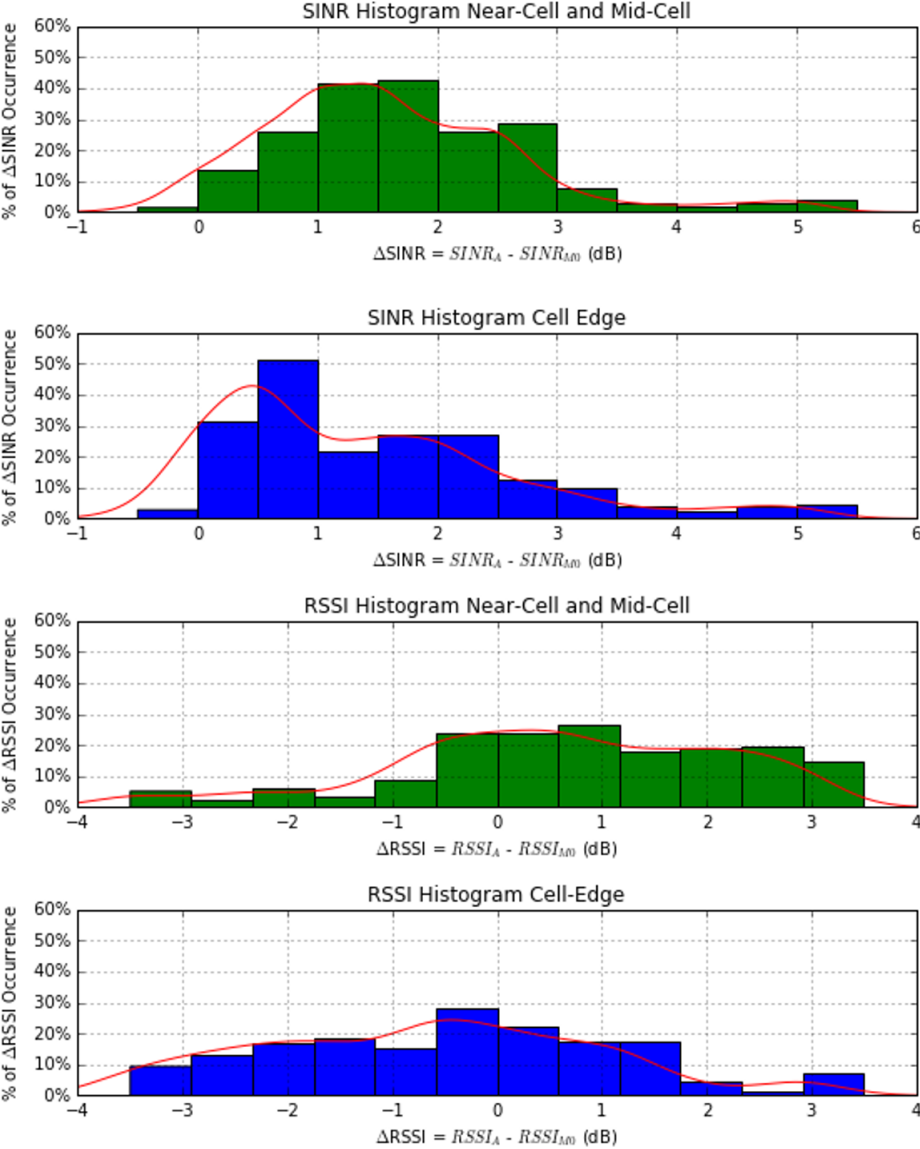
Figure 4.13: Histogram of RSSI and SINR comparing active versus mode 0. For cell edge cases, the RSSI or total receive power is lower for active state compared to mode 0. The SINR is improved for both near-cell, mid-cell, and cell edge conditions.

Figure 4.14: Measured spectral efficiency and throughput percentage improvements comparing mode 0 of the modal adaptive antenna system to the three mode system for all field channel conditions for stationary and slow rotating test cases.

Network Capacity Results

Figure 4.14 summarizes the throughput and spectral efficiency percentage improvement for all stationary and slow rotating field test scenarios. The plots show the aggregated data for both LTE Band 4 and LTE Band 7 networks. The spectral efficiency and throughput are plotted as a percentage improvement for using the state prediction process with the three mode antenna system compared to mode 0 of the same antenna system. The y-axis shows the percentage of occurrences of that improvement. The cell edge histogram is skewed to the right for cases in which mode 0 of the antenna is in a deep fade, for which the percentage improvement could be greater than 50% by improving the link margin and increasing one MCS step.

The spectral efficiency and throughput distributions are similar. This is due to the fact that the data rate increase comes from improving the link budget and increasing the MCS, and thus the efficiency of the transmission scheme. We report an average spectral efficiency

improvement of 25.2% and an average throughput improvement of 25.4% when using a modal adaptive antenna compared to an antenna with a fixed radiation pattern.

These measured results are in good agreement with the LTE AMC simulations for a Rayleigh faded channel distribution. Per Table 4.1, an average SINR increase of 2.3 dB results in an average increase in spectral efficiency of 30%. Recall that the modal antenna used for these experiments had a diversity gain between 1.5 and 2.5 dB depending on the frequency in LTE band 4 and 7.

In other words, if every cellular handset on the network were retrofitted with a modal antenna, the network operator could maintain the same data rate, but use 25% less bandwidth compared to the case if each handset had a passive antenna. Alternatively, the operator could offer each of its users 25% higher data rates and use the same amount of bandwidth.

Chapter 5

Applications for Indoor Wireless Networks

In this section, we examine how improving the link budget by using a modal adaptive antenna system translates into increased spectral efficiency for wireless local area networks (WLANs). We will evaluate the performance of modal adaptive antenna systems using simulated and measured results from indoor propagation environments. We explore the performance impact of modal antenna systems for WLANs for both transmit and receive and for both access points (APs) and clients. We focus on 802.11ac for our active experiments because devices for retrofit measurements are readily available.

5.1 WLAN Link Parameters

Similar to cellular operators, WLAN service providers are looking to improve network throughput and reliability for their indoor wireless networks. Applications such as high-definition (HD) and ultra-high definition (UHD) video consume an ever-increasing amount of bandwidth on WLAN networks. With the introduction of 802.11ac and future standards like 802.11ax, the WiFi industry is using various physical layer techniques, such as configurable 20/40/80/160 MHz bandwidths, 2/3/4/8 antenna MIMO, beamforming, multi-user MIMO, and OFDMA to better utilize spectrum in the unlicensed 2.4 GHz and 5 GHz frequency bands. Today, 2.4 GHz networks are overcrowded with legacy WLAN devices. As more devices come onto the 5 GHz band, it too will become overcrowded, reducing the QoS for clients on the network.

802.11ac and legacy IEEE 802.11 WLAN standards use adaptive modulation and coding to best utilize their spectrum across all distances between access points and clients. The standard itself specifies minimum receive sensitivity values for deployed devices to successfully decode each MCS index (Table 5.1). 802.11ac introduced 256QAM and 802.11ax will use 1024QAM to increase the peak data rates. However, these higher-order QAM modulations come with stringent transmitter and receiver error vector magnitude (EVM) requirements

Table 5.1: Table of MCS and sensitivities in 802.11ac [4]. The receive sensitivity (S) in dBm represents the minimum sensitivity as required by the 802.11ac specification for a single spatial stream. The corresponding spectral efficiency includes the overhead from the OFDM guard interval and pilot subcarriers.

MCS	Mod.	CR	S (dBm) 20MHz	S (dBm) 40MHz	S (dBm) 80MHz	S (dBm) 160MHz	η (bps/Hz)
0	BPSK	1/2	-82	-79	-76	-73	0.37
1	QPSK	1/2	-79	-76	-73	-70	0.73
2	QPSK	3/4	-77	-74	-71	-68	1.09
3	16QAM	1/2	-74	-71	-68	-65	1.46
4	16QAM	3/4	-70	-67	-64	-61	2.19
5	64QAM	2/3	-66	-63	-60	-57	2.93
6	64QAM	3/4	-65	-62	-59	-56	3.29
7	64QAM	5/6	-64	-61	-58	-55	3.66
8	256QAM	3/4	-59	-56	-53	-50	4.39
9	256QAM	5/6	-57	-54	-51	-48	4.88

to facilitate decoding the constellation. The percentage increase in spectral efficiency from introducing 256QAM for MCS values 8 and 9 is only 15-20% (Figure 5.1), and in practice, higher order modulation is only really useful close to the access point where the throughput and link budget is already good.

802.11ac also incorporates transmit beamforming at the access point to constructively combine the signals of an antenna array. As discussed in previous sections, beamforming improves the link budget to the system, but comes with a higher peak gain of the antenna array, which is limited by the FCC. Because the same copy of the signal is sent with amplitude and phase offsets, beamforming uses multiple antennas to provide a power gain to the system, instead of capacity enhancements as in spatial multiplexing. As long as the access point has a surplus of antennas compared to the clients, which is usually the case for WLANs, the access point may use the extra antennas to beamform one or more of its data streams.

Newer WLAN standards, such as 802.11ac and 802.11ax also increase the amount of bandwidth one access point can occupy. Increasing the bandwidth increases the peak throughput, but also adds to more network congestion as one AP may consume up to 4 frequency channels. Furthermore, doubling the bandwidth also reduces the receive sensitivity by 3 dB, which means that clients must be closer to the AP to maintain a given MCS. Figure 5.1 plots the average RSSI to achieve an increase in MCS by one step for a single spatial stream. The biggest percentage increase in spectral efficiency comes at the lowest MCS values when the link margin is weakest. Clients in these locations benefit the most from improved antenna system gain. Since the weakest clients consume the largest amount of network resources, the other clients on the network will also see an improved QoS as the access point has more time and bandwidth to spend on them too.
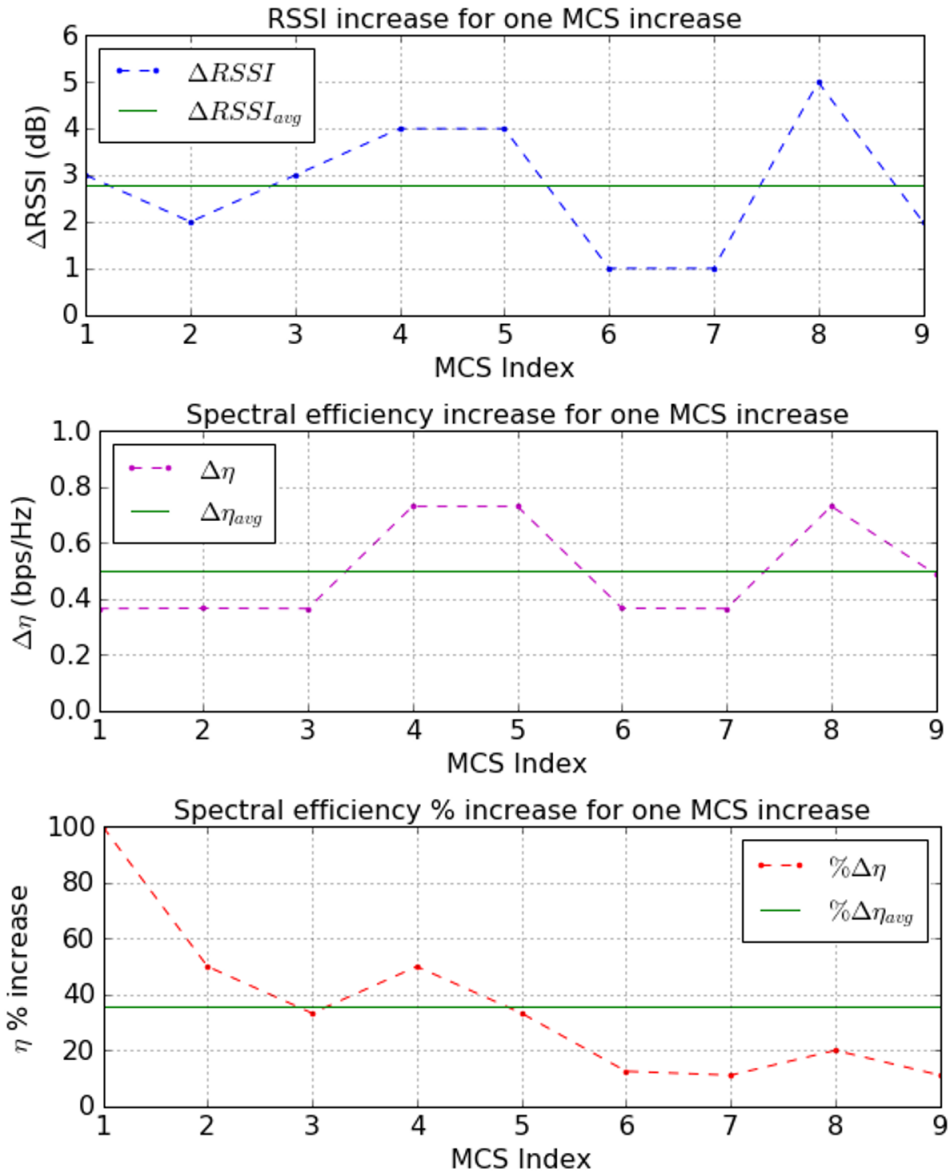
Figure 5.1: RSSI increase for one MCS increase (top), spectral efficiency increase for one MCS increase (middle), and spectral efficiency percentage increase for one MCS increase (bottom) for 802.11ac. An average RSSI increase of 3 dB corresponds to an increase in spectral efficiency of 0.5 bps/Hz and a spectral efficiency percentage increase of 35%.
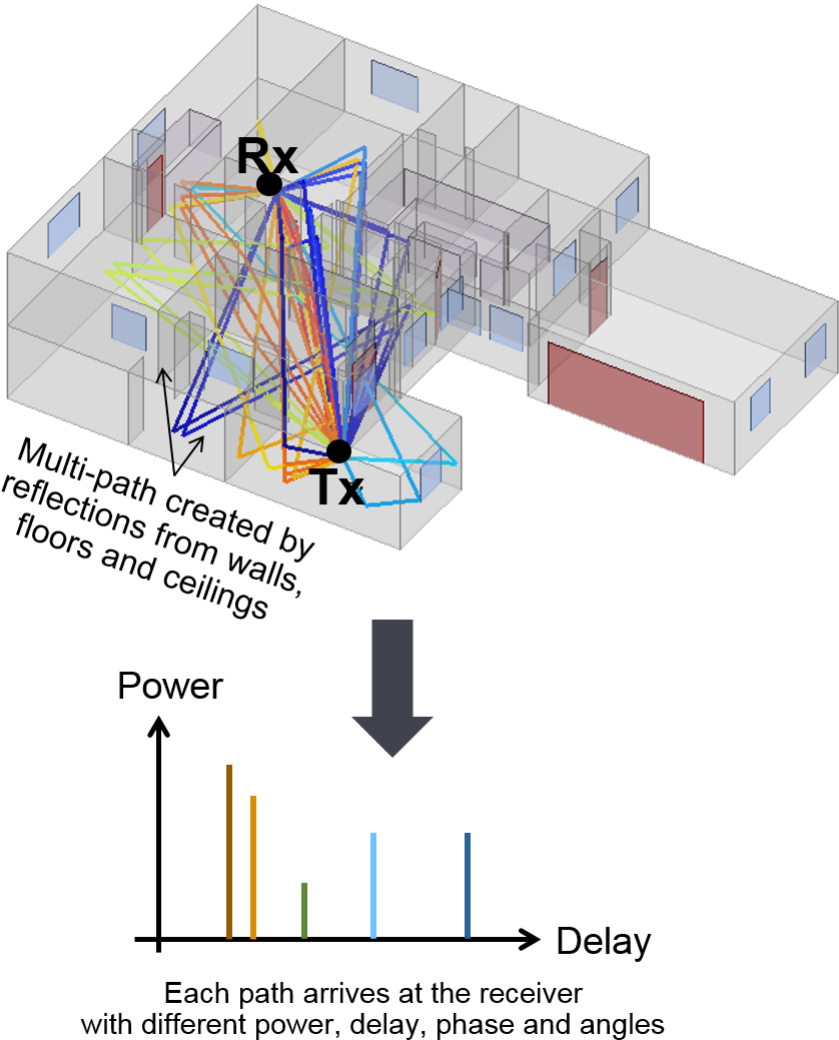
Figure 5.2: 3D building model of the test house and depiction of multipath reflections from the transmitter to the receiver.

5.2 Indoor Propagation Simulations

We use the indoor propagation simulator Volcano Labs from Siradel [10] to explore the effect of improved link margin by using modal adaptive antennas. Volcano Labs uses geometrical optics and the uniform theory of diffraction to simulate the indoor propagation of RF waves. The simulation tool computes the amplitudes, delays, and phases of the channel impulse response considering the path losses between the transmitter and the receiver (Figure 5.2).

We import the 3D building model of an actual 3,200 square foot home, including dielectrics for walls and furniture (Table 5.2 and Figure 5.3). Volcano Labs software also includes 3D radiation patterns at the transmitter and receiver when calculating the ray-based propagation through the channel. That is, the 3D radiation patterns are convolved with the angular power distribution of the multipath propagation environment. The simulation parameters are summarized below:

- Frequency: 5180 MHz.

- Point to area: access point located in the office transmitting to client locations throughout the house.

- Pixel x, y step size: 5cm x 5cm.

- Access point azimuthal rotation: 0 degrees to 330 degrees in steps of 30 degrees.

- Access point height: 1m.

- Access point antenna positions (Figure 5.9):

    - ANT1 (x,y): (0cm, 0cm)
    - ANT2 (x,y): (4cm, 0cm)
    - ANT3 (x,y): (8cm, 0cm)
    - ANT4 (x,y): (13cm, 0cm)

- Access point transmit power: 20 dBm.

- Each of the four antennas at the access point is equipped with a four-mode link-adaptive antenna system.

- Client locations use the radiation pattern from mode 0 of antenna 1.

- Client height: 1m.

The receive signal strength (RSS) calculation also takes into account beamforming at the access point. For each pixel, we coherently combine the signals from each of the four access point antennas. The complex channel impulse response with M taps from antenna n is:

$$Rx_n(\tau) = \sum_{m=1}^{M} a_m e^{j\phi_m} \delta(\tau - \tau_m). \tag{5.1}$$

At each received pixel, we get the amplitude (a_m), phase (ϕ_m), and delay (δ_m) of the power delay profile for the channel at each of the four antennas:

Figure 5.3: First floor layout of the test hose including simulation materials.

Table 5.2: Real and imaginary relative permittivities for 5 GHz indoor propagation simulations [35] [61] [64].

Layer	Material	$\mathbf{Re}\{\epsilon_R\}$	$\mathbf{Im}\{\epsilon_R)\}$
Floor	Concrete	8	0.5
Garage Door	Metal	-1	0
Furniture	Wood	2.06	0.46
Windows	Glass	9.63	0.47
Stairs	Wood	2.06	0.46
External Walls	Concrete	8	0.5
Internal Walls	Plasterboard	2.4	0.03
Doors	Wood	2.06	0.46

$$Rx(\tau) = \sum_{n=1}^{4} Rx_n(\tau) \tag{5.2}$$

To coherently combine the complex path signals, we set the phase of each of the paths to zero as if the access point had pre-coded the signal to phase match each of the spatial streams. Thus, the RSS at each pixel becomes:

$$RSS = \left| \sum_{n=1}^{4} Rx_n(\tau)|_{\phi_m=0} \right|^2 . \tag{5.3}$$

We equip the access point with a four-mode antenna system at each of its four antennas. That is, the access point has 256 possible antenna mode combinations. At each pixel, we compare the RSS for each of the 256 possible antenna mode combinations at the access point against the fixed modes: mode 0, mode 1, mode 2, and mode 3. Figure 5.4 shows the CDF of the results for both floors of the test house. The active curve represents selecting the antenna mode combination that provides the maximum RSS at each of the pixels. With these measured antenna patterns, we observe that adapting the antenna modes to the propagation channel provides a 2-2.5 dB median increase in Rx power for each of the simulated client locations in the test house. This agrees with the measured single antenna diversity gain average (at the 50% CDF cut) of 2.3 dB for these four antennas at 5180 MHz.

We extend the analysis by considering how RSS translates into MCS and throughput using Table 5.1 with sensitivity values for a bandwidth of 160 MHz. Thus, we map the pixel RSS into a throughput and MCS value comparing the best case active antennas (the maximum RSS of the 256 mode combinations for each pixel) to the fixed mode 0 radiation state for all antennas. Figures 5.5, 5.6, and 5.7 highlight the RSS, MCS, and throughput results for the second floor of the home. We observe that the biggest increase in RSS occurs at the corners of the rooms in locations far away from the access point. At these locations, the MCS can increase anywhere from 1 to 3 steps and the throughput by 50+% as a result.
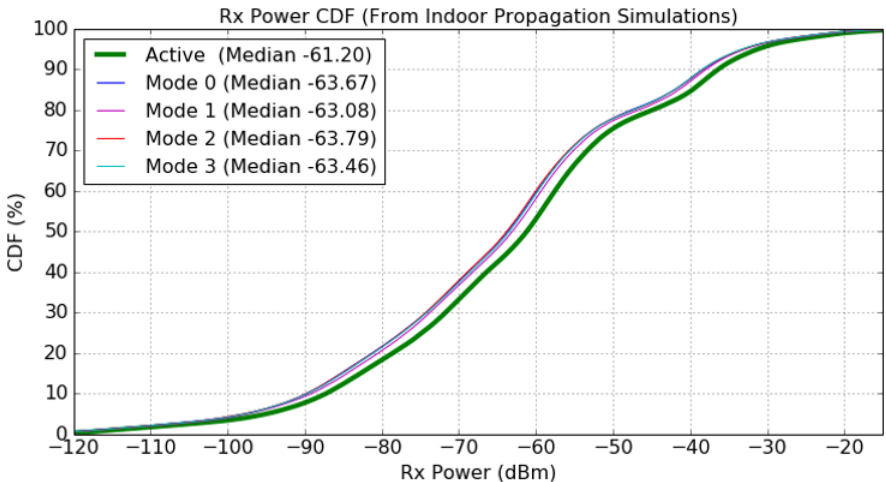
Figure 5.4: CDF of RSS for the indoor propagation simulations. Active indicates the distribution of maximum RSS at each pixel from the 256 possible antenna mode combinations.
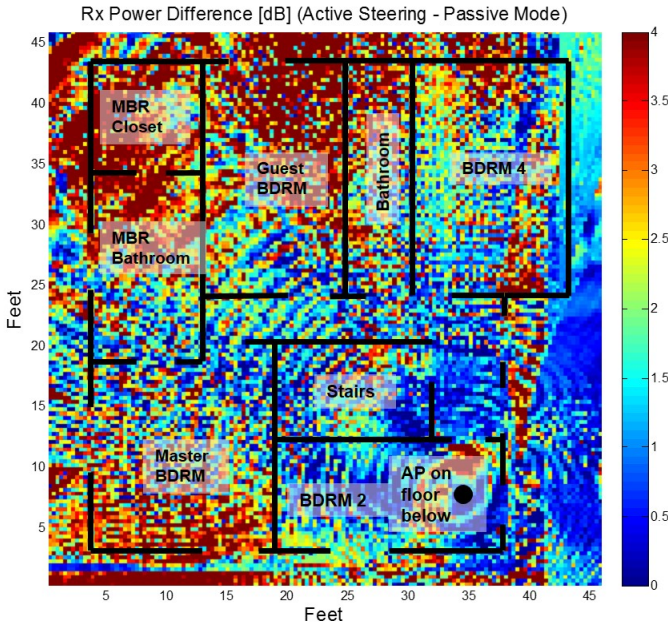

Figure 5.5: RSS difference $(RSS_{Active} - RSS_{M0})$ map for second floor.
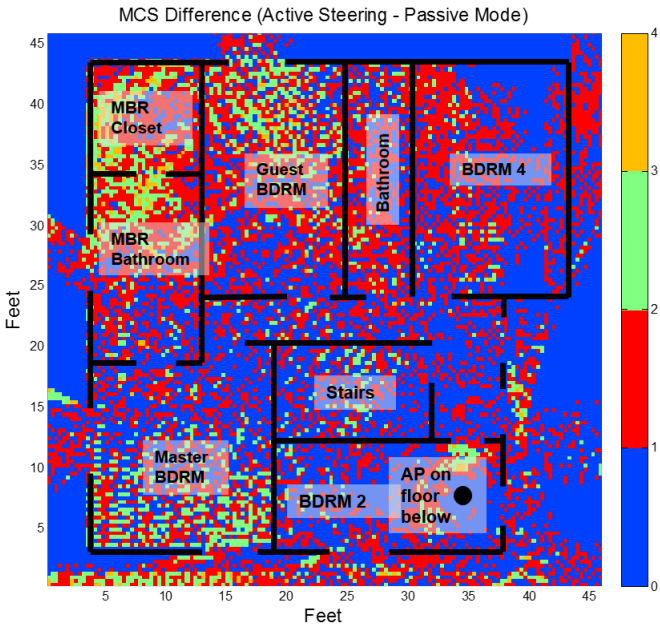
Figure 5.6: MCS difference $(MCS_{Active} - MCS_{M0})$ map for second floor.
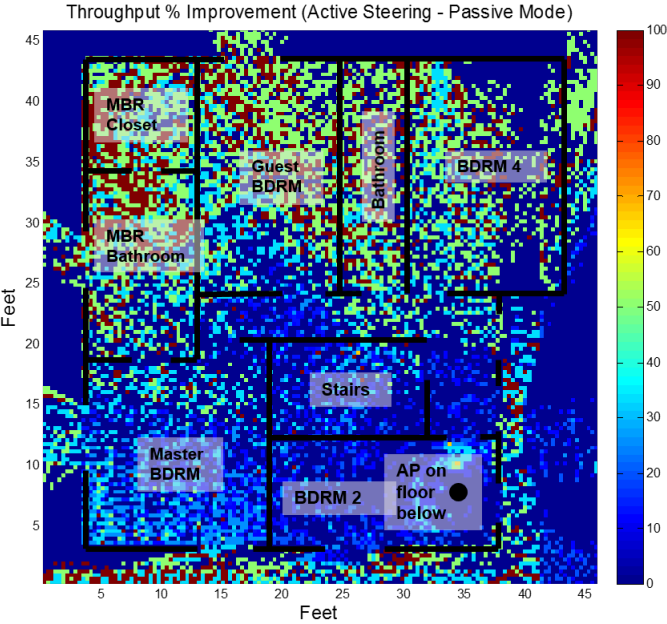
Figure 5.7: Throughput percentage difference (comparing active throughput vs. mode 0 throughput) map for second floor.
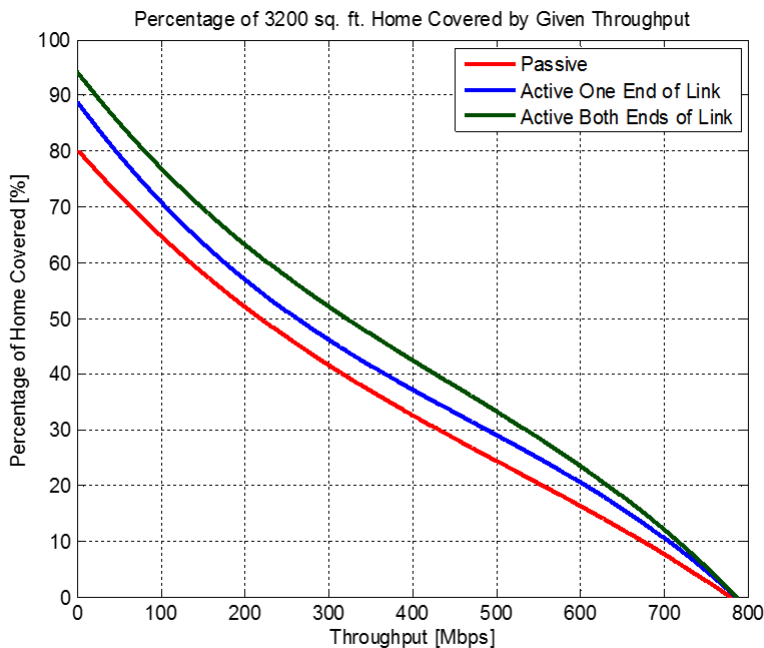
Figure 5.8: Percentage of home covered by a given throughput from the indoor propagation simulations.

From these coverage maps, we can also plot the percentage of the home covered by a given throughput for a 4 antenna access point beamforming to a client with a single antenna using 160 MHz bandwidth (Figure 5.8). We also show the improvement in coverage by adding reconfigurable antennas at both the access point and client (both ends of the link). In this case, the link margin is increased at both the transmitter and receiver. This throughput distribution shows that MCS 8 and 9 (>700 Mbps) are only used for approximately 10% of all coverage cases in the home and that the physical layer throughput is less than 200 Mbps for about 50% of the use cases. For the passive case (mode 0 for all antennas), about 20% of the home is covered in dead zones where the throughput goes to 0 Mbps. With active on one end of the link and both ends of the link, the percentage of dead zones is reduced to 11% and 6%, respectively.

5.3   Measured Results for Link-Adaptive MIMO Antenna Systems

In addition to the simulation data, we also retrofit a 4 antenna router with active antennas for experimental throughput measurements. We compare the reconfigurable antennas to passive printed dipoles in the 5 GHz band. We extract the per-antenna RSSI from the Linux
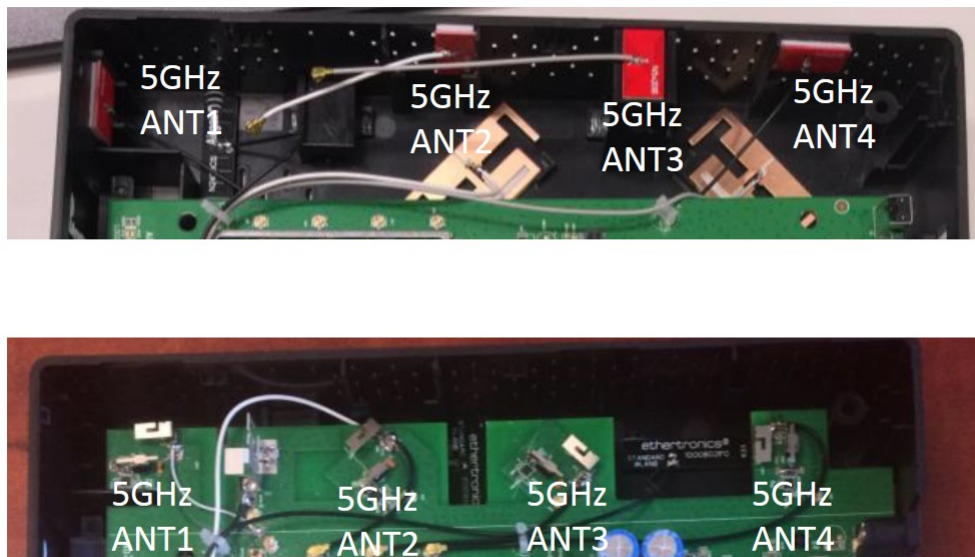
Figure 5.9: Access point antenna positions for the indoor WLAN throughput measurements. The top image shows four passive printed dipole antennas, which are the baseline for the study. The bottom image shows four modal antennas. Each of the four modal antennas has four radiation states. Thus, the four antenna active system has 256 radiation mode combinations.

operating system on the router to be used as the CQI input to four separate state prediction processes. We use the same training and NLMS learning parameters as in the previous chapter.

Because we do not have access to the physical layer firmware or per-antenna SINR from the WLAN baseband processor, our prediction process is used to optimize the RSSI of each of the antennas individually. A more optimal approach would be to incorporate the state of the antennas in conjunction with the beamforming and spatial multiplexing and diversity algorithms running on the baseband.

In a MIMO system, adapting each of the individual antenna elements benefits beamforming and spatial multiplexing. Consider the case in which one of the antenna elements in the array experiences a null of the multipath channel. In this case, selecting another antenna radiation state that is in a peak of the channel increases the overall signal quality of the array.

As discussed in the previous chapter, improving the link budget of each of the MIMO
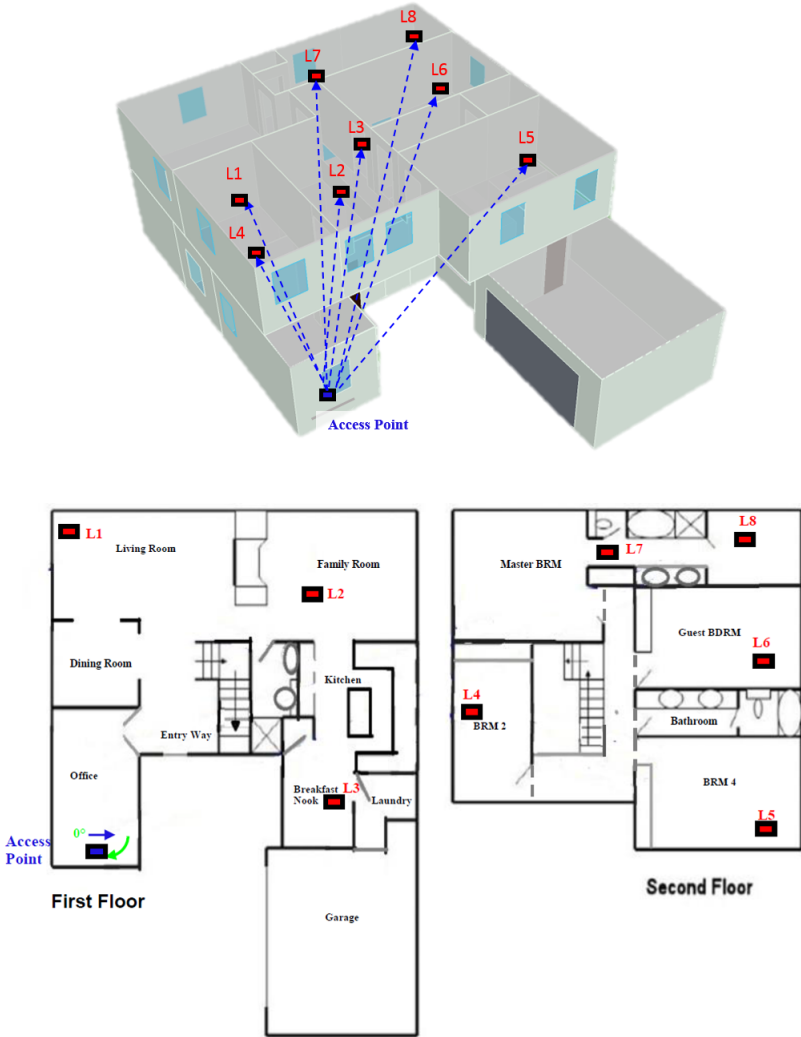
Figure 5.10: Eight locations of the 802.11ac client in the test house used for the study.

antennas also allows the baseband to use spatial multiplexing more often by better matching the MIMO channel eigenvalues. Each of the link-adaptive antennas is less likely to experience a deep fade, which may cause the baseband to revert back to diversity techniques for improved reliability.

We conduct a study comparing the access point with modal adaptive antennas and the baseline access point with printed dipole antennas. We place the access point on a stop-motion turntable and measure the uplink (from client to AP) and downlink (from AP to client) throughput at 30 degree intervals, and we record the average throughput at each of

8 client locations. We use the application iperf with a TCP window size of 1 MB and 4 simultaneous TCP/IP pairs to generate the data traffic for the measurements. We measure the active access point and passive access point one after another for each location so as to minimize the time between measurements. Figure 5.10 shows the client locations in the house. Figure 5.11 shows the access point and client positions. The client used for the study is an off the shelf 802.11ac handset with two 5 GHz WiFi antennas. The study was conducted on channel 36 (center frequency of 5180 MHz) with a bandwidth of 80 MHz.

WiFi access points and clients transmit and receive on the same frequency. Thus, we assume that the RSSI provides a reciprocal measure of the wireless channel, so that modes selected for receive are also selected for transmit. The channel reciprocity may not necessarily hold true as the components in the RF front end are different for the transmit and receive paths. However, because we only consider the relative difference between antenna states for the state prediction process, channel reciprocity is a fine assumption.

The throughput results for each of the eight locations are shown in Figure 5.12. Note that the uplink throughput is lower than the downlink throughput because the mobile client transmits at a lower power, due to the fact that handsets have more stringent SAR requirements and are equipped with PAs that transmit at lower output powers. For each of the locations, the active antenna system provides a higher uplink and downlink average throughput over the turntable angles. As expected, we see that lower throughputs have a larger percentage improvement. This is a result of the AMC and spectral efficiency mapping for 802.11ac (Figure 5.1). Furthermore, the results at each location depend on how the passive dipole antennas interact with the propagation waves in a cluttered indoor multipath environment. The active antenna system provides a downlink and uplink throughput percentage improvement of 23% and 35%, respectively, when compared against passive dipole antennas.

Similar to cellular fading scenarios, the improvement in link quality in indoor WLAN environments translates into an improved MCS, and hence an improved throughput and spectral efficiency for the modal antenna system compared to passive antennas. The largest capacity improvements occur at the edges of the home in regions of high multipath fading, especially on the second floor. These farthest clients consume the largest amount of the network time and bandwidth resources, and the ability to adapt the radiation state of the antenna to the multipath channel especially improves the spectral efficiency for these far clients.
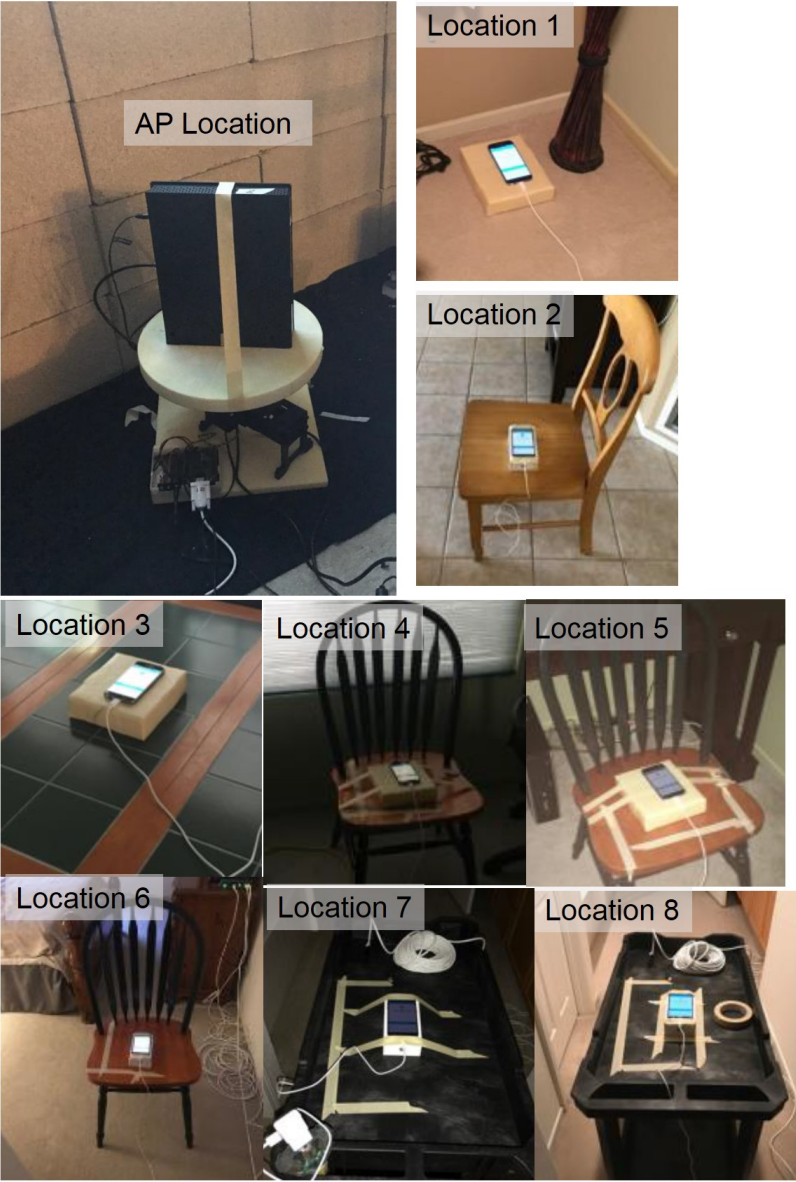
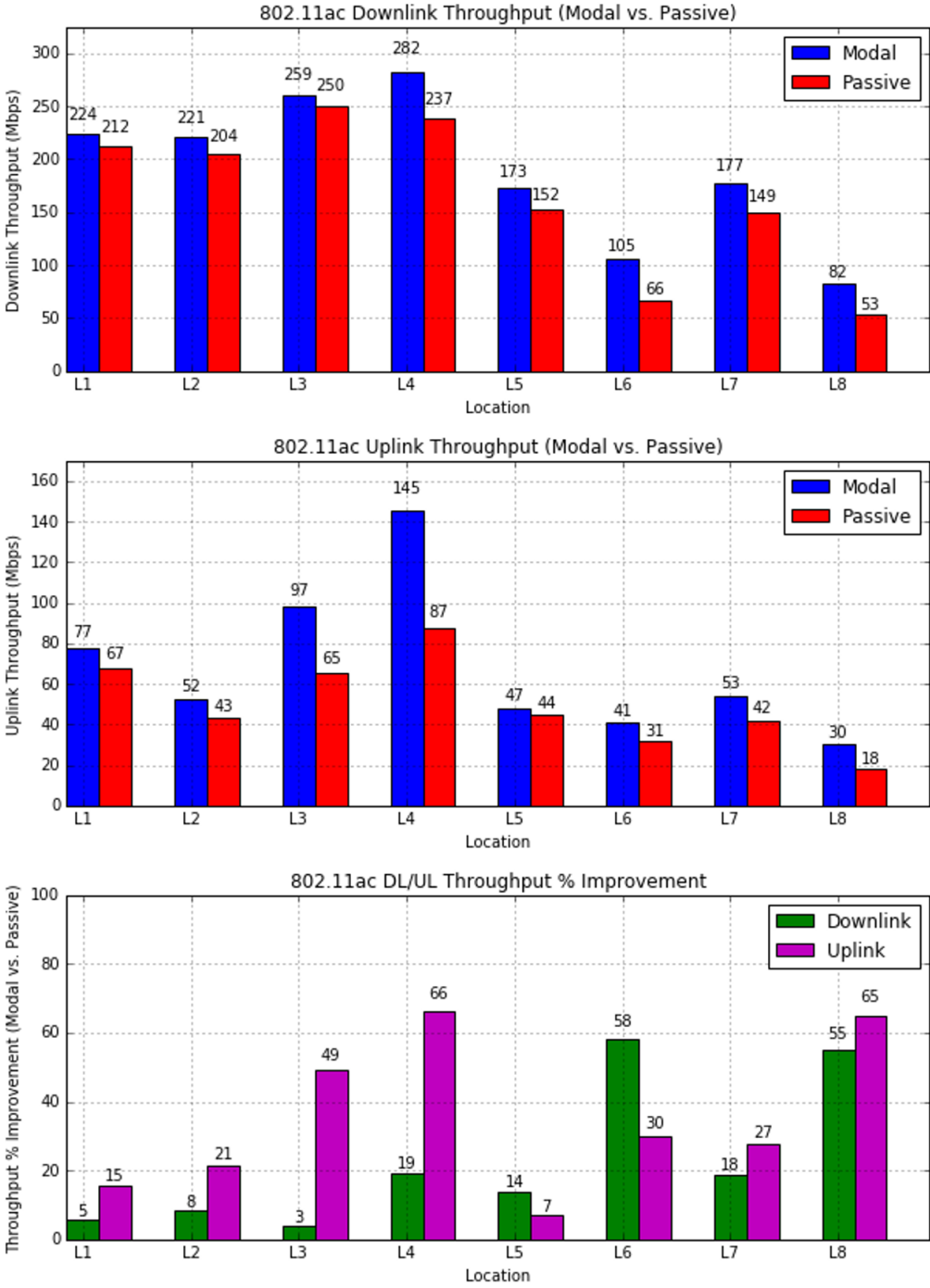Figure 5.11: Access point turntable setup and client test locations.

Figure 5.12: Measured uplink and downlink throughput results comparing the modal antenna system with passive printed dipole antennas.

Chapter 6

Conclusions

Mobile service providers have experienced explosive growth in the amount of data consumed on their networks. As handsets and other wireless devices are becoming equipped with more data-centric applications, operators are running out of spectrum to serve their users. We have presented link-adaptive antennas as a method to improve the capacity of these wireless networks. By dynamically switching radiating states from a single antenna feed, modal antennas are capable of adapting to reflections, scattering, and interference in multipath propagation environments. By improving the individual elements of multi-antenna systems, we have shown that modal antenna systems can enhance existing techniques, such as diversity and spatial multiplexing. We have evaluated link-adaptive antennas as practical systems, from the antenna architecture to the state prediction algorithms to actual field measurements. It has been shown that modal antenna systems can enhance the link margin of existing wireless systems by 2 to 3 dB on average, which translates into an average spectral efficiency enhancement of more than 30%, depending on the application.

Future work will explore synchronizing the antenna state prediction process with the spatial multiplexing and beamforming algorithms running on the baseband processor. Moreover, a physical layer implementation of the algorithm will allow for faster channel sample times and better performance in fast-fading scenarios. The field measurements and experimental correlation between single antenna diversity gain and measured SINR and capacity may also be used to further evaluate the performance of link-adaptive antennas from a communication and information theoretic perspective. Overall, the results presented in this work highlight the potential for implementing link-adaptive antenna systems in handsets and other mobile devices as a method to improve the capacity of existing and future wireless communication networks.

Bibliography

[1] Tyseer Aboulnasr and K Mayyas. "A robust variable step-size LMS-type algorithm: analysis and simulations". In: *IEEE Transactions on signal processing* 45.3 (1997), pp. 631–639.

[2] Siavash M Alamouti. "A simple transmit diversity technique for wireless communications". In: *IEEE Journal on selected areas in communications* 16.8 (1998), pp. 1451–1458.

[3] Mohd Tarmizi Ali et al. "A novel of reconfigurable planar antenna array (RPAA) with beam steering control". In: *Progress In Electromagnetics Research B* 20 (2010), pp. 125–146.

[4] IEEE Standard Association et al. *IEEE standard 802.11 ac-2013*. 2013.

[5] David Astély et al. "LTE: the evolution of mobile broadband". In: *IEEE Communications magazine* 47.4 (2009).

[6] Martin Badsberg, Jørgen Bach Andersen, and Preben Elgaard Mogensen. "Exploitation of the terrain profile in the Hata model". In: (1995).

[7] Constantine A. Balanis. *Antenna Theory: Analysis and Design*. Wiley-Interscience, 2005. ISBN: 0471714623.

[8] Daniel S Baum, Jan Hansen, and Jari Salo. "An interim channel model for beyond-3G systems: extending the 3GPP spatial channel model (SCM)". In: *Vehicular Technology Conference, 2005. VTC 2005-Spring. 2005 IEEE 61st*. Vol. 5. IEEE. 2005, pp. 3132–3136.

[9] Roberta Cardinali et al. "Comparison of clutter and multipath cancellation techniques for passive radar". In: *Radar Conference, 2007 IEEE*. IEEE. 2007, pp. 469–474.

[10] Yoann Corre and Yves Lostanlen. "Three-dimensional urban EM wave propagation model for radio network planning and optimization over large areas". In: *IEEE Transactions on Vehicular Technology* 58.7 (2009), pp. 3112–3123.

[11] Erik Dahlman, Stefan Parkvall, and Johan Skold. *4G: LTE/LTE-advanced for mobile broadband*. Academic press, 2013.

[12] Supratim Deb et al. "Algorithms for enhanced inter-cell interference coordination (eICIC) in LTE HetNets". In: *IEEE/ACM transactions on networking* 22.1 (2014), pp. 137–150.

[13] Gregory D Durgin, Theodore S Rappaport, and Hao Xu. "Partition-based path loss analysis for in-home and residential areas at 5.85 GHz". In: *Global Telecommunications Conference, 1998. GLOBECOM 1998. The Bridge to Global Integration. IEEE.* Vol. 2. IEEE. 1998, pp. 904–909.

[14] Vinko Erceg et al. "An empirically based path loss model for wireless channels in suburban environments". In: *IEEE Journal on selected areas in communications* 17.7 (1999), pp. 1205–1211.

[15] Richard B Ertel et al. "Overview of spatial channel models for antenna array communication systems". In: *IEEE personal communications* 5.1 (1998), pp. 10–22.

[16] TS ETSI. "136 214 v11. 1.0 (2012) LTE". In: *Evolved Universal Terrestrial Radio Access (E-UTRA); Physical layer; Measurements* ().

[17] ECFSTR EURO-COST231. "Urban Transmission Loss Models for Mobile Radio in the 900 and 1800 MHz Bands". In: *The Hague, Sep* (1991).

[18] Harald T Friis. "A note on a simple transmission formula". In: *Proceedings of the IRE* 34.5 (1946), pp. 254–256.

[19] Lloyd Griffiths and CW Jim. "An alternative approach to linearly constrained adaptive beamforming". In: *IEEE Transactions on antennas and propagation* 30.1 (1982), pp. 27–34.

[20] Masaharu Hata. "Empirical formula for propagation loss in land mobile radio services". In: *IEEE transactions on Vehicular Technology* 29.3 (1980), pp. 317–325.

[21] Md Rashidul Islam, Nowrin H Chamok, and Mohammod Ali. "Switched parasitic dipole antenna array for high-data-rate body-worn wireless applications". In: *IEEE Antennas and Wireless Propagation Letters* 11 (2012), pp. 693–696.

[22] Ramakrishna Janaswamy. "Spatial Diversity for Wireless Communications". In: *Handbook of Antennas in Wireless Communications.* CRC Press, 2001, pp. 601–624.

[23] Muhammad Ramlee Kamarudin et al. "Electronically switched beam disk-loaded monopole array antenna". In: *Progress In Electromagnetics Research* 101 (2010), pp. 339–347.

[24] Mohammad T Kawser et al. "Downlink SNR to CQI Mapping for Different MultipleAntenna Techniques in LTE". In: *International Journal of Information and Electronics Engineering* 2.5 (2012), p. 757.

[25] Joseph B Keller. "Geometrical theory of diffraction". In: *JOSA* 52.2 (1962), pp. 116–130.

[26] Ryuji Kohno et al. "Combinations of an adaptive array antenna and a canceller of interference for direct-sequence spread-spectrum multiple-access system". In: *IEEE journal on Selected Areas in Communications* 8.4 (1990), pp. 675–682.

[27] Robert G Kouyoumjian and Prabhakar H Pathak. "A uniform geometrical theory of diffraction for an edge in a perfectly conducting surface". In: *Proceedings of the IEEE* 62.11 (1974), pp. 1448–1461.

[28] Volodymyr Kuleshov and Doina Precup. "Algorithms for multi-armed bandit problems". In: *arXiv preprint arXiv:1402.6028* (2014).

[29] Anita G Longley and Patricia L Rice. *Prediction of tropospheric radio transmission loss over irregular terrain. A computer method-1968*. Tech. rep. DTIC Document, 1968.

[30] David Lopez-Perez et al. "Enhanced intercell interference coordination challenges in heterogeneous networks". In: *IEEE Wireless Communications* 18.3 (2011).

[31] Justin J Luther, Siamak Ebadi, and Xun Gong. "A microstrip patch electronically steerable parasitic array radiator (ESPAR) antenna with reactance-tuned coupling and maintained resonance". In: *IEEE Transactions on Antennas and Propagation* 60.4 (2012), pp. 1803–1813.

[32] Jonas Medbo, Mathias Riback, and J-E Berg. "Validation of 3GPP spatial channel model including WINNER wideband extension using measurements". In: *Vehicular Technology Conference, 2006. VTC-2006 Fall. 2006 IEEE 64th*. IEEE. 2006, pp. 1–5.

[33] Tariqul Islam Mohammad and Abidin Abdual Rashid Zainol. "MI-NLMS adaptive beamforming algorithm for smart antenna system applications". In: *Journal of Zhejiang University-SCIENCE A* 7.10 (2006), pp. 1709–1716.

[34] Andreas F Molisch. *Wireless communications*. Vol. 34. John Wiley & Sons, 2012.

[35] Jindřich Musil and Frantisek Zacek. "Microwave Measurements of Complex Permittivity by Free Space Methods and Their Applications.(Translation)". In: *Academia, 1986,* (1986), p. 275.

[36] Marc C Necker. "Scheduling constraints and interference graph properties for graph-based interference coordination in cellular OFDMA networks". In: *Mobile Networks and Applications* 14.4 (2009), pp. 539–550.

[37] Marija M Nikolic, Antonije R Djordjevic, and Arye Nehorai. "Microstrip antennas with suppressed radiation in horizontal directions and reduced coupling". In: *IEEE Transactions on Antennas and Propagation* 53.11 (2005), pp. 3469–3476.

[38] Yoshihisa Okumura et al. "Field strength and its variability in VHF and UHF land-mobile radio service". In: *Rev. Elec. Commun. Lab* 16.9 (1968), pp. 825–73.

[39] Prabhat Patel and Ajit Kumar Chaturvedi. "Impact of Noise Imbalance on the Performance of Predetection Dual-EGC Receivers over Rayleigh Fading Channels". In: *Global Telecommunications Conference, 2007. GLOBECOM'07. IEEE*. IEEE. 2007, pp. 3596–3600.

[40] Laurent Petit, Laurent Dussopt, and J-M Laheurte. "MEMS-switched parasitic-antenna array for radiation pattern diversity". In: *IEEE Transactions on Antennas and Propagation* 54.9 (2006), pp. 2624–2631.

[41] SL Preston et al. "Electronic beam steering using switched parasitic patch elements". In: *Electronics Letters* 33.1 (1997), pp. 7–8.

[42] John G Proakis. "Digital communications. 1995". In: *McGraw-Hill, New York* ().

[43] Theodore S Rappaport et al. *Wireless communications: principles and practice*. Vol. 2. Prentice Hall PTR New Jersey, 1996.

[44] Herbert Robbins. "Some aspects of the sequential design of experiments". In: *Herbert Robbins Selected Papers*. Springer, 1985, pp. 169–177.

[45] Sebastian Rowson, Gregory Poilasne, and Laurent Desclos. "Isolated magnetic dipole antenna: application to GPS". In: *Microwave and optical technology Letters* 41.6 (2004), pp. 449–451.

[46] Richard Roy and Thomas Kailath. "ESPRIT-estimation of signal parameters via rotational invariance techniques". In: *IEEE Transactions on acoustics, speech, and signal processing* 37.7 (1989), pp. 984–995.

[47] Artem Saakian. *Radio wave propagation fundamentals*. Artech House, 2011.

[48] Akbar M Sayeed. "Deconstructing multiantenna fading channels". In: *IEEE Transactions on Signal Processing* 50.10 (2002), pp. 2563–2579.

[49] Robert Schlub, Junwei Lu, and Takashi Ohira. "Seven-element ground skirt monopole ESPAR antenna design from a genetic algorithm and the finite element method". In: *IEEE Transactions on Antennas and Propagation* 51.11 (2003), pp. 3033–3039.

[50] I Schneider, F Lambrecht, and A Baier. "Enhancement of the Okumura-Hata propagation model using detailed morphological and building data". In: *Personal, Indoor and Mobile Radio Communications, 1996. PIMRC'96., Seventh IEEE International Symposium on*. Vol. 1. IEEE. 1996, pp. 34–38.

[51] Scott Y Seidel and Theodore S Rappaport. "914 MHz path loss prediction models for indoor wireless communications in multifloored buildings". In: *IEEE transactions on Antennas and Propagation* 40.2 (1992), pp. 207–217.

[52] Scott Y Seidel et al. "Path loss, scattering and multipath delay statistics in four European cities for digital cellular and microcellular radiotelephone". In: *IEEE Transactions on Vehicular Technology* 40.4 (1991), pp. 721–730.

[53] Stefania Sesia, Matthew Baker, and Issam Toufik. *LTE-the UMTS long term evolution: from theory to practice*. John Wiley & Sons, 2011.

[54] NH Shahadan et al. "Switched parasitic dielectric resonator antenna array using capacitor loading for 5G Applications". In: *Antennas and Propagation (EuCAP), 2016 10th European Conference on*. IEEE. 2016, pp. 1–5.

[55] Hyun-Chool Shin, Ali H Sayed, and Woo-Jin Song. "Variable step-size NLMS and affine projection algorithms". In: *IEEE signal processing letters* 11.2 (2004), pp. 132–135.

[56] Quentin H Spencer et al. "Modeling the statistical time and angle of arrival characteristics of an indoor multipath channel". In: *IEEE Journal on Selected areas in communications* 18.3 (2000), pp. 347–360.

[57] David H Staelin, Ann W Morgenthaler, and Jin Au Kong. *Electromagnetic waves.* Pearson Education India, 1994.

[58] Stergios Stergiopoulos. "Advanced beamformers". In: *Advanced Signal Processing Handbook: Theory and Implementation for Radar, Sonar, and Medical Imaging Real Time Systems.* CRC press, 2000.

[59] Warren L Stutzman and Gary A Thiele. *Antenna theory and design.* John Wiley & Sons, 2012.

[60] Vahid Tarokh, Hamid Jafarkhani, and A Robert Calderbank. "Space-time block codes from orthogonal designs". In: *IEEE Transactions on information theory* 45.5 (1999), pp. 1456–1467.

[61] Grigoriy I Torgovnikov. "Dielectric Properties of Wood-Based Materials". In: *Dielectric Properties of Wood and Wood-Based Materials.* Springer, 1993, pp. 135–159.

[62] David Tse and Pramod Viswanath. *Fundamentals of wireless communication.* Cambridge university press, 2005.

[63] Joannes Vermorel and Mehryar Mohri. "Multi-armed bandit algorithms and empirical evaluation". In: *European conference on machine learning.* Springer. 2005, pp. 437–448.

[64] Arthur Robert Von Hippel. *Dielectric materials and applications.* Vol. 2. Artech House on Demand, 1954.

[65] Joram Walfisch and Henry L Bertoni. "A theoretical model of UHF propagation in urban environments". In: *IEEE Transactions on antennas and propagation* 36.12 (1988), pp. 1788–1796.

[66] Christopher John Cornish Hellaby Watkins. "Learning from delayed rewards". PhD thesis. University of Cambridge England, 1989.

[67] Harold A Wheeler. "Fundamental limitations of small antennas". In: *Proceedings of the IRE* 35.12 (1947), pp. 1479–1484.

[68] Bernard Widrow and Samuel D Stearns. "Adaptive signal processing". In: (1985).

[69] Bernard Widrow et al. "Adaptive antenna systems". In: *Proceedings of the IEEE* 55.12 (1967), pp. 2143–2159.

[70] Bernard Widrow et al. "Adaptive noise cancelling: Principles and applications". In: *Proceedings of the IEEE* 63.12 (1975), pp. 1692–1716.

[71] Guanghan Xu and Thomas Kailath. "Fast subspace decomposition". In: *IEEE Transactions on Signal Processing* 42.3 (1994), pp. 539–551.

[72] Dimitra Zarbouti et al. "The effective radiation pattern concept for realistic performance estimation of LTE wireless systems". In: *International Journal of Antennas and Propagation* 2013 (2013).